Mineralium Deposita (2023) 58:161–196
https://doi.org/10.1007/s00126-022-01143-x

ARTICLE

Genesis of hydrous-oxidized parental magmas for porphyry Cu (Mo, Au) deposits in a postcollisional setting: examples from the Sanjiang region, SW China

Lei-Luo Xu[1] · Jing-Jing Zhu[1] · Ming-Liang Huang[1] · Li-Chuan Pan[1] · Ruizhong Hu[1,2] · Xian-Wu Bi[1,2]

Received: 18 November 2021 / Accepted: 30 September 2022 / Published online: 19 October 2022

Abstract
Magmatic sources of porphyry deposits in postcollisional settings remain controversial. We have used new and published petrological and geochemical data for the Eocene–Oligocene porphyry Cu ± Mo ± Au deposits in the Sanjiang region, SW China, to address this outstanding issue. New data for three deposits (Machangqing, Tongchang, and Beiya) in the Ailaoshan–Red River porphyry Au-Cu-Mo belt (southern part of the Sanjiang region) suggest that ore-forming porphyries were emplaced at ~ 35 Ma, have high $(^{87}Sr/^{86}Sr)_i$ (0.7068–0.7071) and negative $\varepsilon_{Nd}(t)$ (−6.9 to −5.0), low zircon $\varepsilon_{Hf}(t)$ (−5.3 to 4.5), and relatively high $\delta^{18}O$ (5.9–9.0‰). Magmatic amphibole phenocryst compositions indicate that the parental magmas are all relatively oxidized (ΔFMQ = 1.7 ± 0.6), and H_2O-rich (3.8 ± 0.3 wt% H_2O). These results are consistent with those estimated from zircon compositions (ΔFMQ = 1.8 ± 0.8) and high whole-rock Sr/Y ratios (75 ± 31), respectively. Based on the new and published data, we suggest that the parental magmas for the Ailaoshan–Red River porphyry Au-Cu-Mo belt were derived from a preserved juvenile arc lower-crust and the underlying metasomatized subcontinental lithospheric mantle (SCLM) attributed to a Neoproterozoic subduction event, whereas the parental magmas for the Yulong porphyry Cu-Mo belt (northern part of the Sanjiang region) originated from the Permian–Triassic juvenile arc lower-crust and metasomatized SCLM. Additionally, parental magmas for these porphyry deposits are all oxidized and H_2O-rich, and we attribute such characteristics to inheritance from mixed mantle-crust sources that were modified by previous oceanic slab subduction.

Keywords Porphyry Cu-Mo-Au deposits · Postcollisional setting · Hydrous-oxidized magma · Petrogenesis · Sanjiang region

Introduction

Porphyry deposits are significant global repositories of copper, gold, and molybdenum. The majority of such deposits occur in oceanic or continental arcs above subduction zones, such as those distributed around the Pacific Rim (e.g., El Teniente, Chuquicamata, and El Salvador; Richards 2003, 2009; Cooke et al. 2005; Sillitoe 2010). Many studies have shown that most arc porphyry Cu ± Mo ± Au deposits are associated with moderately oxidized (ΔFMQ = 1 to 2) and H_2O-rich (> 4 wt%) intermediate–felsic magmas (Mungall 2002; Sillitoe 2010; Richards 2015a; Richards and Şengör 2017; Chiaradia 2021). The relatively high oxidation state likely suppresses the formation of magmatic sulfide phases which would strip the magmas of the Cu, Mo, and Au ore metals at early stages of magma evolution, and which facilitates transportation of economic metals (e.g., Cu and Au) into upper crustal levels in the fractionating magmas (Ballard et al. 2002; Richards 2009, 2015a; Richards and Şengör 2017). Additionally, H_2O-rich magma would provide enough exsolving water for the formation of porphyry deposits (Richards and Kerrich 2007; Richards 2011a). It has been widely accepted that basaltic melts generated by partial melting of the metasomatized asthenospheric mantle wedge

Editorial handling: C. Mercer

✉ Jing-Jing Zhu
zhujingjing@vip.gyig.ac.cn

✉ Xian-Wu Bi
bixianwu@vip.gyig.ac.cn

1 State Key Laboratory of Ore Deposit Geochemistry, Institute of Geochemistry, Chinese Academy of Sciences, Guiyang 550081, China

2 College of Earth and Planetary Sciences, University of Chinese Academy of Sciences, Beijing 100049, China

underwent MASH processes (melting, assimilation, storage, and homogenization; Hildreth and Moorbath 1988; Richards et al. 2003) at the base of the lower crust, eventually forming intermediate–felsic arc magmas (Ringwood 1977; Richards 2003, 2011b). Interaction between asthenospheric mantle and oxidized hydrothermal fluids and/or silicate melts released from a subducted oceanic slab, resulted in the elevated fO_2 and H_2O of the mantle wedge and sequently in arc magmas that form porphyry Cu ± Mo ± Au deposits (Richards 2003, 2015a; Richards and Şengör 2017; Park et al. 2021).

In the last three decades, many porphyry Cu ± Mo ± Au deposits in postcollisional settings have been discovered, including those in the Eocene–Oligocene Jinshajiang–Ailaoshan porphyry Cu-Mo-Au belt in the Sanjiang (Three Rivers) region, SW China (Table 1) (Hu et al. 2004), the Miocene Gangdese porphyry Cu belt in south Tibet, China (Hou et al. 2015a), the Kerman porphyry Cu belt in south Iran (Shafiei et al. 2009), the Western Tethys (SE Europe and Anatolia) (Richards 2015b), and the North American Cordillera (Logan and Mihalynuk 2014). It has been suggested that these postcollisional ore-forming porphyry magmas were generated by remelting of (1) metasomatized subcontinental lithospheric mantle (SCLM) enriched by previous oceanic subduction (Lu et al. 2015a; Holwell et al. 2019), (2) thickened old lower-crust (Chung et al. 2003), (3) juvenile mafic arc lower-crust formed by previous oceanic subduction (Hou et al. 2004, 2015a), or (4) both metasomatized SCLM and juvenile mafic arc lower-crust (Richards 2009). Post-subduction lithospheric thickening, lithospheric extension, or mantle lithosphere delamination have been proposed as mechanisms for the formation of postcollisional ore-forming porphyry magmas (Hou et al. 2003, 2015b; Richards 2009, 2015b; Xu et al. 2016a; Wang et al. 2018a; Yang and Cooke 2019).

Like ore-forming magmas in active arcs, the parental magmas for the postcollisional porphyry deposits are also characterized by elevated fO_2 and H_2O ($\Delta FMQ = 1$ to 2, $H_2O > 4$ wt%; Liang et al. 2006, 2009; Bi et al. 2009; Richards 2009; Shafiei et al. 2009; Hou et al. 2011, 2015a, 2015b; Wang et al. 2014a, 2014b, 2018a; Lu et al. 2015a, 2016; Xu et al. 2016a, 2019; Yang et al. 2014a, 2016). However, due to the absence of active oceanic slab subduction, the fundamental controls on the elevated fO_2 and H_2O in the parental magmas for the postcollisional Cu ± Mo ± Au porphyry deposits remain controversial. For example, in the Gangdese porphyry Cu belt, the oxidized and hydrous ore-forming magmas are thought to be derived from either the juvenile lower-crust (Hou et al. 2011, 2013, 2015a, 2015b; Wang et al. 2014a, 2014b; Yang et al. 2015; Hou and Wang 2019; Yang and Cooke 2019) or Tibetan mantle (Lu et al. 2015a; Xu et al. 2021). Specifically, dehydration melting of amphibole-bearing juvenile lower-crust could release H_2O into ore-forming magmas, which might also lead to elevated magmatic oxidation state given that fO_2 correlates positively with water contents in the deep crust (Hou et al. 2011, 2015a). However, it has been suggested that the breakdown of amphibole during melting may not provide sufficient water for porphyry Cu formation, and thus additional water may be necessary (Hronsky et al. 2012; Lu et al. 2015a; Yang et al. 2015). Such exogenous water could be released from the Tibetan mantle-derived ultrapotassic magma, probably originally from the subducted Indian continental plate (Yang et al. 2016; Wang et al. 2018a; Yang and Cooke 2019).

In general, it is debated whether and how mantle-derived melts have been involved in the generation of fertile porphyry magmas. In this contribution, we have addressed this issue by investigating critical petrological and geochemical data from this study and the literature for the Eocene–Oligocene Jinshajiang–Ailaoshan porphyry Cu-Au-Mo belt in the Sanjiang region, SW China, where numerous postcollisional porphyry Cu-Mo-Au deposits are present (Fig. 1; e.g., Narigongma, Yulong, Beiya, Machangqing, Tongchang and Yao'an; Hou et al. 2003, 2017; Xu et al. 2012; Yang et al. 2014a; He et al. 2016). The data used in this study include zircon U−Pb ages, Hf−O isotopes, zircon and amphibole chemical compositions, and whole-rock chemical and Sr−Nd isotope compositions. We demonstrate that the parental magmas for the porphyry deposits in the Jinshajiang–Ailaoshan belt were derived from the juvenile lower-crust, which mixed with partial melts derived from the underlying metasomatized SCLM formed during earlier subduction, both of which are hydrous and oxidized.

Geological background

Tectonic evolution in the Sanjiang region

The Sanjiang region constitutes the southeastern part of the Tibetan Plateau and western Yunnan Province (Deng et al. 2014a, 2014b), with a collage of Paleozoic arc terranes and Gondwana-derived microcontinental blocks (Fig. 1; Mo et al. 1994; Metcalfe 2002, 2013; Deng et al. 2014a; Wang et al. 2018b; Zhao et al. 2018a). These blocks were amalgamated to form part of the Eurasian continent during multiple Tethyan suture events (i.e., Paleo-, Meso-, and Neo-Tethys; Fig. 1A) prior to the Early Cenozoic (Hu et al. 2004; Deng et al. 2014a). The major continental blocks in the southern part of this region are the South China Block in the east, the Indochina Block in the middle, and the Sibumasu Block in the west, separated by the Jinshajiang–Ailaoshan and Changning–Menglian Paleo-Tethys sutures (sutures II–III and IV_2 on Fig. 1; Deng et al. 2014a; Wang et al. 2018b). The northwestern part of this region consists of the Songpan–Garzê and three Gondwana-derived micro-continental blocks, namely the East Qiangtang, West Qiangtang, and Lhasa blocks that are separated from north to south by the Jinshajiang and

Table 1 Geological and mineralization features of the Eocene–Oligocene fertile porphyries and associated Cu-Mo-Au deposits in the Sanjiang region, SW China

Pluton/Deposit	Longtitude, latitude	Wall rock	Lithology and mineralogy	Porphyry occurrence	Outcrop area	Alteration	Mineralization	Reserves (contained metals)	Ore grade	Ore structure	Shape of orebody	Reference
Fertile porphyry plutons and associated deposits in the Yulong porphyry Cu–Mo belt												
Narigongma	31°31′N, 94°46′E	$P_{2–3}$: basalt, andesitic basalt, and minor andesite	Biotite granite porphyry (phenocrysts 25–30 vol.%: Pl + Kfs + Qtz + Bt + Amp), granite porphyry (phenocryst: Kfs + Bt + Qtz + Pl), and quartz diorite porphy (phenocrysts 25–30 vol.%: Pl + Qtz + Kfs)	Stocks	1.2 km^2	Potassic, phyllic, propylitic, argillic	Cu-Mo (Au)	0.46 Mt Cu, 0.25 Mt Mo	Cu: 0.32%, Mo: 0.06%	Veinlet	Stratiform and lenticular orebodies in the stock and contact	Yang et al. 2014a
Baomai	31°45′N, 97°25′E	T_{2-3}: limestone, siltstone, sandstone, mudstone and conglomerate Pt_1: biotite monzonitic gneiss, and plagioclase gneiss	Biotite granite porphyry (phenocrysts 25–40 vol.%: Kfs + Pl + Qtz + Bt) and biotite monzogranite porphyry (phenocrysts 25–40 vol.%: Kfs + Pl + Bt + Qtz)	Stocks	1.2 km^2	Potassic, phyllic, propylitic, argillic, hornfel	Cu-Mo	0.21 Mt Cu, 0.06 Mt Mo	Cu: 0.22%, Mo: 0.06%	veinlet, disseminated	Pipe-like, tubular, lenticular, vein-like orbodies in the sock and wall rocks	Lin et al. 2017, 2018
Yulong	31°24′N, 97°44′E	T_3: crystalline limestone	Monzogranite porphyry (phenocrysts 40–60 vol.%: Pl + Kfs + Qtz + Bt + Amp), quartz monzonite porphyry, and syenogranite porphyry	Stocks	0.64 km^2	Potassic, phyllic, propylitic, argillic, skarnization, hornfel	Cu-Mo (Au)	6.5 Mt Cu, 0.41 Mt Mo	Cu: 0.62%, Mo: 0.04%	Veinlet, disseminated, brecciated	Stratiform, lenticular and pipe-like orebodies in the stock and contact	Yulong Copper 2009
Zhanaga	31°15′N, 97°44′E	T_3: sandy mudstone	Monzogranite porphyry (phenocrysts: Pl + Qtz + Kfs + Bt + Amp) and syenogranite porphyry	Stocks	0.60 km^2	Potassic, phyllic, propylitic, argillic, skarnization	Cu (Mo)	0.30 Mt Cu, Mo?	Cu: 0.36%, Mo: 0.03%, Au: 0.03 ppm	Veinlet, disseminated	Pipe-like orebodies in the stock	Hou et al. 2003, 2006; Liang et al. 2006

Table 1 (continued)

Pluton/ Deposit	Longtitude, latitude	Wall rock	Lithology and mineralogy	Porphyry occurrence	Outcrop area	Alteration	Minerali-zation	Reserves (contained metals)	Ore grade	Ore struc-ture	Shape of orebody	Reference
Mangzong	31°12′N, 97°48′E	T_3: sandy mudstone	Monzogranite porphyry (phenocrysts: Pl + Kfs + Amp + Bt + Qtz), alkali-feldspar granite porphyry, and K-feldspar granite porphyry	Stocks	0.28 km^2	Potassic, phyllic, propylitic, argillic, skarnization	Cu (Mo)	0.25 Mt Cu, Mo?	Cu: 0.34%, Mo: 0.03%, Au: 0.02 g/t	Veinlet, disseminated	Regular pipe-like orebodies in stock	Hou et al. 2003, 2006; Liang et al. 2006
Duoxia-songduo	31°5′N, 97°52′E	T_3: sandy mudstone	Monzogranite porphyry (phenocrysts: Kfs + Pl + Qtz + Bt), alkali-feldspar granite porphyry, and granodiorite porphyry	Stocks	0.30 km^2	Potassic, phyllic, propylitic, skarn	Cu (Mo)	0.50 Mt Cu, Mo?	Cu: 0.38%, Mo: 0.04%, Au: 0.05 g/t	Veinlet, disseminated, stockwork	Regular lenticular orebodies in the stock	Hou et al. 2003, 2006; Liang et al. 2006
Malasong-duo	31°N, 97°57′E	T_1: rhyolite	Monzogranite porphyry (phenocrysts: Kfs + Pl + Qtz + Bt) and syenogranite porphyry	Stocks	0.13 km^2	Potassic, phyllic, propylitic, skarnization	Cu (Mo)	1.0 Mt Cu, Mo?	Cu: 0.44%, Mo: 0.14%, Au: 0.06 g/t	Veinlet, disseminated	Regular lenticular orebodis in the stock	Hou et al. 2003, 2006; Liang et al. 2006
Fertile porphyry plutons and associated deposits in the Ailaoshan−Red River porphyry Au−Cu−Mo belt												
Machang-qing	25°31′N, 100°26′E	O_1–D_1: limestone and sandstone	Granite porphyry (phenocrysts 35–40 vol.%: Kfs + Pl + Qtz + Amp + Bt), monzogranite porphyry (phenocrysts: Kfs + Pl + Qtz + Amp + Bt) monzonite porphyry (phenocrysts 30–40 vol.%: Kfs + Pl + Qtz + Bt), and equigranular granite (Kfs + Pl + Qtz + Amp + Bt)	Stocks	1.3 km^2	Potassic, phyllic, advanced argillic, skarnization	Cu-Mo (Au)	0.25 Mt Cu, Mo?	Cu: 0.44%, Mo: 0.14%, Au: 0.06 g/t	Veinlet, disseminated, massive	Lenticular, pocket, and irregular orebodies in the stock	Hou et al. 2003, 2006; Lu et al. 2013a
Habo	22°53′N, 102°35′E	Hymalayan granite	Quartz monzonite porphyry (phenocrysts 20–50 vol.%: Kfs + Pl + Qtz + Bt + Amp), granite porphyry (Pl + Qtz + Bt), syenite porphyry (Kfs + Pl + Amp + Px + Bt), monzonite porphyry (phenocryst 20–25 vol.%: Kfs + Pl; matrix 75–80 vol.%: Bt + Pl + Amp + Qtz)	Stocks and dykes	> 1.0 km^2	Potassic, phyllic, propylitic	Cu-Mo (Au)	0.53 Mt Cu, 37,718 t Mo	Cu: 0.42–1.0%, Mo: 0.01–0.1%, Au: 1–33 g/t	Veinlet, disseminated	Stratiform and lenticular orebody in the stock and contact	Zhu et al. 2013b; Xia et al. 2018; Yang et al. 2017

Table 1 (continued)

Pluton/ Deposit	Longtitude, latitude	Wall rock	Lithology and mineralogy	Porphyry occurrence	Outcrop area	Alteration	Mineralization	Reserves (contained metals)	Ore grade	Ore structure	Shape of orebody	Reference
Tongchang	22°47′N, 103°3′E	S_2: dolomitic limestone and sandstone	Quartz syenite porphyry (phenocrysts 35–50 vol.%: Kfs + Pl + Qtz + Amp + Bt)	Stocks and dykes	> 0.38 km^2	Potassic, phyllic, skarnization	Cu-Mo (Au)	37,958 t Cu, 30,370 t Mo	Cu: 1.24–1.48%, Mo: 0.13–0.218%, Au: 0.13–0.25 g/t	Veinlet, disseminated, massive	Stratiform and lenticular orebodies in the stock and skarn	Xu et al. 2012, 2014, 2019
Beiya	26°9′N, 100°12′E	T_2: limestone, T_1: sandstone, P: basalt	Granite porphyry (phenocrysts 35–50 vol.%: Kfs + Pl + Qtz + Amp), monzogranite porphyry (phenocrysts 35–50 vol.%: Kfs + Pl + Qtz + Amp), quartz monzonite porphyry (phenocrysts 35–50 vol.%: Kfs + Pl + Qtz + Amp), alkali-feldspar granite porphyry (phenocrysts: Kfs + Qtz), and mozonite porphyry	Stocks	concealed	Potassic, silicification, phyllic, skarnization, carbonation	Au (Cu-Fe-Ag-Pb–Zn)	323 t Au, 0.65 Mt Cu, 56.68 Mt Fe, 7745 t Ag, 0.15 Mt Pb, 0.05 Mt Zn	Au: 2.47 g/t, Cu: 0.52%, Fe: 33.34%, Ag: 44.82 g/t, Pb: 2.01%, Zn: 1.38%	Veinlet, disseminated, massive	Vein-like, pipe-like, stratiform and lenticular orebodies in the skarn zone, stock and wall rock	Zhou et al. 2017a
Yao'an	25°22′N, 101°16′E	J_2: mudstones and marls	Syenite porphyry (phenocrysts 35–50 vol.%: Kfs + Pl + Cpx + Amp + Bt), monzonite porphyry (phenocrysts: Kfs + Pl + Cpx + Bt + Amp), quartz syenite porphyry, and quartz monzonite porphyry (phenocrysts: Kfs + Pl + Cpx + Amp + Bt + Qtz)	Stocks	< 1.0 km^2	Potassic, phyllic, propylitic	Au	10 t Au	4–5 g/t Au	Massive, brecciated and banded	Vein-like and lenticular orebodies in the endo- and exo-contacts of the stock	Bi et al. 2005, 2009; Lu et al. 2013a

Amp: amphibole, *Bt:* biotite, *Cpx:* clinopyroxene, *Kfs:* *K*-feldsapr, *Pl:* plagioclase, *Px:* pyroxene, *Qtz:* quartz

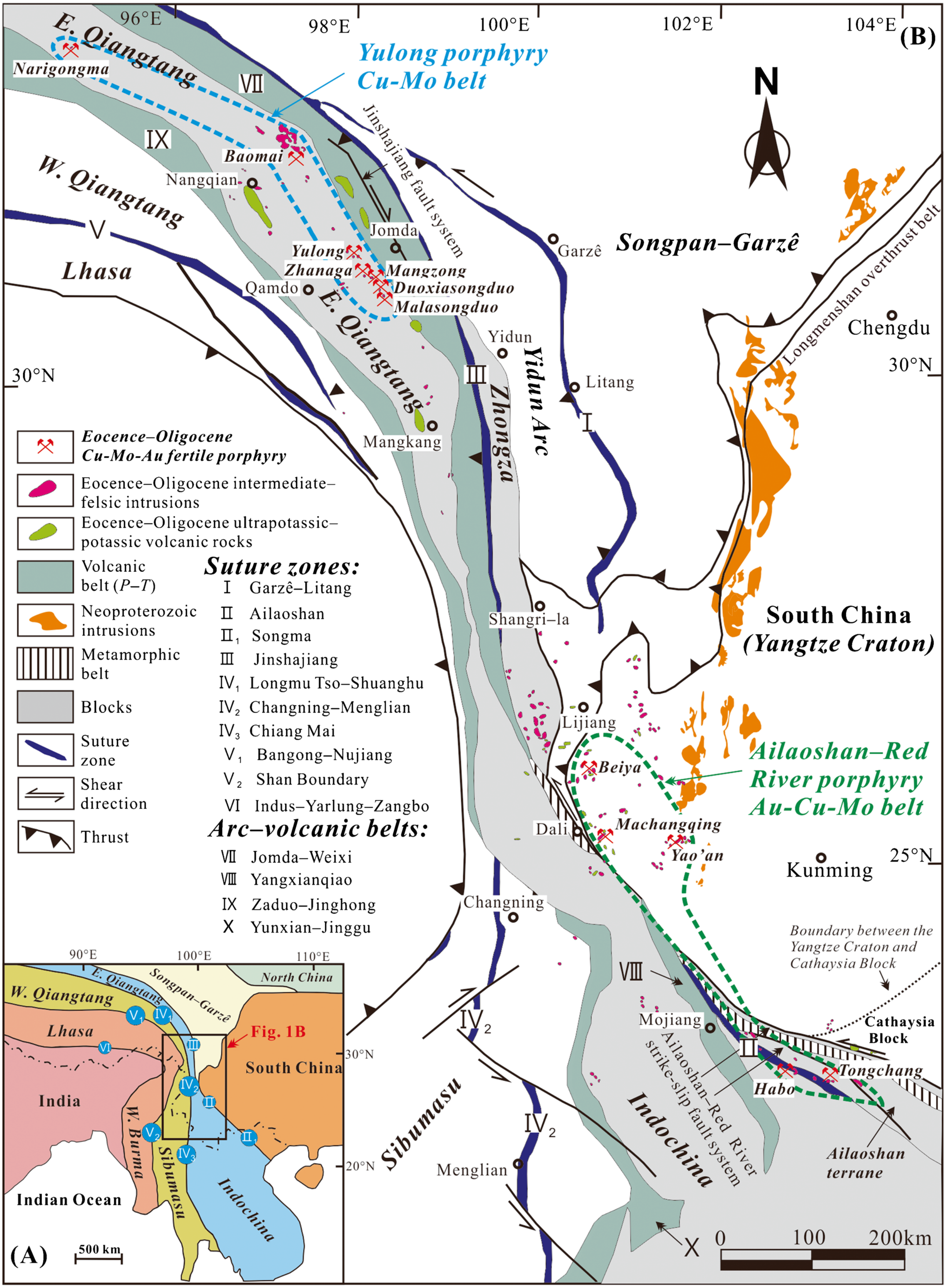
(B)
96°E
98°E
100°E
102°E
104°E
30°N
25°N
N
Yulong porphyry
Cu-Mo belt
E. Qiangtang
W. Qiangtang
Lhasa
Narigongma
Baomai
Nangqian
Jomda
Yulong
Zhanaga
Mangzong
Duoxiasongduo
Malasongduo
Qamdo
Mangkang
Yidun
Garzê
Litang
Songpan–Garzê
Chengdu
Longmenshan overthrust belt
Jinshajiang fault system
Yidun Arc
Zhongza
Shangri–la
Lijiang
Beiya
Dali
Machangqing
Yao'an
Kunming
South China
(Yangtze Craton)
Ailaoshan–Red
River porphyry
Au-Cu-Mo belt
Changning
Mojiang
Menglian
Sibumasu
Indochina
Ailaoshan–Red River
strike-slip fault system
Boundary between the
Yangtze Craton and
Cathaysia Block
Cathaysia
Block
Tongchang
Habo
Ailaoshan
terrane
0 100 200km
Eocence–Oligocene
Cu-Mo-Au fertile porphyry
Eocence–Oligocene intermediate–
felsic intrusions
Eocence–Oligocene ultrapotassic–
potassic volcanic rocks
Volcanic
belt (P–T)
Neoproterozoic
intrusions
Metamorphic
belt
Blocks
Suture
zone
Shear
direction
Thrust
Suture zones:
I Garzê–Litang
II Ailaoshan
II1 Songma
III Jinshajiang
IV1 Longmu Tso–Shuanghu
IV2 Changning–Menglian
IV3 Chiang Mai
V1 Bangong–Nujiang
V2 Shan Boundary
VI Indus–Yarlung–Zangbo
Arc–volcanic belts:
VII Jomda–Weixi
VIII Yangxianqiao
IX Zaduo–Jinghong
X Yunxian–Jinggu
(A)
90°E
100°E
110°E
30°N
20°N
North China
Songpan–Garzê
E. Qiangtang
W. Qiangtang
Lhasa
Fig. 1B
South China
India
W. Burma
Sibumasu
Indochina
Indian Ocean
500 km

◂**Fig. 1** **A** Distribution of principal continental Blocks and sutures of southeast Asia (modified from Deng et al. 2014a); **B** tectonic framework of the Sanjiang region showing the major terranes, suture zones, arc volcanic belts, and the Eocene–Oligocene fertile porphyry Cu-Mo-Au deposits (modified from Hou et al. 2003; Deng et al. 2014a and Zhu et al. 2015b). The distributions of the Neoproterozoic intrusions are from Zhao et al. (2018b), and the ultrapotassic–potassic volcanic rocks are from Lu et al. (2015b) and Xu et al. (2016b). Note the boundary between the Yangtze Craton and Cathaysia Block are from Zhao and Cawood (2012). E. Qiangtang = East Qiangtang; W. Qiangtang = West Qiangtang

Longmu Tso–Shuanghu Paleo-Tethys, and Bangong–Nujiang Meso-Tethys sutures (sutures III, IV_1, and V on Fig. 1; Deng et al. 2014a; Wang et al. 2016; Zhu et al. 2017).

The Sanjiang region has a complex evolutionary history from the Neoproterozoic to Cenozoic, due to the accretion of Gondwana-derived microcontinental blocks and arc terranes to Eurasia during multiple stages of opening and closure of the Tethys oceans, the intracontinental orogeny, as well as the Cenozoic tectonic deformation (Deng et al., 2014a, 2014b). Below is a brief summary of the tectonic evolution of the southern and northern parts of the Sanjiang region from the Neoproterozoic to Cenozoic, with schematic evolution models shown in ESM Fig. A1.

During the Early Neoproterozoic (ESM Figs. A1A-B), the western and southeastern margins of the Yangtze Craton underwent subduction of the Mozambique and Huanan oceans, respectively, as indicated by abundant ~ 850–740 Ma arc igneous suites (Panxi–Hannan–Ailaoshan arc) with compositions varying from mafic–ultramafic to intermediate and felsic rocks in the western margin of the Yangtze Craton, and abundant ~ 850–830 Ma arc igneous rocks in the southeastern margin of the Yangtze Craton, respectively (Zhou et al. 2002; Zhao and Zhou 2013; Zhao and Asimow 2014; Zhao et al. 2018b; Cawood et al. 2018; Yao et al. 2018). The subduction of the Huanan Ocean resulted in the amalgamation of the Yangtze Craton and Cathaysian Block at ~ 830 Ma, forming the South China Block (Zhao et al. 2018b). Later, the breakup of the Rodinia Supercontinent resulted in separation of the South China Block (Yangtze Craton and Cathaysian Block) from the Supercontinent. From the Late Neoproterozoic to Late Triassic (~ 700–230 Ma), the western margin of the South China Block was a passive continental margin, as indicated by the lack of granitoids and calc-alkaline volcanic rocks formed during this period (Li 1998; Metcalfe 2006; Pullen et al. 2008). In the Late Permian (~ 260 Ma), this region was affected by mantle plume activity, as indicated by voluminous continental flood basalts and associated mafic–ultramafic intrusions (Xu et al. 2008; Zhong et al. 2011).

From the Early Cambriam to Early–Middle Devonian, the Sanjiang region underwent opening and closure of the Proto-Tethys oceans (Deng et al. 2014a). The closure of the Proto-Tethys Ocean was coupled with the opening of the Paleo-Tethys Ocean during the Middle–Late Devonian (ESM Fig. A1C). The main units of the Paleo-Tethys Ocean in the Sanjiang region include the Longmu Tso–Shuanghu–Changning–Menglian main ocean, and the Jinshajiang, Ailaoshan, and Garzê–Litang branch oceans (ESM Fig. A1C). It is widely accepted that the northwest trending Longmu Tso–Shuanghu–Changniang–Menglian suture represents the remnant of the main Paleo-Tethys Ocean, whereas the Jinshajiang–Ailaoshan and Garzê–Litang sutures represent the remnant of a branch or the back-arc basin of that ocean (e.g., Wang et al. 2000, 2018b; Metcalfe 2013; Deng et al. 2014a; Zhao et al. 2018a; Fig. 1). Permian–Trassic arc igneous suites along the eastern margin of the Zhongza Block, eastern and western margins of the East Qiangtang–Indochina Block (e.g., Yidun, Jomda–Weixi, Yangxianqiao, Zaduo–Jinghong, and Yunxian–Jinggu volcanic arcs) have been used as evidence for subduction of Paleo-Tethys oceanic plates (Fig. 1B and ESM Figs. A1E-F; Mo et al. 1994; Wang et al. 2000; Jian et al. 2009; Yang et al. 2011, 2014b; Zi et al. 2012; Wu et al. 2013; Deng et al. 2014a; Xin et al. 2018). The closure of the Paleo-Tethys Ocean, which resulted in final amalgamation between the South China, Zhongza, East Qiangtang, Indochina, and West Qiangtang blocks, is thought to be prior to the Late Triassic (~ 230 Ma; see reviews by Deng et al. 2014a, Wang et al. 2018b and Zhao et al. 2018a; ESM Fig. A1F).

The Bangong–Nujiang suture extends for over 2000 km within central Tibet and was formed by the closure of the Bangong–Nujiang Meso-Tethys Ocean (e.g., Yin and Harrison 2000; Guynn et al. 2006; Zhang et al. 2012; Zhu et al. 2013a). Most researchers suggested it was open between the Late Permian and Early Triassic (Pan et al. 2004; Metcalfe 2006). The final amalgamation between the West Qiangtang and Lhasa blocks was probably no later than the Early Cretaceous (~ 151–140 Ma; Guynn et al. 2006; Kapp et al. 2007; Zhu et al. 2013a). This event recorded the final amalgamation of the microcontinents in the Sanjiang region (ESM Fig. A1G; Deng et al. 2014a).

The Indus–Yarlung–Zangbo suture extending for more than 2000 km from NW India via southern Tibet to NE India was formed by the closure of the Indus–Yarlung–Zangbo Neo-Tethys Ocean (Zhu et al. 2013a). The Neo-Tethys Ocean was open during the Triassic or the Middle to Late Jurassic, and closed at ~ 60–50 Ma marking the collision between the Indian and Asian continents (ESM Fig. A1H; Zhu et al. 2011, 2013a, 2015a). Influenced by the Indo-Asian continental collision since ~ 60–50 Ma, the Sanjiang region underwent strong intracontinental deformation with development of abundant strike-slip faults (e.g., the Jinshajiang and Ailaoshan–Red River strike-slip fault sysems) and thrust–nappe structures in the Cenozoic (Hou et al. 2007a; Deng et al. 2014b).

Eocene–Oligocene magmatism

During the Eocene–Oligocene, numerous intermediate–felsic igneous rocks were emplaced generally as small intrusions in the Sanjiang region, primarily within the East Qiangtang and South China blocks (Fig. 1B and ESM Fig. A11; Chung et al. 1997; Zhang and Xie 1997; Guo et al. 2005, 2006; Wang et al. 2018a). These igneous rocks are predominantly distributed along the NNW to NW-trending Jinshajiang–Ailaoshan fault zone, with length of ~ 2000 km and width of ~ 50–80 km (Fig. 1B; Chung et al. 1997, 2005; Campbell et al. 2014). Minor amounts of these rocks are present up to 50 km west of the fault zone in the East Qiangtang Block, and up to 270 km east of the fault zone in the South China Block (Fig. 1B; Guo et al. 2005; Lu et al. 2012).

Eocene–Oligocene ultrapotassic–potassic volcanic rocks are common in the southern and northern parts of the Sanjiang region, and they show close time–space relationships with the Eocene–Oligocene intermediate–felsic intrusions in the region (Fig. 1B; Turner et al. 1993, 1996; Deng 1998; Ding et al. 2003, 2007; Wang et al. 2005, 2016; Guo et al. 2005, 2006; Huang et al. 2010; Guo and Wilson 2019; Yakovlev et al. 2019; Shen et al. 2021). These volcanic rocks are mainly shoshonites, with minor dacites and rhyolites, and are characterized by enriched LREEs, LILEs, and Sr–Nd–Pb isotopic compositions (Turner et al. 1996; Deng 1998; Guo et al. 2005). It is widely accepted that the parental magmas for the mafic endmembers of these rocks were mainly derived from an enriched SCLM (Turner et al. 1993, 1996; Ding et al. 2003; Guo et al. 2005, 2006; Huang et al. 2010; Lu et al. 2015b; Yakovlev et al. 2019).

Eocene–Oligocene postcollisional porphyry Cu-Mo-Au deposits

The Eocene–Oligocene porphyry Cu-Mo-Au deposits, which are associated with the trachytic–rhyolitic porphyries among the Eocene–Oligocene intermediate–felsic intrusions in the Sanjiang region, form a belt mainly along the Jinshajiang–Ailaoshan fault zone and generally are regarded as the Jinshajiang–Ailaoshan porphyry Cu-Au-Mo belt (Fig. 1B; Table 1; Hu et al. 2004; Hou et al. 2006; Xu et al. 2012; Chang et al. 2017; Huang et al. 2019a). In the southern part of the belt, porphyry deposits mainly occur along the Ailaoshan–Red River fault system in the western margin of the South China Block and has been referred to as the Ailaoshan–Red River porphyry Au-Cu-Mo belt by some researchers (e.g., Fig. 1B; Xu et al. 2012). However, in the northern part of this belt, porphyry deposits mainly occur along the Jinshajiang fault system in the East Qiangtang Block and has been referred to as the Yulong porphyry Cu-Mo belt in many studies (Fig. 1B; Hou et al. 2003, 2007a, 2007b; Yang et al. 2014a).

The Ailaoshan–Red River porphyry Au-Cu-Mo belt extends for ~ 600 km with a NW-trend (Fig. 1B; Hou et al. 2006; Xu et al. 2012). It is located in the western margin of the South China Block (Fig. 1B). The most important deposits in this belt are the Beiya skarn ± porphyry Au deposit, the Yao'an porphyry Au deposit, and the Machangqing, Habo and Tongchang porphyry Cu-Mo(Au) deposits, plus several porphyry Cu-Mo-Au prospects such as Xiaolongtan and Fenshuiling (Table 1). These deposits together have a total Au metal endowment of > 330 t and Cu metal resource of ~ 1.4 Mt, with ~ 0.06 Mt Mo reserves (Hou et al. 2006, 2017; Xu et al. 2007; He et al. 2016; Li et al. 2016). The associated porphyry intrusions are mainly composed of monzogranite and granite, plus minor syenite and quartz syenite (Hou et al. 2006; Xu et al. 2012; Lu et al. 2013a; Deng et al. 2014b, 2015). Important characteristics of these deposits are listed in Table 1.

The Yulong porphyry Cu-Mo belt is ~ 400 km in length and 15–30 km in width, spatially controlled by the Jinshajiang fault system (Fig. 1B; Tang and Luo 1995; Hou et al. 2003, 2007a, 2017b; Yang et al. 2014a; Yang and Cooke 2019). It is located within the East Qiangtang Block, adjacent to the Permian–Triassic (*P–T*) bimodal volcanic belt (Jomda–Weixi arc) in the northeastern rim of the block (Fig. 1B). The belt contains seven porphyry Cu ± Mo deposits, namely Narigongma, Bomai, Yulong, Zhanaga, Mangzong, Malasongduo, and Duoxiasongduo from north to south, plus ~ 20 porphyry Cu ± Mo prospects, with total Cu and Mo reserves of ~ 8 and 0.8 Mt, respectively (Fig. 1B; Table 1; Hou et al. 2003; Yang et al. 2014a; Lin et al. 2018). The associated intrusions are dominated by felsic rocks, such as monzogranite and granite porphyries (Tang and Luo 1995; Hou et al. 2003; Yang et al. 2014a). The main features of representative deposits are listed in Table 1.

As mentioned above, the Neo-Tethyan subduction beneath the Eurasian continent is the last oceanic subduction event in the Greater Himalayan region. The eastward subduction of the Neo-Tethyan oceanic plate beneath the western margin of the Eurasian continent (in present coordinates) led to continental collision between India and Tibet in the Cenozoic, forming the Indus–Yarlung–Zangbo suture (suture VI on Fig. 1), which occurs more than several hundred km southwest of the Eocene–Oligocene Jinshajiang–Ailaoshan porphyry Cu-Au-Mo belt in the Sanjiang region. The timing of this collision remains a topic of debate, but most researchers now accept an age between 60 and 50 Ma (Zhu et al. 2015a, and references therein). Therefore, it is concluded that the Eocene to Oligocene porphyry Cu-Mo-Au deposits in the Sanjiang region were generated in a postcollisional environment (e.g., Hou et al. 2015a, 2015b; Yang et al. 2015).

Although porphyry Cu-Mo-Au deposits in the Jinshajiang–Ailaoshan belt in the Sanjiang region formed in a similar postcollisional backgroud, they are mainly distributed in two different blocks, i.e., the East Qiangtang Block in the north and Yangtze Craton in the south, correspondingly forming two different secondary belts, i.e., the Yulong porphyry Cu-Mo belt in the north, and the Ailaoshan–Red River porphyry Au-Cu-Mo belt in the south. The two blocks underwent different tectonic evolution, especially the oceanic subduction processes as presented above. Furthermore, compositions of fertile porphyries and associated metal endowments in the two belts are different as described above, i.e., the Yulong belt is dominated by felsic rocks and Cu-Mo mineralization, and the Ailaoshan–Red River belt is dominated by intermediate−felsic rocks and Au-Cu-Mo mineralization. Because of the tectonic differences between the two belts, especially the early oceanic subduction processes, petrogenesis of fertile porphyries in the two belts are discussed separately. In this study, fertile porphyry samples were collected from three deposits (e.g., Machangchang, Tongchang and Beiya) in the Ailaoshan–Red River belt, and analyzed for zircon U−Pb ages, Hf−O isotopes, zircon and amphibole chemical compositions, and whole-rock chemical and Sr−Nd isotope compositions. These new petrological-geochemical data together with the previously published data for fertile porphyries in both the Ailaoshan–Red River porphyry Au-Cu-Mo belt and the Yulong porphyry Cu-Mo belt are used to decipher the magmatic source, magmatic fO_2-H_2O characteristics, and major controls on magmatic fO_2-H_2O.

Geology of the Eocene–Oligocene porphyry Cu-Mo-Au deposits

Machangqing porphyry Cu-Mo deposit

The Machangqing deposit contains ~ 60 Mt ore with average grades of 0.44% Cu, 0.03% Mo, and 0.03 g/t Au (Hou et al. 2006). Cu-Mo mineralization in the deposit is hosted by a granite porphyry stock intruding Lower Ordovician and Lower Devonian limestone and sandstone (Table 1; ESM Figs. A2A-B; Xu et al. 2012, 2015, 2016a). The exposed area of this intrusion is ~ 1.3 km^2. The granite porphyries are grey to light pink, with a porphyritic texture. Primary phenocrysts are K-feldspar, plagioclase, quartz, amphibole, and biotite in a cryptocrystalline matrix and locally in a phanerocrystalline matrix, with main accessory minerals of titanite, zircon, and apatite (ESM Fig. A3A). Alteration zones in this deposit can be divided into an inner K-silicate alteration zone at depth and the outer sericite and weak argillic alteration zones at shallower levels, surrounded by a skarn or hornfels zone in the contact between the granite porphyry intrusion and the country rocks (Bi et al. 2009; Lu et al. 2013a). Abundant secondary biotite formed by alteration of amphibole and abundant sericite formed by alteration of plagioclase characterize the K-silicate and sericite alteration, respectively (ESM Figs. A3B-C). The alteration is accompanied by porphyry-style disseminated and veinlet-type molybdenite and chalcopyrite mineralization. The skarn-style Cu(Fe) mineralization is characterized by massive or disseminated chalcopyrite, magnetite, and pyrite that is restricted to the skarn and associated hornfels zones. From the granite porphyry stock toward the country rock, there is a general metal zonation, i.e., Mo → Mo (Cu) → Cu (Mo) → Cu (Fe) (ESM Fig. A2B). This zonation is consistent with decreasing ore-forming temperatures from the causative intrusion to distal area (Lu et al. 2013a).

Tongchang porphyry Cu-Mo deposit

The Tongchang deposit is composed of the Tongchang ore zone in the east and Chang'anchong ore zone in the west (ESM Fig. A4A). The Tongchang ore zone contains 8,621 t Cu and 17,060 t Mo with 1.24% Cu and 0.218% Mo, whereas the Chang'anchong ore zone contains 29,337 t Cu and 13,310 t Mo with 1.48% Cu, and 0.13% Mo (Xu et al. 2015). Three stages of magmatism are recognised in the Tongchang deposit: an early stage of fine-grained syenites and minor pyroxene syenites, a middle stage of quartz syenite porphyries, and a late stage of syenite porphyries, diabases and diabase gabbros (ESM Fig. A4A; Xu et al. 2019). Cu-Mo mineralization in both ore zones is hosted by the quartz syenite porphyry intrusions of the middle stage (Table 1; ESM Figs. A4A-C; Xu et al. 2015), which were emplaced into Middle Silurian limestone and sandstone (ESM Fig. A4A). The intrusions form stocks and dykes with outcrop areas of ~ 0.2 km^2 at the Tongchang ore zone, and > 0.18 km^2 at Chang'anchong ore zone, respectively (Xu et al. 2012). Quartz syenite porphyries in both ore zones have phenocrysts of K-feldspar, plagioclase, quartz, hornblende, and biotite in a phanerocrystalline groundmass (ESM Fig. A3D). Titanite, zircon, and apatite are the main accessory minerals. The ore zones have similar alteration mineral assemblages and mineralization styles (ESM Figs. A4B-C; Xu et al. 2016a). The interior of the intrusions exhibit K-silicate alteration at depth and sericite alteration at shallower depths, expressed by abundant secondary biotite and sericite, respectively (ESM Figs. A3E-F). Along with the alteration, abundant spot-, and veinlet-disseminated molybdenite and minor veinlet-disseminated chalcopyrite mineralization occurs in the interior of the intrusions. Skarn alteration at the contacts between the intrusions and the country rocks is characterized by abundant skarn minerals (e.g., garnet, scapolite, tremolite, epidote, and diopside), and is accompanied by massive magnetite and massive and disseminated sulfide (e.g., chalcopyrite and pyrite) mineralization (ESM Figs. A4B-C). Similar to the Machangqing deposit, a clear metal zonation (from Mo-Cu to Pb–Zn) is present from the intrusion toward the country rock, due to decreasing ore-forming temperatures outwards from the causative intrusion.

Beiya skarn ± porphyry Au deposit

The Beiya deposit is divided into six ore segments: Wandongshan, Hongnitang, Weiganpo, Bijiashan, Guogaishan, and Jingouba (ESM Fig. A5A). The deposit contains ~ 130 Mt of ore with average grades of 2.47 g/t Au, 0.52% Cu, and 33.3% Fe. The mineralization is hosted by quartz syenite porphyry intrusions which emplaced into Lower Triassic sandstone and Middle Triassic limestone (Table 1; ESM Fig. A5B). The porphyry intrusions are mainly exposed in the Wandongshan and Hongnitang ore segments (ESM Fig. A5A). Phenocrysts in the Beiya quartz syenite porphyries are mainly composed of K-feldspar, plagioclase, and quartz (ESM Fig. A3G), with minor amphibole and biotite (Bao et al. 2017). The quartz syenite porphyries have undergone pervasive sericite alteration, characterized by abundant sericite alteration of plagioclase, amphibole, and biotite (ESM Figs. A3H-I). Three types of mineralization are present in the Beiya deposit: skarn Au-Fe-Cu mineralization, porphyry Au-Cu(Mo) mineralization, and supergene Au-Fe mineralization in the weathered zones of both porphyry and skarn ore bodies (Lu et al. 2013a; Deng et al. 2015; Li et al. 2016; Zhou et al. 2017a). Porphyry-style Au-Cu(Mo) mineralization (Orebody KT50; ESM Fig. A5B) is characterized by quartz-pyrite-chalcopyrite stockwork veins, associated with potassic and sericite alteration, providing 1.33 Mt ore with Au grade of 2.87 g/t (3.8 t Au; Lu et al. 2013a). Skarn Au-Cu-Fe mineralization provides the majority of Au resources and is developed within the contact zone between the intrusion and the Middle Triassic limestone sequences in the Wandongshan area. It is characterized by massive magnetite ores with disseminated pyrite and chalcopyrite. In the Wandongshan segment, ore body KT52 with typical skarn Au-Cu-Fe mineralization (ESM Fig. A5B) is the largest individual orebody in the Beiya deposit, containing 87 Mt at 2.4 g/t Au, 90 Mt at 34% Fe, and 112 Mt at 0.34% Cu (Zhou et al. 2017a).

Yulong porphyry Cu-Mo deposit

The Yulong porphyry Cu-Mo deposit, which contains over 6.5 Mt Cu with average grades of 0.38% Cu, 0.04% Mo, and 0.35 g/t Au, is the largest in the Yulong porphyry Cu-Mo belt (Hou et al. 2003; Xu et al. 2012, 2014, 2016a). Cu-Mo mineralization at the Yulong deposit is hosted by the Yulong monzogranite porphyry stock with an outcrop area of ~ 0.64 km^2, which was emplaced into the Triassic sandstone and limestone at ~ 41 Ma (ESM Figs. A6A-B; Li et al. 2012; Xu et al. 2012). The monzogranite porphyries are light grey to light pink with a porphyritic texture, and they contain K-feldspar, plagioclase, quartz, biotite, and amphibole as the dominant phenocrysts in a cryptocrystalline groundmass (Xu et al. 2016a). Zircon, apatite, and titanite constitute the principal accessory minerals. Spatially, alteration zones of the Yulong deposit range from an inner K-silicate alteration zone at depth, out through quartz-sericite and argillic alteration zones at relatively shallow level, to an outer propylitic zone (ESM Figs. A6A-B; Hou et al. 2003, 2006; Li et al. 2012). The K-silicate alteration is characterized by replacement of amphibole by secondary biotite, and the sericite alteration is characterized by development of sericite by replacing plagioclase and even secondary biotite (Huang et al. 2019a, 2019b). Hydrothermal alteration zones have locally overprinted earlier formed contact metamorphic zones that show a crude zonation from inner hornfels, through skarn alteration to marble (ESM Figs. A6A-B; Hou et al. 2003; Li et al. 2012). The Yulong deposit is composed of a ring-shaped high-grade Cu-Au mineral zone (~ 3 Mt Cu with > 1% Cu and 100 t Au with 4 g/t Au) overlying and surrounding a pipe-like, steeply dipping, veinlet-disseminated Cu-Mo orebody within the monzogranite porphyry stock (Hou et al. 2006).

Analytical methods

Porphyry samples were collected from the outcrops, open pits and tunnels of the Machangqing, Tongchang, and Beiya porphyry deposits (ESM Table A1). Fresh or least-altered samples were selected for whole-rock major and trace elemental, and Sr−Nd isotope, zircon U−Pb dating, Hf−O isotope, and trace elemental, and amphibole major elemental analyses. Locations and brief descriptions for these samples are presented in ESM Table A1. The detailed analytical methods can be found in ESM Appendix 1. Briefly, whole-rock major element analyses were carried out using a PANalytical Axios–advance (Axios PW4400) X-ray fluorescence spectrometer (XRF) and a Thermo Fisher (ARL Perform' X 4200) XRF at the State Key Laboratory of Ore Deposit Geochemistry (SKLODG), Institute of Geochemistry, Chinese Academy of Sciences, Guiyang, China. Whole-rock trace element analyses were finished using a Perkin-Elmer ELAN-DRC-e inductively coupled plasma mass spectrometer (ICP-MS) and a PlasmaQuant-MS Elite ICP-MS at the SKLODG. Whole-rock samples for Sr–Nd isotopic analyses were spiked and dissolved in Teflon bombs with $HF + HNO_3$ acid, and separated by conventional cation-exchange techniques. The isotopic measurements were performed on a Thermo Fisher Scientific Neptune plus multi-collector inductively coupled plasma mass spectrometer (MC-ICP-MS) at the SKLODG. Zircon separates were separated from rock sample using standard density and magnetic separation techniques. The mineral grains were hand-picked and mounted in epoxy resin discs, and then polished. Cathodoluminescence (CL) images of the zircon grains used for textural observation were obtained using a field emission scanning electron microscope (JSM-7800F, Japan Electronic Co., Ltd.) at the SKLODG. Zircon oxygen isotopes were measured using a CAMECA IMS 1280 SIMS at the Institute of Geology and

Geophysics, Chinese Academy of Sciences, Beijing, China. Zircon in situ Hf isotopic analysis was carried out using a Neptune Plus MC-ICP-MS equipped with a Geolas 2005 excimer ArF laser ablation systemat the state Key Laboratory of Geological Processes and Mineral Resources, China University of Geosciences (Wuhan), China. Zircon Lu−Hf isotopic measurements were performed on the same locations of the same zircon grains that were previously analyzed for oxygen isotopes. Zircon U–Pb isotopic and trace element compositions were simultaneously measured using a pulsed GeoLas 193-nm ArF excimer laser (Lambda Physik, Göttingen, Germany) plus an ICP-MS (Agilent 7900) at the SKLODG. The analyses were performed on the same zircon grains that were analyzed previously for O−Hf isotopic compositions. Major element compositions of amphibole were determined using a JXA8530F-plus field emission electron microscope using wavelength-dispersive spectroscopy at the SKLODG.

Results

Geochronology

Zircon U−Pb results of the selected mineralized porphyry samples from the Machangqing, Tonchang, and Beiya deposits are presented in ESM Table A2 and illustrated in the Tera-Wasserburg concordia diagrams with the reported intercept ages (ESM Fig. A7). Under CL imaging, most of the zircon grains show clear magmatic oscillatory zoning, and minor zircon grains have inherited cores surround by rims with clear magmatic oscillatory zoning (ESM Fig. A8). Zircon U−Pb dating, Hf−O isotope, and trace element measurements were performed on locations with clear magmatic oscillatory zoning (ESM Fig. A8); this, combined with Th/U ratios of >0.1 for all the analyzed zircons (ESM Table A2), suggest a magmatic origin. Samples BXC920, SMC907, and LDS906 are collected from the mineralized granite porphyries of the Machangqing deposit; zircon grains from the three samples yielded intercept ages of 34.8 ± 0.4 Ma (2σ, MSWD = 0.37, $n=20$), 35.3 ± 0.5 Ma (2σ, MSWD = 0.21, $n=17$), and 35.3 ± 0.4 Ma (2σ, MSWD = 0.46, $n=20$), respectively (ESM Figs. A7A-C). Samples TC920 and CA907 are collected from the mineralized quartz syenite porphyries of the Tongchang deposit; zircon grains from the two samples yielded intercept ages of 35.0 ± 0.4 Ma (2σ, MSWD = 0.21, $n=23$), and 35.4 ± 0.5 Ma (2σ, MSWD = 0.21, $n=18$), respectively (ESM Figs. A7D-E). Sample BY13-1 is collected from the mineralized quartz syenite porphyries of the Beiya deposit, and zircon grains from this sample yielded an intercept age of 35.2 ± 0.5 Ma (2σ, MSWD = 1.8, $n=45$; ESM Fig. 7F).

Whole-rock geochemistry

The whole-rock geochemical data for the selected 45 mineralized porphyry samples from the Machangqing, Tonchang, and Beiya deposits are summarized in Table 2 with detailed data presented in ESM Table A3**,** and plotted in Figs. 2 and 3. They are relatively unaltered based on the microscopic petrographic observation and have relatively low loss-on-ignition (LOI) contents of 0.41–2.65 wt%. The Machangqing, Tonchang, and Beiya porphyry samples are all felsic (SiO_2 = 65.7–71.2 wt%) and metaluminus to weakly peraluminus [molar $Al_2O_3/(CaO+Na_2O+K_2O)$ = 0.9–1.2], but the Machangqing and Beiya samples are slightly more SiO_2-enriched than the Tongchang samples (Table 2; ESM Table A3; Fig. 2). They have high alkali contents (Na_2O+K_2O = 8.13–11.34 wt%), and in the diagram of immobile ratios (Zr/TiO_2 versus Nb/Y; Winchester and Floyd 1977), these samples generally plot in the syenite field, suggesting that they are genuinely alkaline in composition. The porphyry samples are all characterized by enrichment in LILEs (LREE, Rb, Ba, Th, U, K, and Pb), and depletion in HFSEs (Ta, Nb, and Ti; Fig. 3A, B), but the Beiya samples have notably lower REE concentrations than the Machangqing and Tongchang samples (Fig. 3A, B). Most samples have slightly negative Eu anomalies with Eu_N/Eu_N^* values of 0.63 – 0.94, and high Sr/Y ratios of 75 ± 31.

Sr−Nd−Hf−O isotopes

The Sr−Nd isotopes for the selected thirteen mineralized porphyry samples from the Machangqing and Tonchang deposits, and zircon Hf−O isotopes for the selected six mineralized porphyry samples from the Machangqing, Tonchang, and Beiya deposits are presented in Table 2 and ESM Tables A2-A3, and they are also illustrated in Figs. 4, 5, and 6. Eight mineralized porphyry samples from the Machangqing deposit have initial $^{87}Sr/^{86}Sr$ ratios and $\varepsilon_{Nd}(t)$ values of 0.7068–0.7069 and −5.3 to −5.0, respectively. Five mineralized porphyry samples from the Tongchang deposit have initial $^{87}Sr/^{86}Sr$ ratios and $\varepsilon_{Nd}(t)$ values of 0.7070–0.7071 and −6.3 to −5.9, respectively (Table 2; ESM Table A3).

Sixty-four zircon Hf−O isotopic analyses for three mineralized porphyry samples from the Machangqing deposit were obtained in this study. The $\varepsilon_{Hf}(t)$ ratios range from −4.6 to 2.9 (average = 0.4 ± 0.3), with T_{DM2} model ages from 924 to 1401 Ma (Fig. 5A). The $\delta^{18}O$ values of these zircon crystals range from 5.9 to 6.8‰ (average = 6.3 ± 0.3‰). Forty-five zircon Hf−O isotopic analyses for two mineralized porphyry samples from the Tongchang deposit yielded $\varepsilon_{Hf}(t)$ ratios of −5.2 to 0.4 (average = -1.5 ± 0.3) and the T_{DM2} model ages from 1084 to 1437 Ma (Fig. 5A; ESM Table A2). The $\delta^{18}O$ values of these zircon grains vary from 6.1 to 7.7‰, (average = 6.8 ± 0.3‰; Fig. 6; ESM Table A2). Twenty-eight zircon Hf−O isotopic anlyses for one mineralized porphyry sample from the Beiya

Table 2 Summary of whole-rock geochemistry and Sr−Nd isotopes of the Machangqing, Tongchang, and Beiya Cu-Mo-Au fertile porphyries in the Sanjiang region, SW China

Pluton/deposit	Machangqing			Tongchang			Beiya		
Rock type	Granite porphyry			Quartz syenite porphyry			Granite porphyry		
Value	Minimum	Maximum	Average	Minimum	Maximum	Average	Minimum	Maximum	Average
Whole-rock major element compositions (wt %) and calculated parameters									
SiO_2	68.65	71.20	69.61	65.67	66.70	66.20	66.37	70.03	68.19
Al_2O_3	14.56	15.32	14.91	14.87	15.47	15.26	14.20	15.79	15.04
Fe_2O_{3Total}	1.77	3.05	2.50	2.89	3.09	3.04	1.37	3.60	2.27
MgO	0.94	1.25	1.11	1.86	2.01	1.92	0.14	0.46	0.31
CaO	1.34	2.33	1.83	2.81	3.04	2.89	0.08	2.20	0.90
Na_2O	4.13	4.62	4.35	3.72	4.29	3.98	0.79	4.46	3.71
K_2O	3.66	5.24	4.45	4.53	5.09	4.76	5.81	10.55	6.67
MnO	0.02	0.04	0.03	0.04	0.05	0.05	0.01	0.15	0.06
P_2O_5	0.14	0.20	0.17	0.26	0.27	0.26	0.04	0.16	0.11
TiO_2	0.26	0.35	0.30	0.38	0.39	0.39	0.20	0.40	0.25
LOI	0.41	1.18	0.58	0.74	2.65	1.37	0.62	2.31	1.45
Total	99.48	100.41	99.82	99.17	100.85	100.12	98.25	100.00	99.30
K_2O+Na_2O	8.13	9.38	8.80	8.25	8.92	8.74	8.95	11.34	10.38
A/CNK	0.94	1.01	0.97	0.86	0.94	0.90	0.87	1.20	1.01
Whole-rock trace element compositions (ppm) and calculated parameters									
V	32.7	71.7	39.1	56.0	60.2	58.3	19.0	33.0	24.9
Sc	5.13	8.30	5.73	8.00	10.7	9.25	3.30	5.90	4.36
Cr	24.8	34.8	28.6	41.7	58.5	52.1	1.00	9.00	4.04
Co	3.98	10.1	5.34	8.16	9.59	9.01	56.8	179	85.2
Ni	11.5	18.0	14.0	17.3	23.7	21.3	0.900	4.80	2.62
Rb	110	257	174	151	241	188	109	192	157
Ba	776	4405	1276	1530	1850	1720	1770	7920	2415
Sr	638	1458	775	880	1220	1003	362	881	681
Y	12.7	19.0	15.0	12.3	14.7	14.1	5.20	12.8	8.36
Zr	148	250	175	108	156	132	27.5	103	54.9
Hf	4.27	6.01	4.86	3.37	4.16	3.67	1.30	3.30	2.10
Nb	12.4	16.3	13.8	9.45	11.2	10.1	9.10	13.7	11.5
Ta	0.929	1.13	0.995	0.749	0.926	0.831	0.560	0.810	0.688
Pb	8.62	38.3	25.8	29.0	35.0	33.0	17.4	68.1	29.7
Th	27.0	41.1	32.0	18.0	23.2	21.6	10.4	14.7	12.9
U	5.33	8.89	6.88	5.80	9.23	6.94	1.80	5.30	3.20
La	55.4	128	68.1	53.1	65.5	60.9	6.70	43.6	20.9
Ce	92.9	227	117	92.4	113	105	18.4	58.8	37.7
Pr	10.2	24.7	12.7	9.87	12.0	11.4	1.94	7.84	4.23
Nd	34.8	87.2	44.2	34.0	41.1	39.1	6.80	28.3	15.2
Sm	5.28	12.6	6.71	5.63	6.71	6.45	1.31	4.86	2.81
Eu	0.963	2.05	1.31	1.35	1.65	1.55	0.360	1.32	0.690
Gd	3.61	7.82	4.56	4.29	5.08	4.82	1.04	3.96	2.21
Tb	0.472	0.935	0.588	0.560	0.662	0.630	0.170	0.450	0.292
Dy	2.26	3.86	2.73	2.40	2.89	2.77	0.910	2.20	1.53
Ho	0.412	0.642	0.491	0.457	0.537	0.515	0.180	0.390	0.289
Er	1.15	1.75	1.34	1.19	1.46	1.38	0.520	0.990	0.756
Tm	0.159	0.226	0.184	0.151	0.191	0.176	0.080	0.140	0.108
Yb	1.10	1.52	1.26	0.979	1.22	1.15	0.580	0.970	0.726
Lu	0.159	0.207	0.181	0.156	0.181	0.171	0.100	0.180	0.128

Table 2 (continued)

Pluton/deposit	Machangqing			Tongchang			Beiya		
Rock type	Granite porphyry			Quartz syenite porphyry			Granite porphyry		
Value	Minimum	Maximum	Average	Minimum	Maximum	Average	Minimum	Maximum	Average
Eu_N/Eu_N^*	0.632	0.811	0.729	0.828	0.888	0.851	0.714	0.944	0.845
Y/Yb	11.3	13.5	11.8	11.8	12.7	12.2	8.00	17.3	11.4
Nb/Ta	13.0	17.2	13.9	11.6	12.8	12.2	15.3	18.3	16.6
Nb/U	13.0	17.2	13.9	11.6	12.8	12.2	2.17	5.17	3.74
La/Yb	47.6	90.8	53.6	50.8	54.6	53.0	9.71	58.9	28.5
Sr/Y	43.6	76.7	51.3	61.1	83.0	71.4	28.3	168	88.5
Dy/Yb	1.98	2.74	2.15	2.37	2.45	2.41	1.40	2.97	2.09
Whole-rock Sr−Nd isotopic compositions									
$^{87}Rb/^{86}Sr$	0.401888	1.070356	0.715509	0.400833	0.792449	0.552732			
$^{147}Sm/^{144}Nd$	0.090095	0.095938	0.092441	0.097614	0.100650	0.099655			
$^{87}Sr/^{86}Sr$	0.707031	0.707382	0.707203	0.707271	0.707466	0.707341			
2σ	0.000009	0.000011	0.000009	0.000006	0.000010	0.000008			
$^{143}Nd/^{144}Nd$	0.512344	0.512359	0.512352	0.512292	0.512315	0.512302			
2σ	0.000008	0.000010	0.000009	0.000002	0.000004	0.000002			
Age (Ma)	35	35	35	35	35	35			
I_{sr}	0.70683	0.70690	0.70685	0.70703	0.70710	0.70707			
$\varepsilon_{Nd}(t)$	−5.3	−5.0	−5.1	−6.3	−5.9	−6.1			

deposit show $\varepsilon_{Hf}(t)$ values of -5.3 to 4.5 (average = −1.8 ± 0.7) and T_{DM2} model ages from 823 to 1446 Ma (Fig. 5A; ESM Table A2). The $\delta^{18}O$ values of these zircon crystals vary from 6.9 to 9.0‰ (average = 7.5 ± 0.3‰; Fig. 6; ESM Table A2).

Zircon and amphibole chemistry

Zircon trace element chemistry of the selected mineralized porphyry samples from the Machangqing, Tonchang and Beiya deposits are presented in ESM Table A2. Apatite and titanite are common mineral inclusions in zircon, and during LA-ICP-MS trace element analysis of zircon, these small mineral inclusions are easily encountered (Lu et al. 2016; Zhu et al. 2018). Therefore, we have taken La > 1 ppm and Ti > 20 ppm as indicators of apatite and titanite contamination, and screened out data with values higher than those thresholds. Chondrite-normalized REE patterns of zircon show relative enrichment in HREEs and depletion in LREEs, with small negative Eu and strongly positive Ce anomalies (ESM Fig. A8). Titanium-in-zircon temperatures that are usually used to reflect the magmatic crystallization temperatures, were calculated using the method of Ferry and Watson (2007), where it is assumed that SiO_2 activity = 1 and TiO_2 activity = 0.7, because of the presence of quartz and titanite in the porphyries. Titanium-in-zircon temperatures are summarized in Table 3 with details listed in ESM Table A2. They are 570−798 °C (average = 689 ± 41 °C, 1σ) for the Machangqing porphyry, 635−849 °C (average = 715 ± 40 °C, 1σ) for the Tongchang porphyry, and 531−849 °C (average = 710 ± 84 °C, 1σ) for the Beiya porphyry. Using ratios of Ce, U, and Ti in zircon, Loucks et al. (2020) developed a method to estimate the relative oxidation state of parental melts by zircon composition. Using this method, calculated ΔFMQ values for the selected porphyry samples from the Machangqing, Tongchang and Beiya deposits are 0.8−4.5 (average = 2.1 ± 0.7, 1σ), 0.7−3.0 (average = 1.9 ± 0.4, 1σ) and 0.1−4.1 (average = 1.2 ± 0.9, 1σ), respectively (Table 3; ESM Table A2). Abundant amphibole phenocrysts are present in the mineralized porphyries. Amphibole chemical compositions from the Machangqing and Tongchang deposits are presented in ESM Table A4. Amphibole chemical compositions can be used to estimate magmatic oxidation state, crystallization temperatures, and pressures, as well as water contents (e.g., Ridolfi et al. 2010; Locock 2014; Mutch et al. 2016; Zhu et al. 2018; Li et al. 2019). All the selected amphibole phenocrysts are magmatic (ESM Figs. A3A and D). The calculated results of these parameters are presented in ESM Table A4 and summarized in Table 4. Crystallization temperatures and pressures for the Machangqing porphyry samples range from 714 to 912 °C (average = 771 ± 44 °C, 1σ) and from 1.1 to 4.3 kbar (average = 1.9 ± 0.7 kbar, 1σ), respectively, with calculated ΔFMQ values and magmatic water contents of 0.7 to 2.9 (average = 2.1 ± 0.6, 1σ) and 2.7 to 4.2 wt% (average = 3.5 ± 0.3 wt%, 1σ), respectively. For the Tongchang samples, their calculated temperatures range from 706 to 953 °C (average = 806 ± 41 °C, 1σ) and pressures from 1.0 to 5.4 kbar (average = 2.6 ± 0.8 kbar, 1σ), with calculated ΔFMQ values of 0.7–3.0 (average = 1.6 ± 0.6, 1σ) and magmatic water contents of 2.5–4.4 wt% (average = 3.8 ± 0.3 wt%, 1σ).

Table 3 Summary of magmatic oxygen fugacity (ΔFMQ) and Ti-in-zircon temperatures (°C) calculated from zircon compositions for the Eocene–Oligocene fertile porphyries and associated Cu-Mo-Au deposits in the Sanjiang region, SW China, and those for Cu fertile porphyry plutons in Chile and Central Asian orogenic belt

Pluton/Deposit	Number of analyzed zircon spots	ΔFMQ	$T_{\text{Ti-in-Zir temperature}}$ (°C)	Reference
Cu fertile arc porphyry plutons in the Central Asian Orogenic belt				
Baogutu	6	0.3 ~ 0.5, average = 0.4 ± 0.1 (± SD)	777 ~ 807, average = 793 ± 11 (± SD)	Shen et al. 2015
Borly	5	−0.6 ~ 1.5, average = 0.0 ± 0.8 (± SD)	719 ~ 824, average = 771 ± 38 (± SD)	
Tuwu-Yandong	6	1.1 ~ 1.8, average = 1.4 ± 0.2 (± SD)	662 ~ 708, average = 668 ± 17 (± SD)	
Koksai	5	1.0 ~ 1.5, average = 1.3 ± 0.2 (± SD)	682 ~ 720, average = 707 ± 15 (± SD)	
Erdenet	8	0.3 ~ 1.0, average = 0.7 ± 0.3 (± SD)	748 ~ 812, average = 786 ± 21 (± SD)	
Aktogai	8	0.7 ~ 1.3, average = 1.0 ± 0.2 (± SD)	736 ~ 806, average = 766 ± 23 (± SD)	
Kounrad	11	−0.6 ~ 1.9, average = 0.7 ± 0.7 (± SD)	678 ~ 765, average = 722 ± 26 (± SD)	
Nurkazghan	10	−0.5 ~ 0.3, average = −0.1 ± 0.3 (± SD)	716 ~ 792, average = 768 ± 24 (± SD)	
Bozshakol	17	0.1 ~ 1.3, average = 0.8 ± 0.3 (± SD)	683 ~ 748, average = 716 ± 20 (± SD)	
Cu fertile arc porphyry plutons in Chile				
El Teniente	6	−0.1 ~ 1.4, average = 0.8 ± 0.5 (± SD)	750 ~ 813, average = 732 ± 45 (± SD)	Muñoz et al. 2012
	7	−2.8 ~ 1.4, average = 0.4 ± 1.3 (± SD)	614 ~ 781, average = 685 ± 41 (± SD)	
	6	0.3 ~ 1.5, average = 1.0 ± 0.4 (± SD)	746 ~ 778, average = 681 ± 37 (± SD)	
Cu-Mo-Au fertile porphyry plutons in the Sanjiang region				
Yulong	87	−0.3 ~ 3.8, average = 1.8 ± 0.8 (± SD)	628 ~ 960, average = 696 ± 51 (± SD)	Li et al. 2012
Machangqing	59	0.8 ~ 4.5, average = 2.1 ± 0.7 (± SD)	570 ~ 798, average = 689 ± 41 (± SD)	this study
Habo	19	0.1 ~ 1.6, average = 0.7 ± 0.4 (± SD)	636 ~ 768, average = 704 ± 54 (± SD)	Yang et al. 2017
Tongchang	24	0.9 ~ 2.6, average = 1.5 ± 0.5 (± SD)	609 ~ 774, average = 736 ± 46 (± SD)	Yang et al. 2017
	21	1.4 ~ 2.4, average = 1.8 ± 0.3 (± SD)	668 ~ 753, average = 702 ± 18 (± SD)	Xu et al. 2019
	28	0.9 ~ 2.6, average = 1.6 ± 0.4 (± SD)	609 ~ 774, average = 732 ± 44 (± SD)	Yang et al. 2017
	43	0.7 ~ 3.0, average = 1.9 ± 0.4 (± SD)	635 ~ 849, average = 715 ± 40 (± SD)	this study
Yao'an	23	1.4 ~ 3.3, average = 2.6 ± 0.5 (± SD)	665 ~ 1104, average = 676 ± 34 (± SD)	Xu et al. 2016a
Bieya	47	0.1 ~ 4.1, average = 1.2 ± 0.9 (± SD)	631 ~ 849, average = 710 ± 84 (± SD)	This study

Discussion

Timing of the Jinshajiang–Ailaoshan porphyry Cu-Au-Mo belt

Zircon U−Pb data for the Beiya, Tongchang, and Machangqing mineralized porphyries show a magmatic pulse of 35.4−34.8 Ma. The newly obtained age data are consistent with the published age data (ESM Table A5). We have summarized the published age data of the Eocene–Oligocene fertile porphyries and associated Cu-Mo-Au deposits in the Jinshajiang–Ailaoshan belt (ESM Table A5), and plotted them in histograms (Fig. 7A, B). Zircon U−Pb dating indicates that the porphyry emplacement in the Jinshajiang–Ailaoshan belt occurred between 43.8 and 32.8 Ma (ESM Table A5; Fig. 7A). Molybdenite Re−Os and hydrothermal mineral (e.g., titanite, allanite, and monazite) U-Th-Pb dating shows that the porphyry Cu-Mo-Au mineralization in the Jinshajiang–Ailaoshan belt occurred between 42.3 and 31.7 Ma (ESM Table A5; Fig. 7B), consistent with zircon U−Pb ages of the host porphyries (ESM Table A5; Fig. 7A). These age data collectively define a duration of ~ 12 m year for porphyry magmatism and associated Cu-Mo-Au mineralization in the Jinshajiang–Ailaoshan belt.

Petrogenesis of fertile porphyries in the Jinshajiang–Ailaoshan Cu-Au-Mo belt

Ailaoshan–Red River porphyry Au-Cu-Mo belt

Given the similarity to published data for the corresponding deposits in the Ailaoshan–Red River belt, we discuss their petrogenesis based on all available geochemical data (Figs. 2–6 and 8). The published whole-rock elemental and Sr−Nd and zircon Hf−O isotope results have been collected in ESM Tables A6-A7. The corresponding data for typical arc fertile porphyries are presented in ESM Table A8 for comparison. Given the potassic alteration for published data of the Beiya deposit (e.g., Lu et al. 2013a), the samples with K_2O contents higher than 8 wt% have been removed for major elemental plots (Fig. 2) in order to minimize the effects of potassic alteration.

The fertile porphyries in the Ailaoshan–Red River belt generally have high SiO_2 and total alkaline contents. They

Table 4 Summary of relevant parameters calculated from amphibole compositions for the Eocene–Oligocene Cu-Mo-Au fertile porphyries in the Sanjiang region, SW China

Pluton/Deposit	Number of analyzed amphibole spots	Calculated relevant parameters for parental melts				Reference
		T (°C)	ΔFMQ	H_2O_{melt} (wt%)	P (kbar)	
Narigongma	7	705−767, average = 734 ± 23 (±SD)	3.1−3.6, average = 3.4 ± 0.2 (±SD)	–	0.86−1.64, average = 1.24 ± 1.3 (±SD)	Hao et al. 2010
Yulong	1	887	2.0	3.0	3.29	Wang 2013
	4	796−843, average = 815 ± 33 (±SD)	1.6−2.2, average = 2.0 ± 0.2 (±SD)	–	2.20−2.91, average = 2.44 ± 0.42 (±SD)	Jiang et al. 2006
	33	709−848, average = 789 ± 37 (±SD)	1.5−3.2, average = 2.2 ± 0.5 (±SD)	2.8−4.6, average = 3.9 ± 0.5 (±SD)	1.04−3.27, average = 2.20 ± 0.61 (±SD)	Huang et al. 2019a
Machangqing	11	744−796, average = 777 ± 15 (±SD)	2.6−3.1, average = 2.8 ± 0.2 (±SD)	2.9−3.6, average = 3.3 ± 0.2 (±SD)	1.37−1.88, average = 1.65 ± 0.14 (±SD)	Wang 2013
	5	687−828, average = 770 ± 59 (±SD)	1.9−3.6, average = 2.6 ± 0.7 (±SD)	2.3−4.2, average = 3.6 ± 0.7 (±SD)	0.78−2.75, average = 1.92 ± 0.83 (±SD)	Bi et al. 2009
	16	687−770, average = 724 ± 21 (±SD)	2.5−3.3, average = 3.0 ± 0.2 (±SD)	3.3−4.0, average = 3.7 ± 0.2 (±SD)	0.89−1.88, average = 1.28 ± 0.25 (±SD)	Shen et al. 2018
	36	714−912, average = 771 ± 43 (±SD)	0.7−2.9, average = 2.1 ± 0.6 (±SD)	2.7−4.2, average = 3.5 ± 0.3 (±SD)	1.12−4.34, average = 1.87 ± 0.67 (±SD)	this study
Tongchang	11	738−946, average = 875 ± 70 (±SD)	0.6−2.8, average = 1.5 ± 0.7 (±SD)	3.2−4.8, average = 3.9 ± 0.5 (±SD)	1.30−5.52, average = 3.81 ± 1.45 (±SD)	Wang 2013
	109	706−953, average = 806 ± 41 (±SD)	0.7−3.0, average = 1.6 ± 0.6 (±SD)	2.5−4.4, average = 3.8 ± 0.3 (±SD)	1.01−5.40, average = 2.58 ± 0.78 (±SD)	this study
Beiya	9	660−759, average = 709 ± 29 (±SD)	1.9−2.8, average = 2.5 ± 0.3 (±SD)	2.5−4.1, average = 3.3 ± 0.5 (±SD)	0.73−1.63, average = 1.18 ± 0.33 (±SD)	Bao et al. 2017
Yao'an	3	892−954, average = 915 ± 27 (±SD)	1.2−1.7, average = 1.5 ± 0.2 (±SD)	2.1−2.4, average = 2.3 ± 0.1 (±SD)	3.47−4.91, average = 3.99 ± 0.65 (±SD)	Wang 2013
	8	809−858, average = 842 ± 17 (±SD)	1.6−2.0, average = 1.8 ± 0.1 (±SD)	2.6−3.3, average = 3.0 ± 0.2 (±SD)	2.47−3.24, average = 2.95 ± 0.25 (±SD)	Bi et al. 2009

"–" = not given

Fig. 2 **A** TAS (Middlemost 1994) and **B** SiO_2 vs. A/CNK [A/CNK = molar ratio Al_2O_3/($CaO+Na_2O+K_2O$)] (Kemp and Hawkesworth 2003) diagrams for the Eocene–Oligocene fertile porphyries in the Sanjiang region, SW China. In A, the dashed line separating alkaline series from subalkaline series is from Irvine and Baragar (1971). Data for the Eocene–Oligocene fertile porphyries in the Sanjiang region, SW China and those formed in arc setting are from the Digital Appendix Tables A3, A6 and A8

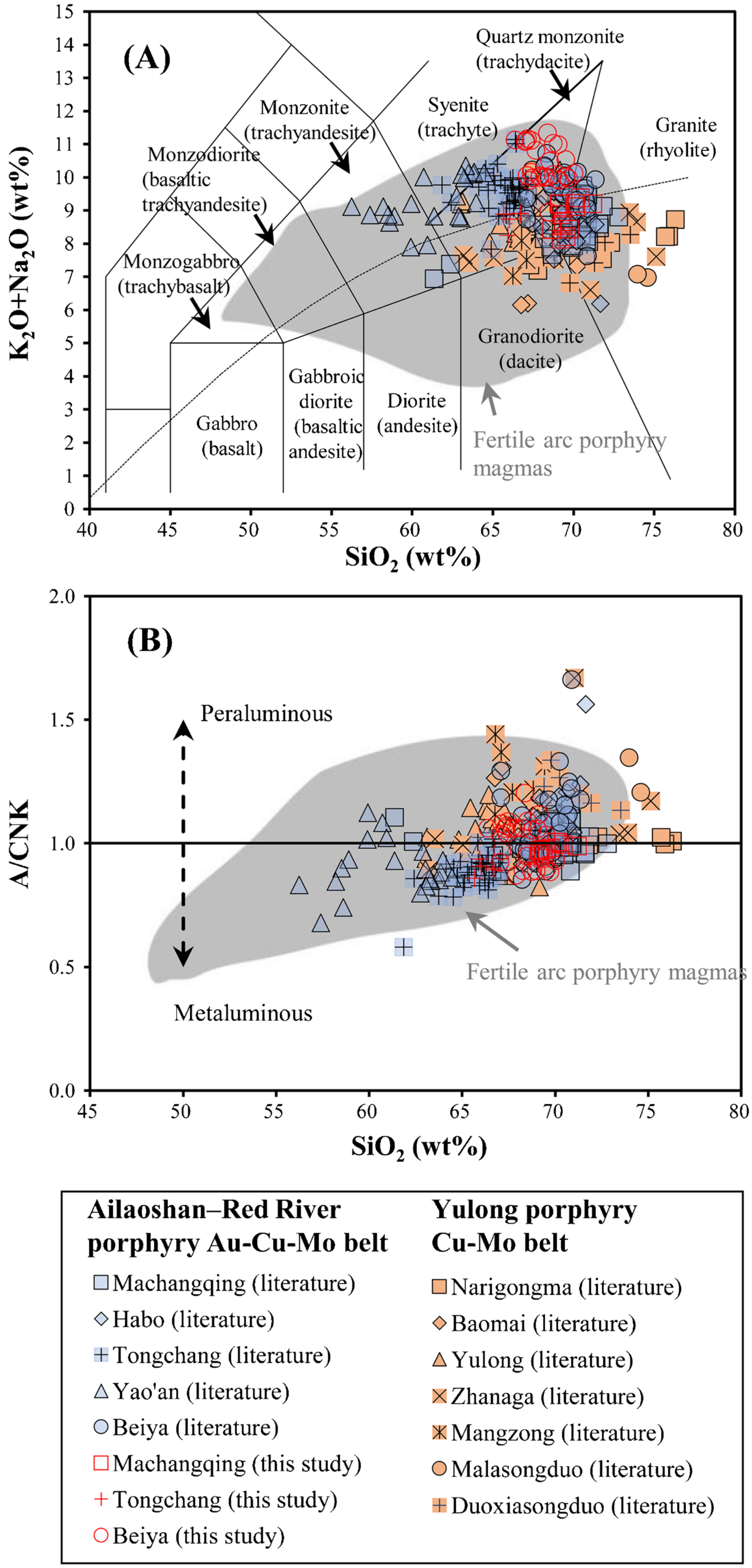

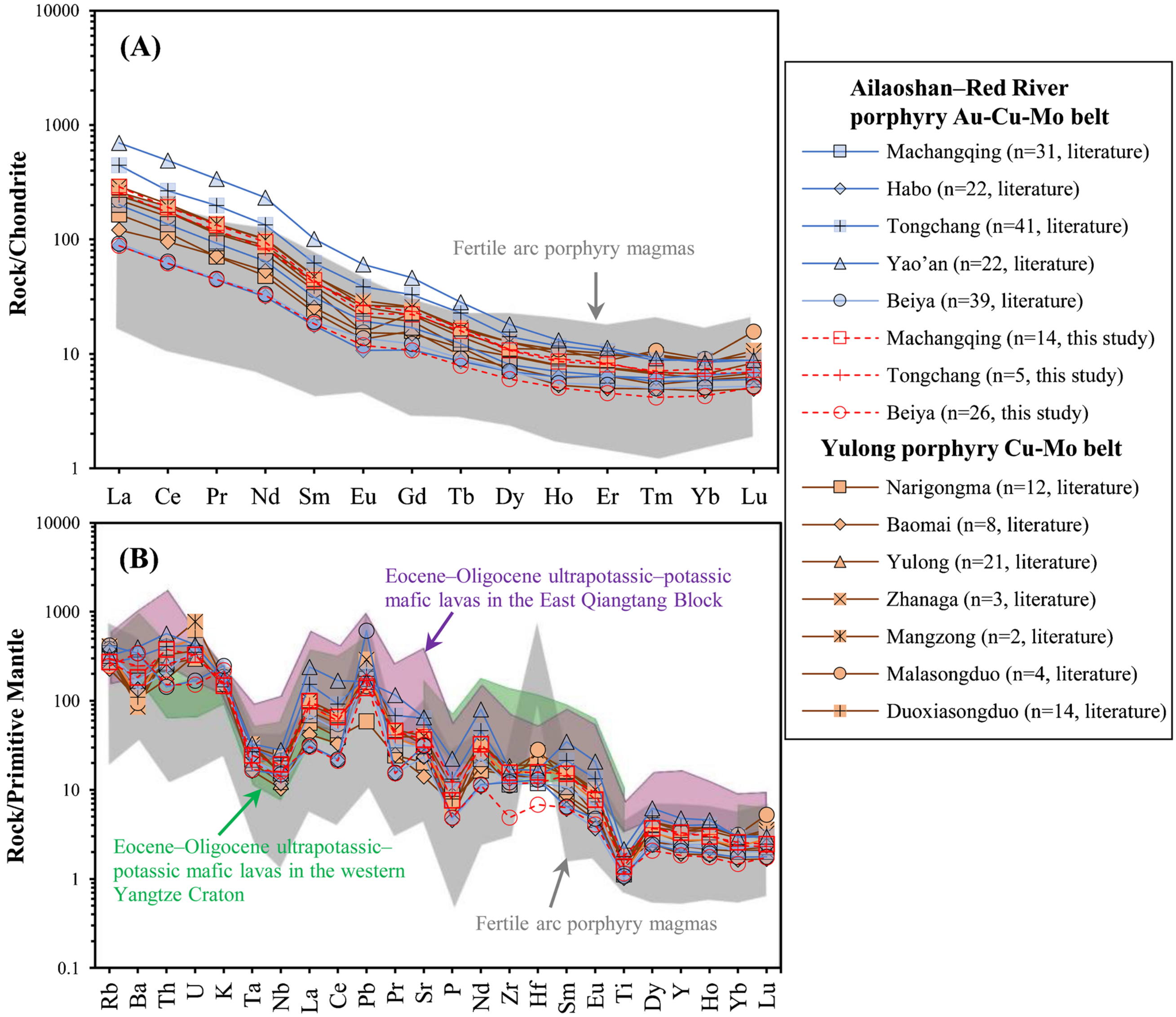

Fig. 3 Chondrite-normalized average whole-rock REE (**A**) and Primitive mantle-normalized average whole-rock trace-element (**B**) diagrams for the Eocene–Oligocene fertile porphyries in the Sanjiang region, SW China (normalization values from Sun and McDonough 1989). Data for the Eocene–Oligocene fertile porphyries in the Sanjiang region, SW China and those formed in arc setting are from the ESM Tables A3, A6 and A8. Data for Eocene–Oligocene potassic–ultrapotassic mafic lavas in western Yangtze Craton and East Qiangtang Block are from Guo et al. (2005, 2006)

are classified as quartz syenite, quartz monzonite, and granite, and plot across the fields of subalkaline and alkaline series (Fig. 2A). Generally, they are indistinguishable from the fertile porphyries in typical arc settings (Fig. 3), but the fertile arc porphyries tend to be more primitive overall, as indicated by lower SiO_2 contents and zircon $\delta^{18}O$ ratios, and more positive $\varepsilon_{Nd}(t)$ and zircon $\varepsilon_{Hf}(t)$ values (Figs. 2 and 4–6). Two groups can be formed based on their silica contents. The first group includes the Beiya, Machangqing, Habo, and Tongchang porphyries, all of which have felsic compositions, with SiO_2 contents from 59 to 73 wt% (average = 68 wt%). Whereas the other group includes the Yao'an porphyries with intermediate–felsic compositions, with SiO_2 contents from 56 to 67 wt% (average = 61 wt%). Three petrogenetic models have been proposed for the Ailaoshan–Red River porphyry belt: (1) magma derived from the SCLM that was modified by subduction in the Neoproterozoic (Zhang and Xie 1997; Bi et al. 2005; Lu et al. 2013a; Li et al. 2016; Mao et al. 2017), (2) magma derived from the overlying arc lower-crust formed in the Neoproterozoic (Lu et al. 2013a; Campbell et al. 2014; Deng et al. 2015; Hou et al. 2017; Xu et al. 2019), or (3) a hybrid formed by mixing between these two different types of magma (Zhu et al. 2013b; He et al. 2016; Zhou et al. 2019; Yang et al. 2020; Shen et al. 2021).

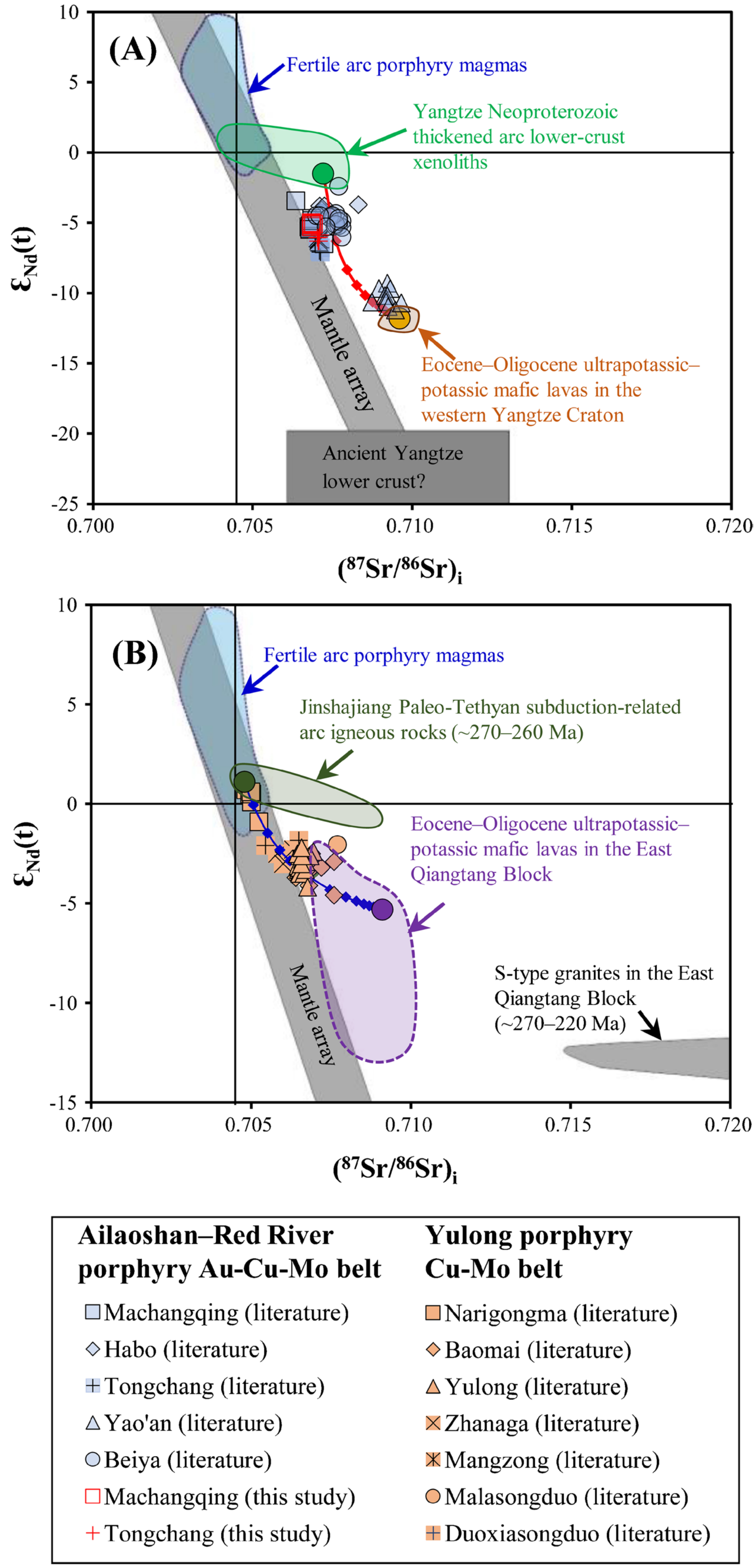

Fig. 4 $(^{87}Sr/^{86}Sr)_i$ vs. $\varepsilon_{Nd}(t)$ for the fertile porphyries (**A**) in the Ailaoshan–Red River Au-Cu-Mo and (**B**) Yulong porphyry Cu-Mo belts. Literature data plotted for comparison include fertile arc porphyry magmas (ESM Table A8), Yangtze Neoproterozoic thickened arc lower-crust xenoliths (Zhou 2018), ancient Yangtze lower crust (Jahn et al. 1999), Jinshajiang Paleo-Tethyan subduction-related arc igneous rocks (~ 270–260 Ma; Zi et al. 2012; Wu et al. 2013), S-type granites in the East Qiangtang Block (~ 270–220 Ma; Wu et al. 2013; Tao et al. 2014), and Eocene–Oligocene ultrapotassic–potassic mafic lavas in the western Yangtze Craton and East Qiangtang Block (Guo et al. 2005, 2006). The Sr–Nd isotopic data of the Yangtze Neoproterozoic thickened arc lower-crust xenoliths and ancient Yangtze lower crust in **A**, and those of the Jinshajiang Paleo-Tethyan subduction-related arc igneous rocks and S-type granites in the East Qiangtang Block in **B** have been calculated back to 35 Ma and 40 Ma, respectively. Mixing between enriched SCLM-derived ultrapotassic–potassic melts in the western Yangtze Craton and Yangtze Neoproterozoic thickened juvenile arc lower-crust-derived melts are used to model the formation of the fertile porphyries in the Ailaoshan–Red River belt; the Sr (ppm), Nd (ppm), $(^{87}Sr/^{86}Sr)_i$ and $\varepsilon_{Nd}(t)$ for endmembers used in mixing calculation: 1591, 65.2, 0.7096, and – 11.8 for pure enriched SCLM-derived potassic–ultrapotassic melts in western Yangtze Craton (Guo et al. 2005); 855, 8.25, 0.7072, and – 1.5 for Yangtze Neoproterozoic thickened juvenile arc lower-crust-derived melts (Zhou 2018). Data for the Eocene–Oligocene fertile porphyries in the Sanjiang region, SW China and those formed in arc setting are from the ESM Tables A3, A6 and A8. Mixing between enriched SCLM-derived ultrapotassic–potassic melts in the East Qiangtang Block and Jinshajiang Paleo-Tethyan subduction-related juvenile arc lower-crust-derived melts is used to model the formation of the fertile porphyries in the Yulong belt; the Sr (ppm), Nd (ppm), $(^{87}Sr/.^{86}Sr)_i$ and $\varepsilon_{Nd}(t)$ for end members used in mixing calculation: 2789, 102, 0.7091, and – 5.31 for enriched SCLM-derived potassic–ultrapotassic melts (median data; Guo et al. 2006); 427, 4.72, 0.7048, and 1.1 for Jinshajiang Paleo-Tethyan subduction-related juvenile arc lower-crust-derived melts (Zhu et al. 2022)

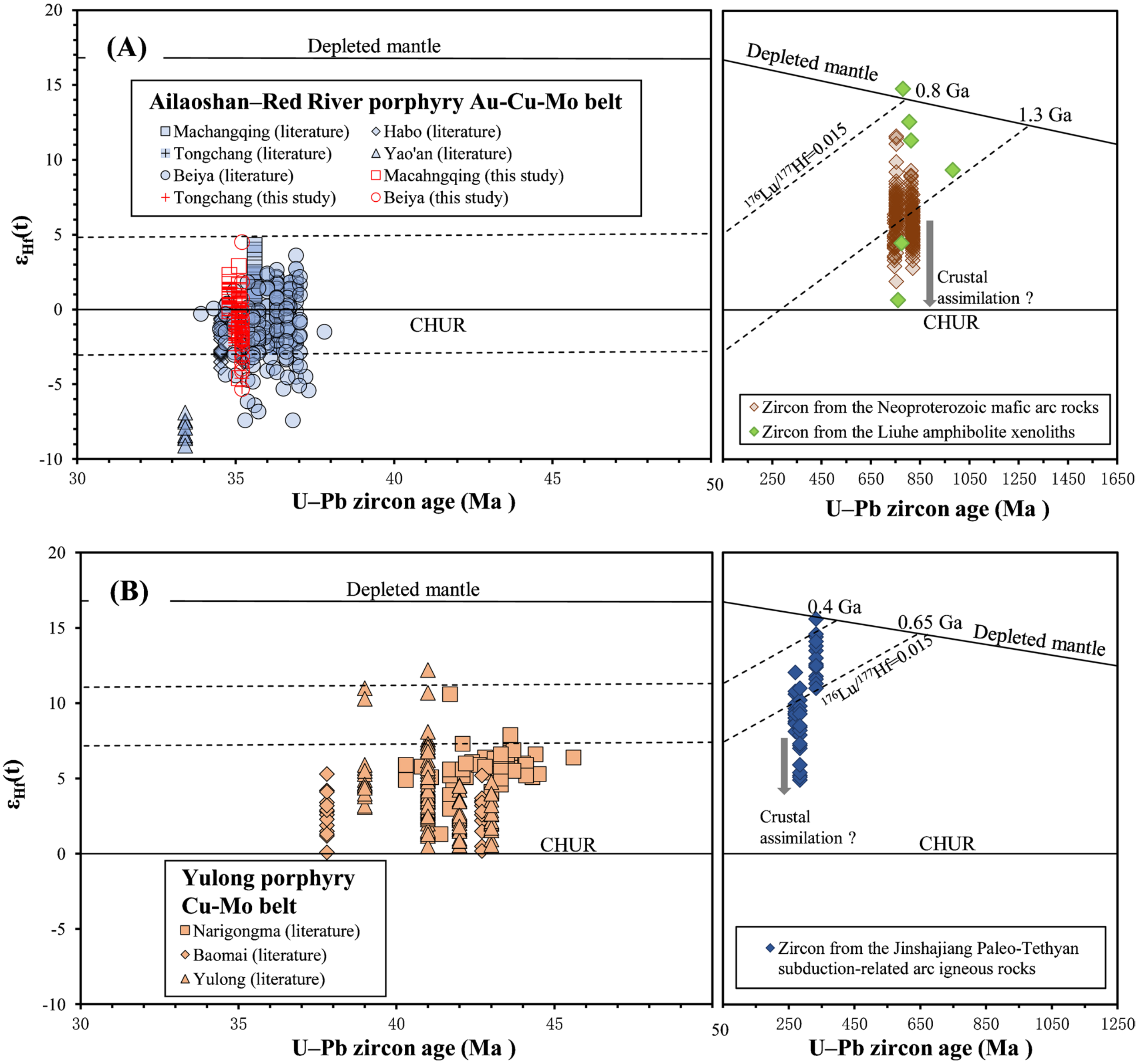

Fig. 5 Zircon U−Pb age vs. $\varepsilon_{Hf}(t)$ diagram for the fertile porphyries in **A** the Ailaoshan–Red River porphyry Au-Cu-Mo and **B** Yulong porphyry Cu-Mo belts. Data for the Eocene–Oligocene fertile porphyries in the Sanjiang region, SW China can be found in ESM Table A2 and A7. Zircon data for the Liuhe amphibolite enclaves and Neoproterozoic mafic arc rocks are from Hou et al. (2017) and Zhao et al. (2008), respectively. Zircon data for the Jinshajiang Paleo-Tethyan subduction-related arc igneous rocks are from Zi et al. (2012), Yan et al. (2018), and our unpublished data. Note zircon $\varepsilon_{Hf}(t)$ values of the Eocene–Oligocene fertile porphyries mostly plot below the isotope evolution trend of the Neoproterozoic (**A**) and *P–T* (**B**) arc rocks, respectively

The chemical compositions of the Eocene−Oligocene felsic fertile porphyries in the Ailaoshan–Red River belt are generally consistent with crust-derived magmas (Lu et al. 2013a, b; Zhu et al. 2013b; Deng et al. 2015; Hou et al. 2017; Xu et al. 2019). They have very high SiO_2 contents and very low MgO (mostly < 2 wt%), Cr (mostly < 40 ppm), and Ni (mostly < 20 ppm) contents (Figs. 8B-C; Table 2; ESM Tables A3 and A6), typical of igneous rocks formed from crust-derived melts. The Sr−Nd isotope compositions of these rocks are obviously inconsistent with those of the ancient (Archean to Paleoproterozoic) Yangtze cratonic lower crust (Fig. 4A; Jahn et al. 1999; Qiu et al. 2018; Zhao et al. 2020), but are close to those of a younger, Neoproterozoic source (Neoproterozoic mafic−ultramafic igneous rocks in the western margin of the Yangtze Craton: $\varepsilon_{Nd}(t = 35\ Ma) = -9.4$ to 8.0, average = 0.1, $(^{87}Sr/^{86}Sr)_i = 0.7030$ to 0.7087, average = 0.7051; Zhao et al. 2018b). The analyzed magmatic

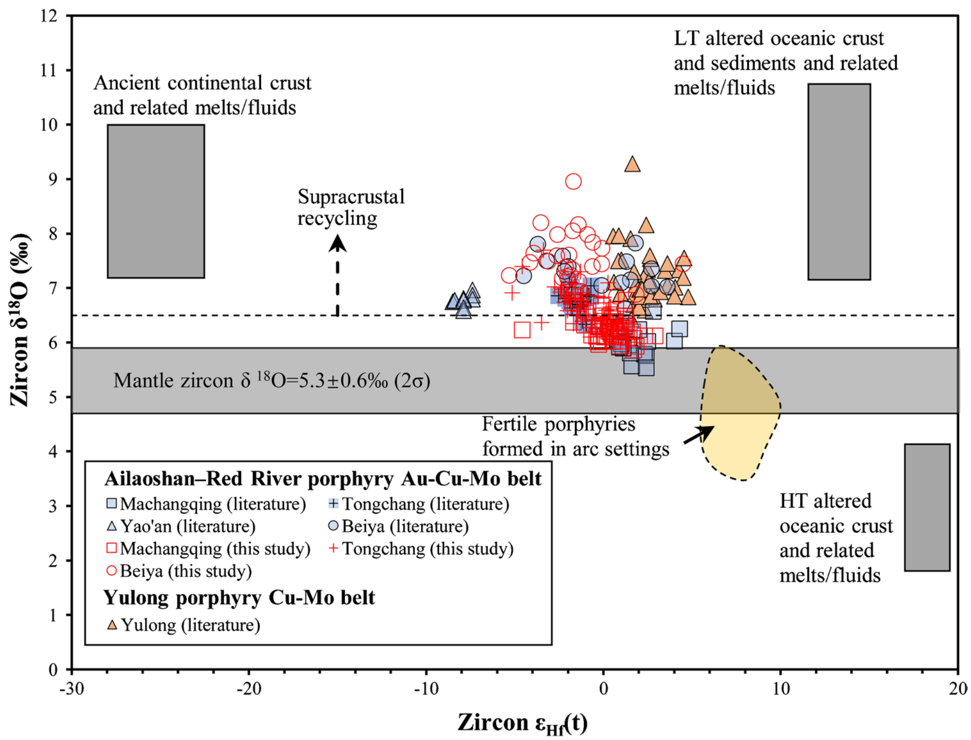

Fig. 6 Zircon $\varepsilon_{Hf}(t)$ vs. $\delta^{18}O$ diagrams for the Eocene–Oligocene fertile porphyries in the Sanjiang region, SW China. Data can be found in ESM Tables A2 and A7. Zircon $\delta^{18}O > 6.5‰$ indicates significant incorporation of supracrustal material. Data for mantle zircon, low-temperature (LT) altered oceanic crust and sediments and related melts/fluids, and high temperature (HT) altered oceanic crust and related melts/fluids are from Valley et al. (1998), Gregory and Taylor (1981), and Eiler (2001), respectively, and furthermore, data for ancient continental crust are from Zheng (1999) and Eiler (2001). Data for fertile porphyries formed in arc settings are from (Muñoz et al. 2012)

zircons from these felsic fertile porphyries mostly have Neoproterozoic Hf isotope model ages (Fig. 5A; ESM Tables A2 and A7), indicating a significant material contribution from the Neoproterozoic source as well (Hou et al. 2017). Neoproterozoic lower-crust amphibolite xenoliths entrained in some Eocene−Oligocene barren alkaline syenite plutons in the region may represent such a source, but the analyzed xenoliths show narrow ranges of $\varepsilon_{Nd}(t)$ from − 2.2 to + 1.1 and $(^{87}Sr/^{86}Sr)_i$ from 0.7041 to 0.7072 (Zhou et al. 2017b, 2019; Zhou 2018; Fig. 4A), which are slightly higher and lower, respectively, than the values of the felsic fertile porphyries in the Ailaoshan–Red River belt (Fig. 4A). We suggest the studied xenoliths were not the sole source of the felsic fertile porphyries in this belt. This interpretation is supported by the mismatch of the age-corrected zircon $\varepsilon_{Hf}(t)$ data between the studied felsic porphyries and the Neoproterozoic amphibolite xenoliths (Fig. 5A). The mismatch can be reconciled if a more isotopically enriched melt was also involved. Previous studies of the mafic–ultramafic end-members of the Eocene−Oligocene ultrapotassic−potassic suites in the region have suggested that the magma derived from the underlying metasomatized lithospheric mantle could be the required enriched end-member involved in the formation of the parental magma for the felsic fertile porphyries in the Ailaoshan–Red River belt (Fig. 4A; Guo et al. 2005; Huang et al. 2010). The positive correlation between whole-rock SiO_2 contents and $\varepsilon_{Nd}(t)$ values, coupled with the negative correlations of whole-rock SiO_2 contents versus Cr-Ni concentrations and $(^{87}Sr/^{86}Sr)_i$ ratios, suggest such a mixing model (Fig. 8A–D). Such inference is also in agreement with that made from helium and argon isotopes of the ore fluids exsolved from these fertile porphyries (Hu et al. 1998, 2004; Xu et al. 2014).

The origin of the Yao'an intermediate−felsic fertile porphyries in the Ailaoshan–Red River belt is not included in the above discussion because of different compositions. The Yao'an intermediate−felsic porphyries are more primitive than the other porphyries in this belt, with higher MgO (up to 4.35 wt%), Cr (mostly > 40 ppm, up to 149 ppm), and Ni (mostly > 20 ppm, up to 73.4 ppm; ESM Table A6; Fig. 8B, C). It is worth mentioning that Eocene−Oligocene ultrapotassic–potassic mafic igneous rocks are more abundant in the Yao'an and the nearby areas than elsewhere in the Ailaoshan–Red River belt (Guo et al. 2005; Huang et al. 2010; Campbell et al. 2014; Lu et al. 2015b). The ultrapotassic−potassic mafic igneous rocks and the intermediate–felsic fertile porphyries in the Yao'an deposit similarly have more enriched Sr−Nd isotope compositions than the fertile felsic porphyries as well as the Neoproterozoic amphibolite xenoliths in the region (Fig. 4A; Jahn et al. 1999; Lu et al. 2013a; Hou et al. 2017; Zhou et al. 2017b, 2019; Zhou 2018). The isotope compositions of the intermediate–felsic fertile porphyries and the ultrapotassic–potassic mafic igneous rocks in the Yao'an deposit are also very similar to the Eocene−Oligocene postcollisional lamprophyres in the western rim of the Yangtze Craton that are thought to be derived from the lithospheric mantle that was metasomatized by slab-derived

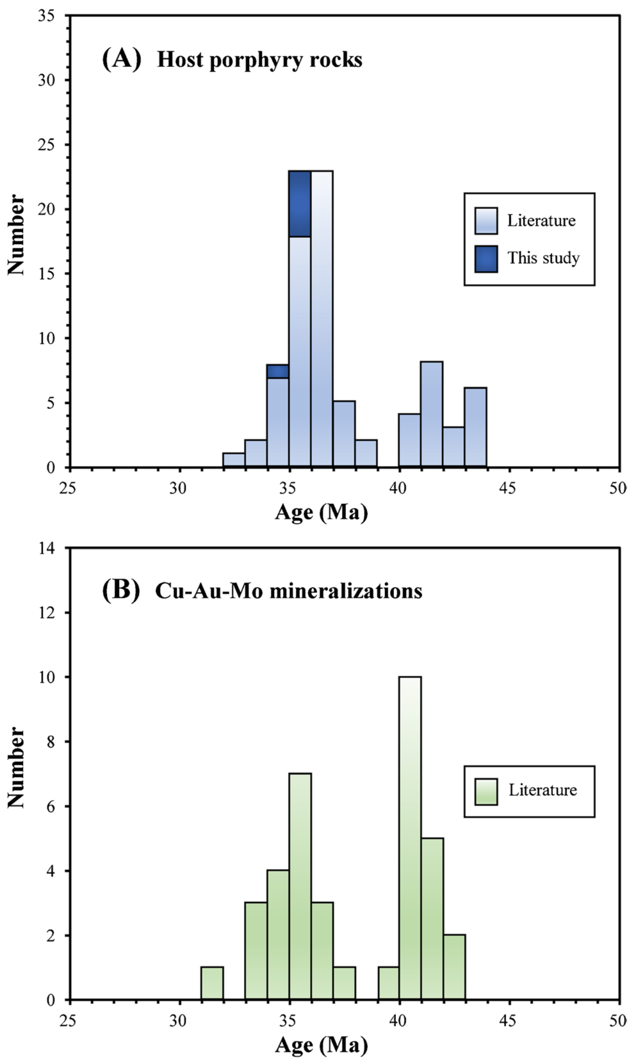

Fig. 7 Histograms of **A** zircon U−Pb and **B** molybdenite Re−Os and hydrothermal minerals U−Th−Pb ages for the Eocene–Oligocene fertile porphyries and associated Cu-Mo-Au deposits in the Sanjiang region, SW China, respectively. Original data can be found in ESM Table A5

fluids and/or subducted sediment-derived melts in the Neoproterozoic (Xu et al. 2001; Guo et al. 2005; Huang et al. 2010; Lu et al. 2013b, 2015b).

The above comparison supports the interpretation that the Yao'an intermediate–felsic fertile porphyries were mainly derived from an enriched mantle source. As shown in Fig. 8A–D, a weak positive correlation between whole-rock $\varepsilon_{Nd}(t)$ values and SiO_2 contents, and a weak negative correlation between whole-rock $\varepsilon_{Nd}(t)$ values and Cr-Ni concentrations indicate mixing of the mantle-derived mafic melt with minor amounts of crust-derived felsic melt for the Yao'an intermediate–felsic fertile porphyries. The latter was not possibly derived from the supracrustal contamination but from the overlying lower crust, as inferred from the negative correlation between whole-rock SiO_2 contents and $(^{87}Sr/^{86}Sr)_i$ ratios (Fig. 8D). As shown in Fig. 4A, the Yao'an fertile porphyries plot on a mixing line between the Neoproterozoic lower-crust xenoliths and the Eocene−Oligocene ultrapotassic–potassic mafic lavas. Mixing calculations suggest the addition of 10–30% crust-derived melt to the mantle-derived magma for Yao'an intermediate–felsic fertile porphyries. In contrast, parental magmas for the felsic fertile porphyry intrusions in this belt are estimated to contain > 80% of crust-derived melt. Such notable difference is consistent with observations from helium and argon isotopes of ore fluids exsolved from these fertile porphyries (Hu et al. 1998, 2004; Xu et al. 2014).

As discussed above, the fertile porphyry magmas can be explained by mixing between the magmas derived from a metasomatized lithospheric mantle and the overlying amphibole-bearing mafic crust that inherited arc signatures due to previous subduction (Guo et al. 2005; Huang et al. 2010; Lu et al. 2013a, 2015b; Hou et al. 2017; Zhou et al. 2019). For the Ailaoshan–Red River belt, the source modification by subduction took place in the Neoproterozoic, as indicated by abundant Neoproterozoic calc-alkaline igneous suites in the western rim of the Yangtze Craton (Zhou et al. 2002; Zhao et al. 2018b; Cawood et al. 2018). Zircon crystals from the metasomatized lithospheric mantle-derived, Eocene−Oligocene shoshonitic syenites (Lu et al. 2013b) and the crust-derived, Neoproterozoic granitoids in the region (Zhao et al. 2018b) all have elevated $\delta^{18}O$ values around 6.5‰, similar to those of the fertile porphyries in this belt (Fig. 6; ESM Tables A2 and A7). In summary, the formation of the hybrid magmas by mixing of mantle-derived melt and crust-derived melt can explain the observed elemental and isotopic compositions of the fertile porphyries in this belt.

Yulong porphyry Cu-Mo belt

We have discussed the petrogenesis of the fertile porphyries in the Yulong belt using published data. The Narigongma, Baomai, Yulong, Zhanaga, Mangzong, Malasongguo, and Duoxiasongduo mineralized intrusions all have high SiO_2 (63.0–76.3 wt%, average 68.5 wt%), K_2O (3.40–7.46 wt%, average 5.19 wt%) and Sr (124–1220 ppm, average 643 ppm) contents, and low Y (4.65–23.9 ppm, average 11.9 ppm) and Yb (0.440–1.93 ppm, average 1.08 ppm) contents (ESM Table A6; Fig. 2A, B). They are all characterized by significant light REE enrichments and pronounced negative Nb–Ta anomalies, indistinguishable from arc magmas (Fig. 3A, B). Two competing petrogenetic models have been proposed for the fertile porphyries in the Yulong belt: (1) low degrees of partial melting of the East Qiangtang SCLM that was enriched by the addition of slab-derived fluids and sediment-derived melts during the Paleo-Tethyan oceanic plate subduction (Hou et al. 2003; Jiang et al. 2006; Xu et al. 2016a); and (2) partial melting of the juvenile arc lower-crust formed

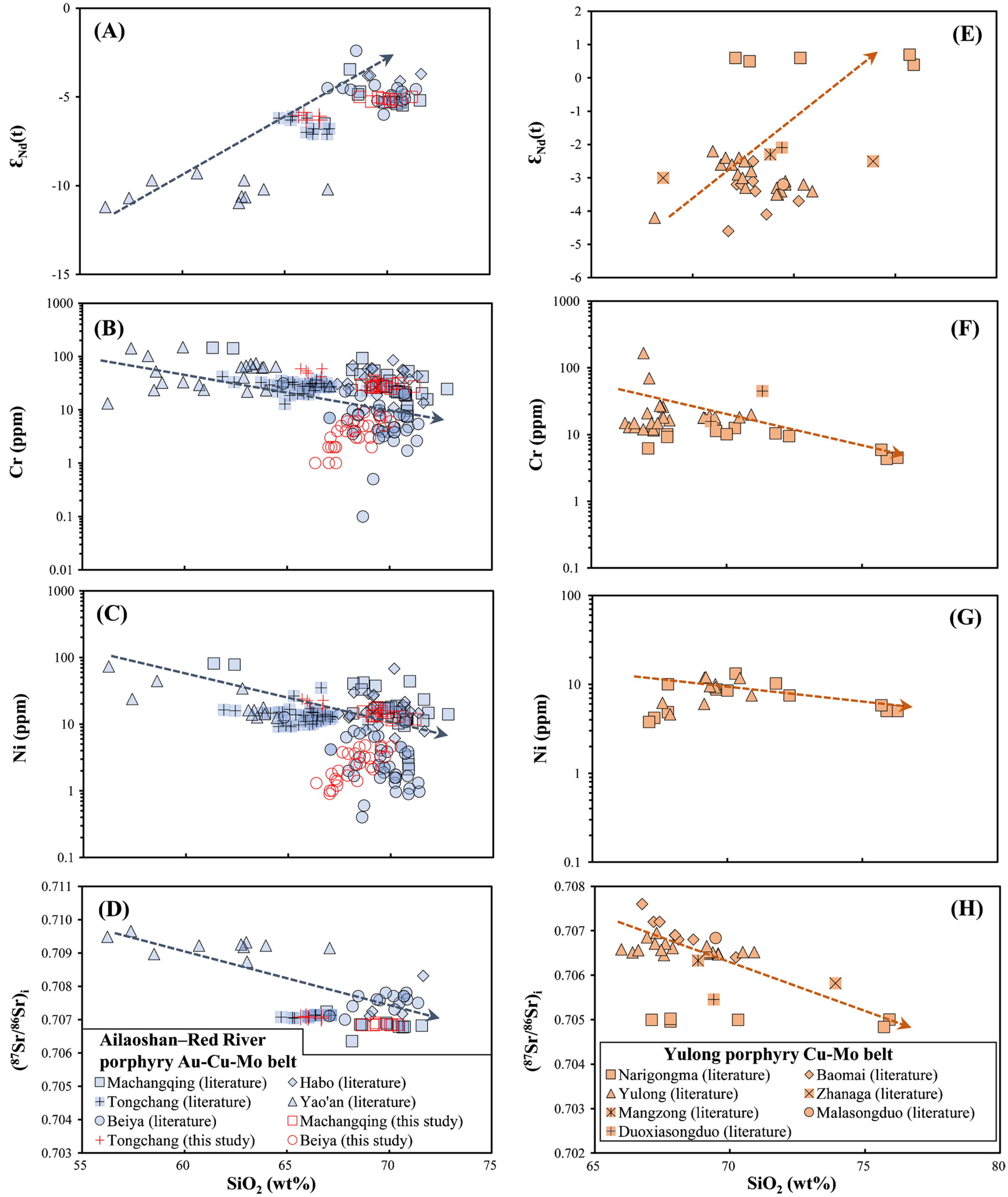

Fig. 8 SiO_2 vs. **A** $\varepsilon_{Nd}(t)$, **B** Cr, **C** Ni, and **D** $(^{87}Sr/^{86}Sr)_i$ for the fertile porphyries in the Ailaoshan–Red River porphyry Au-Cu-Mo belt, and SiO_2 vs. **E** $\varepsilon_{Nd}(t)$, **F** Cr, **G** Ni, and **H** $(^{87}Sr/.^{86}Sr)_i$ for the fertile porphyries in the Yulong porphyry Cu-Mo belt. Data can be found in ESM Tables A3 and A6

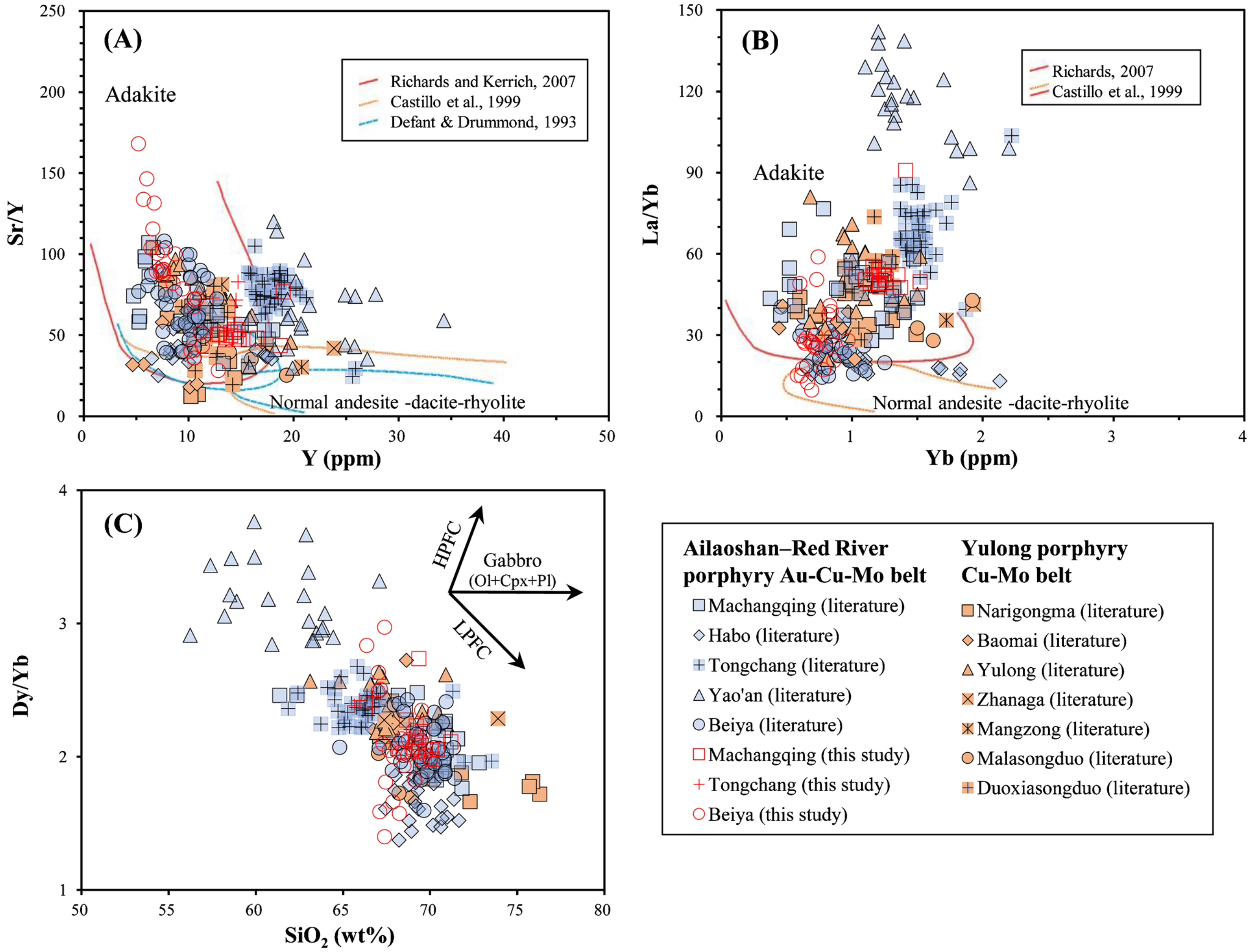

Fig. 9 **A** Y vs. Sr/Y, **B** Yb vs. La/Yb, and **C** SiO_2 vs. Dy/Yb diagrams for the fertile porphyries in the Ailaoshan–Red River porphyry Au-Cu-Mo and Yulong porphyry Cu-Mo belts. HPFC: high-pressure fractionation (involving garnet + clinopyroxene). LPFC: low-pressure fractionation (involving amphibole + plagioclase). Fractional crystallization trends in **C** are from Davidson et al. (2007) and Macpherson (2008). Data can be found in ESM Tables A3 and A6

during the subduction of the Paleo-Tethyan oceanic plate that took place from the Permian to Late Triassic (Li et al. 2012; Yang et al. 2014a; Huang et al. 2019a).

Experimental studies have shown that partial melting of a mantle source cannot produce large amounts of melts containing > 57.3 wt% SiO_2 (e.g., Baker et al. 1995; Jahn et al. 2001). More importantly, coeval ultrapotassic–potassic mafic lavas that originated from the metasomatized SCLM in the region, have higher incompatible element concentrations and more enriched Sr–Nd isotope compositions than the fertile porphyries (Figs. 3B and 4B; Turner et al. 1993, 1996; Deng 1998; Ding et al. 2003; Guo et al. 2006). Thus, it is unlikely that the fertile porphyries in the Yulong belt were direct partial melting products of the metasomatized SCLM or produced by extensive fractional crystallization of the metasomatized SCLM-derived mafic magmas in the region, implying that other sources and/or processes are required for the genesis of the fertile porphyries in the Yulong belt.

It is true that Permian–Triassic arc volcanic rocks are abundant in the region (Fig. 1B; Mo and Pan 2006; Yang et al. 2014b; Wang et al. 2018b; Zhao et al. 2018a). The arc volcanic rocks have significantly higher $\varepsilon_{Nd}(t)$ than the Eocene–Oligocene fertile porphyries except Narigongma in the region (Fig. 4B; Zi et al. 2012; Wu et al. 2013; Zhu et al. 2022). Our calculations show that the differences are mostly larger than the radiogenic production from Permian to Cenozoic. Such differences likely also exist between the arc cumulates (juvenile lower-crust) at depth (the suggested source of model-2) and the Eocene–Oligocene fertile porphyries except Narigongma. Similarly, the zircon $\varepsilon_{Hf}(t)$ values (0.1 to 12.2; ESM Table A7) of the Eocene–Oligocene fertile porphyries mostly plot below the isotope evolution

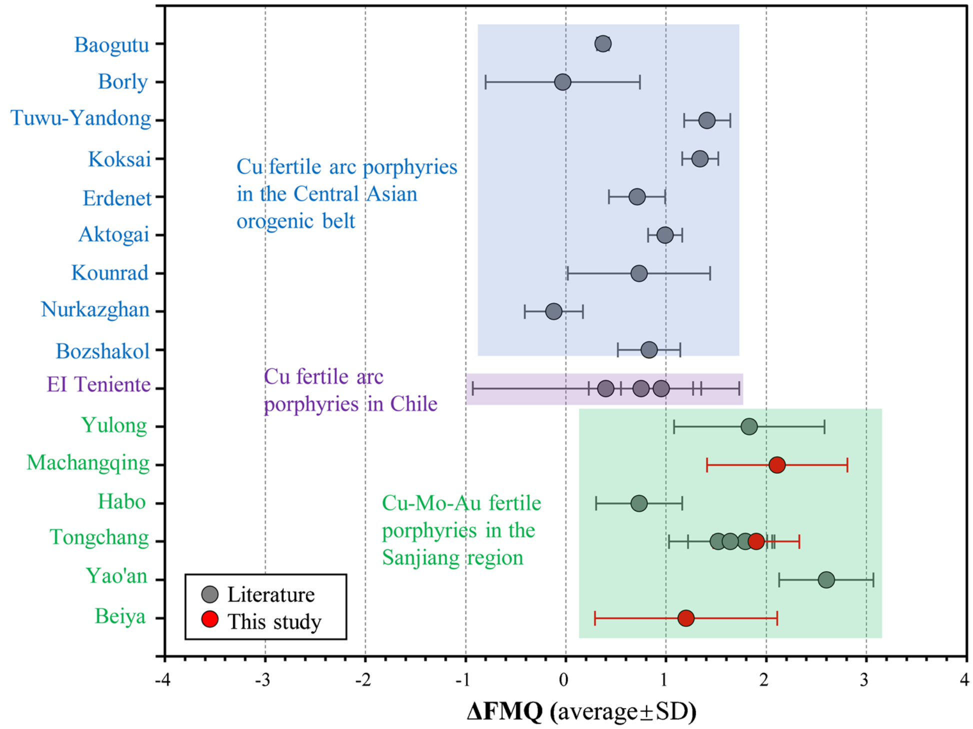

Fig. 10 Diagram of magmatic relative oxidation states (ΔFMQ) calculated from zircon compositions using the method of Loucks et al. (2020) for the Eocene–Oligocene fertile porphyries in the Sanjiang region, SW China. Cu fertile arc porphyries in Chile and the Central Asian orogenic belt are used for comparison. All the data and references can be found in Table 3 and ESM Tables A2 and A9

trend of arc rocks (Fig. 5B). Therefore, partial melting of the Permian–Triassic juvenile arc lower-crust in the region also cannot account for the genesis of the fertile porphyries in the Yulong belt alone.

Interestingly, the Eocene–Oligocene fertile porphyries in the Yulong belt have Sr−Nd isotope compositions between the Permian–Triassic arc rocks and Eocene–Oligocene metasomatized SCLM-derived ultrapotassic−potassic mafic rocks in the region (Fig. 4B). We therefore suggest that the parental magmas of the fertile porphyries in the Yulong belt most likely formed by mixing between the Permian–Triassic juvenile arc lower-crust-derived melts and metasomatized SCLM-derived melts. The composition of magma derived from the Permian–Triassic juvenile arc lower-crust may be approximately represented by the most evolved Permian–Triassic arc igneous rocks in the region, which are characterized by high $\varepsilon_{Nd}(t)$ values and SiO_2 contents, coupled by low Cr and Ni concentrations and $(^{87}Sr/^{86}Sr)_i$ ratios (Zi et al. 2012; Wu et al. 2013; Zhu et al. 2022). The composition of magma derived from a metasomatized SCLM source in the region may be represented by the Eocene–Oligocene ultrapotassic−potassic mafic rocks, which are characterized by low $\varepsilon_{Nd}(t)$ values and SiO_2 contents, coupled by high Cr-Ni contents and $(^{87}Sr/^{86}Sr)_i$ ratios (Fig. 4B; Turner et al. 1996; Guo et al. 2005, 2006; Campbell et al. 2014; Yang et al. 2014a, 2015). Mixing between these two types of magmas would generate a positive correlation between $\varepsilon_{Nd}(t)$ values and SiO_2 contents, coupled by a negative correlation between $\varepsilon_{Nd}(t)$ values and Cr-Ni concentrations as well as a negative correlation between SiO_2 contents and $(^{87}Sr/^{86}Sr)_i$ ratios. As expected, the fertile porphyries of the Yulong belt clearly show such correlations (Fig. 8E–H). The Sr−Nd isotope data for the Yulong fertile porphyries are also consistent with the mixing model (Fig. 4B). More specifically, the Narigongma porphyry intrusion formed mainly from magma derived from the Permian–Triassic juvenile arc lower-crust, with < 3% input from magma derived from the underlying metasomatized lithospheric mantle, whereas the other fertile porphyry intrusions in this belt formed from hybrid magma containing ~ 10% of mantle-derived melt and ~ 90% of juvenile arc lower-crust-derived melt. Such a crust−mantle mixing characteristic is well consistent with the inference from helium and argon isotopes of the ore fluids exsolved from the fertile porphyries in the Yulong belt (Hu et al. 2004).

Zircon oxygen isotope compositions of the fertile porphyries in the Yulong belt ($\delta^{18}O = 7.2 \pm 0.5‰$; ESM Table A7) are also consistent with the magma mixing model. The *P–T* arc juvenile lower-crust-derived magma, as represented by the Permian Jiyidu arc intrusions, is expected to have zircon $\delta^{18}O$ values of 6–6.8‰ (Zi et al. 2012), whereas the underlying metasomatized lithospheric mantle-derived melt is expected to have zircon $\delta^{18}O$ values of 6–7.5‰ (Campbell et al. 2014). Such elevated $\delta^{18}O$ values can be attributed to inheritance from the sources (Turner et al. 1993, 1996; Ding et al. 2003; Kemp et al. 2007). The zircon $\delta^{18}O$ values of these fertile porphyries (7.2 ± 0.5‰; Fig. 6; ESM Table A7) support hybrid parental magmas for these rocks.

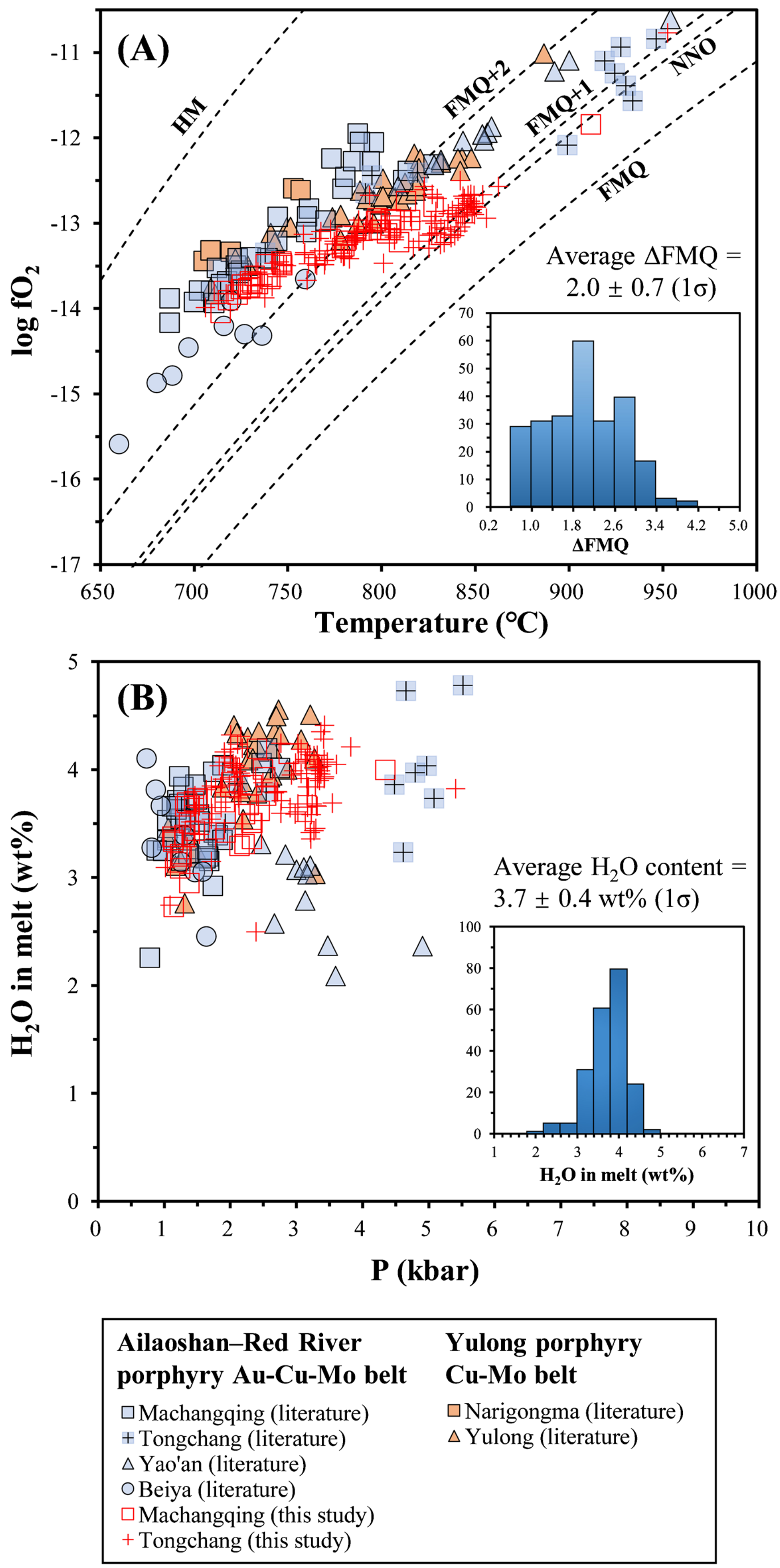

Fig. 11 Temperature vs. oxygen fugacity (in log fO_2) **A** and pressure vs. H_2O in melt **B** diagrams for the Eocene–Oligocene fertile porphyries in the Sanjiang region, SW China. They are calculated by amphibole compositions using the method of Ridolfi et al. (2010). Data can be found in the Table 4 and ESM Tables A4 and A10. FMQ (fayalite-magnetite-quartz oxygen buffer), FMQ + 1, FMQ + 2, and NNO (Ni-NiO oxygen buffer) are from O'Neill (1987), and O'Neill and Pownceby (1993). HM (magnetite-hematite oxygen buffer) is from Chou (1978)

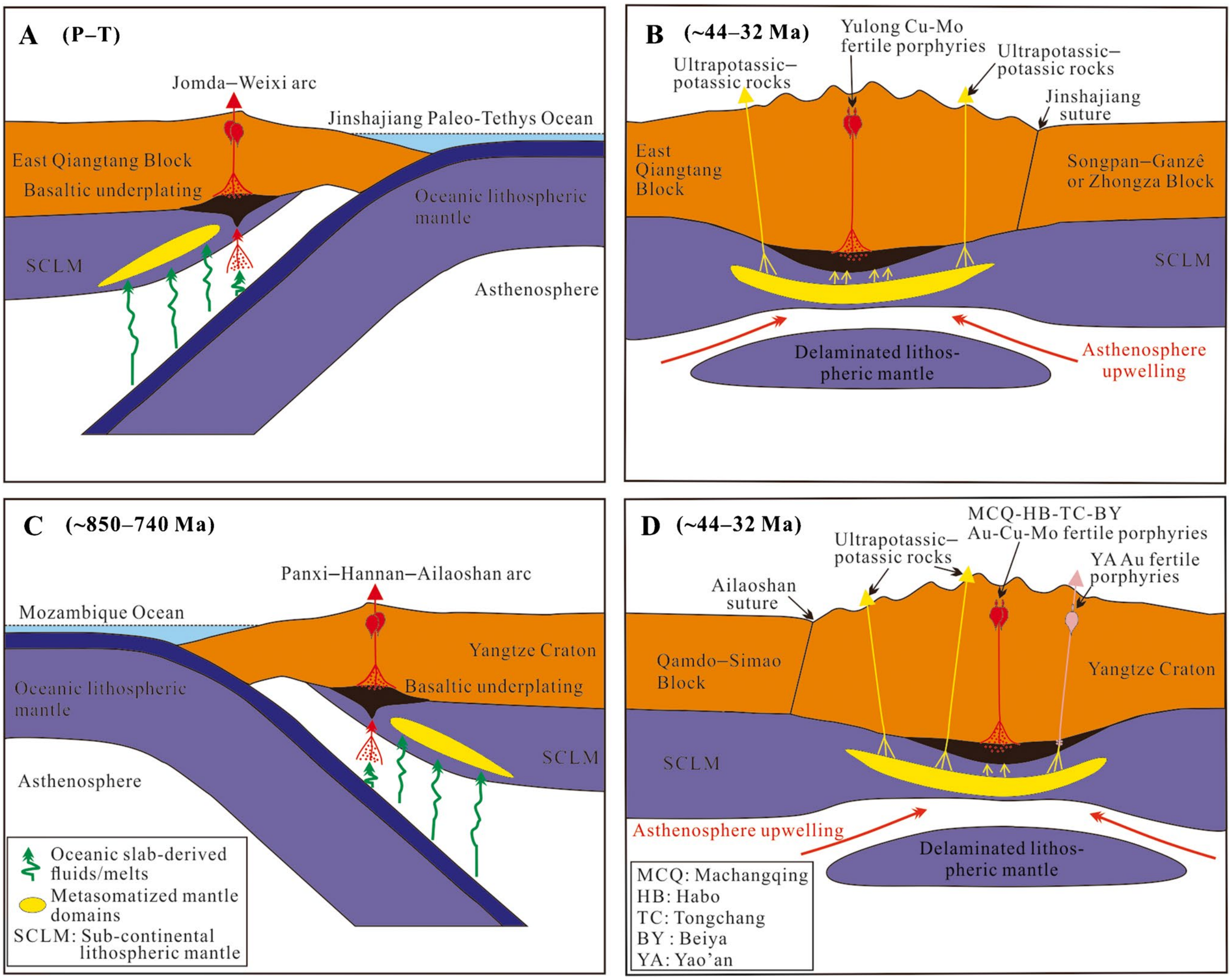

Fig. 12 Proposed genetic model to illustrate the formation of the fertile porphyries in **A**, **B** the Yulong porphyry Cu-Mo and **C**, **D** Ailaoshan–Red River porphyry Au-Cu-Mo belts (modified after Zhou et al. 2002; Richards 2009; Zi et al. 2012; Lu et al. 2013a: Xu et al. 2016b; Zhao et al. 2018b and Wang et al. 2022). **A** The Permian–Trassic (P–T) Jinshajiang Paleo-Tethyan ocean subduction triggered formation of arc magmas that underplated to form the juvenile mafic arc lower-crust and enriched SCLM; **B** after closure of the Jinshajiang Paleo-Tethyan ocean, due to triggers from the thinning of SCLM during the Eocene to Oligocene, mixing of melts from enriched SCLM and this juvenile mafic arc lower-crust generated the magmas that emplaced to form the fertile porphyries in the Yulong Cu-Mo belt; **C** the Neoproterozoic ocean subduction (~850–740 Ma) triggered formation of metasomatized SCLM domains and arc magmas that underplated to form the mafic juvenile lower-crust; and **D** after closure of the Jinshajiang–Ailaoshan Paleo-Tethyan ocean, due to triggers from the thinning of SCLM during the Eocene–Oligocene, mixing of melts from the metasomatized SCLM domains and this Neoproterozoic mafic juvenile lower-crust generated the magmas that emplaced to form the fertile porphyries in the Ailaoshan–Red River Au-Cu-Mo belt

Estimates of magmatic oxidation state and water contents for the Jinshajiang–Ailaoshan porphyry Cu-Au-Mo belt

In the previous studies, magmatic oxidation states of the fertile porphyries in the Jinshajiang–Ailaoshan porphyry Cu-Au-Mo belt have been estimated mostly based on the zircon oxybarometer (i.e., Ce^{4+}/Ce^{3+} ratio in zircon) of Ballard et al. (2002) (e.g., Liang et al. 2006; Xu et al. 2016a, 2019; Yang et al. 2017; Meng et al. 2018), with a few based on biotite Mössbauer Fe^{3+}–Fe^{2+}–Mg ternary compositions (e.g., Bi et al. 2009), the zircon oxybarometer of Trail et al. (2011, 2012) (e.g., Meng et al. 2018), and the amphibole oxybarometer of Ridolfi et al. (2010) (e.g., Huang et al. 2019a). The applicability of the zircon oxybarometers of Ballard et al. (2002) and Trail et al. (2011, 2012) has many limitations, which largely depends on the accurate estimation of parental melt compositions for zircon, accurate measurement of zircon LREE compositions, and the fitness of the lattice strain model (Zou et al. 2019). Biotites are easily altered, so the Mössbauer Fe^{3+}–Fe^{2+}–Mg ternary compositions could be affected if the selected biotite separates were altered. The amphibole oxybarometer of Ridolfi et al. (2010) recently has been widely used in many studies focusing on other regions, and is thought to well reflect magmatic oxidation states (e.g., Cao et al. 2018; Zhu et al. 2018), but this method was only used in the Yulong deposit in the Sanjiang region (e.g., Huang et al. 2019a).

A new zircon oxybarometer has been recently proposed by Loucks et al. (2020). This method is based on the U, Ti, and Ce contents in zircon, and the calculated magmatic oxygen fugacities using this method are consistent with those calculated from the amphibole oxybarometer of Ridolfi et al. (2010) (Loucks et al. 2020). In this study, the oxybarometers of Loucks et al. (2020) and Ridolfi et al. (2010) are used to estimate the magmatic oxidation states based on the newly and previously-obtained data for zircon and amphibole compositions. Based on the method of Loucks et al. (2020) and newly-obtained data for zircon compositions, the estimated average ΔFMQ values for the Machangqing, Tongchang, and Beiya porphyry rocks are 2.1 ± 0.7, 1.9 ± 0.4 and 1.2 ± 0.9, respectively (Table 3; ESM Table A2), which are roughly similar to the recalculated results using published zircon compositional data for the Yulong, Habo, Tongchang and Yao'an deposits in the Jinshajiang–Ailaoshan porphyry Cu-Au-Mo belt (Fig. 10; Table 3; ESM Tables A2 and A9). These data are also roughly consistent with those of arc fertile porphyries worldwide (Fig. 10). Similarly, based on the method of Ridolfi et al. (2010) and compositions of amphibole phenocrysts, the Machangqing and Tongchang porphyry rocks show positive ΔFMQ values of 2.1 ± 0.6 and 1.6 ± 0.6, respectively (Table 4; ESM Table A4), similar to the published and recalculated results for Narigongma, Yulong, Machangiqng, Tongchang, Beiya, and Yao'an deposits in the Jinshajiang–Ailaoshan porphyry Cu-Au-Mo belt (Fig. 11; Table 4; ESM Table A10). In summary, the results from zircon and amphibole geochemistry combined indicate that the fertile porphyries in the Jinshajiang–Ailaoshan porphyry Cu-Au-Mo belt are all relatively oxidized in this region.

There are multiple lines of evidence for high H_2O contents in the parental magmas of fertile porphyries in the Jinshajiang–Ailaoshan porphyry Cu-Au-Mo belt. These include abundant amphibole and biotite phenocrysts in the rocks (Table 1; ESM Fig. A3; ESM Table A1). Such characteristics are commonly used as evidence for H_2O-rich parental magma (> 4 wt%; Burnham 1979; Rutherford and Devine 1988; Richards 2011a; Wang et al. 2014a; Zhu et al. 2018). The flat to listric-shaped chondrite-normalized REE patterns (Fig. 3A), high Sr/Y and La/Yb ratios, and decreasing Dy/Yb ratios with increasing SiO_2 contents (Fig. 9) of the fertile porphyries are consistent with fractional crystallization of amphibole from the parental magma (Richards and Kerrich 2007; Richards et al. 2012). The minor to negligible Eu anomalies of these rocks (Fig. 3A; ESM Tables A3 and A6) indicate that plagioclase is not a dominant phase in the early crystallizing assemblage. At deep crustal levels, hydrous magma (> 4 wt% H_2O) favors amphibole but suppresses plagioclase crystallization (Richards and Kerrich 2007; Richards 2011a; Chiaradia et al. 2012). Thus, it is reasonable to conclude that the parental magmas for the above fertile porphyries are H_2O-rich, which is also supported by the estimated H_2O contents using amphibole compositions (average = 3.7 ± 0.4 wt% H_2O; Fig. 11B; ESM Tables A4 and A10). All the available data for fertile porphyries in the Jinshajiang–Ailaoshan belt show a positive correlation between the estimated H_2O content with crystallization pressure (Fig. 11B), implying that the parental magmas were all saturated with H_2O during magma emplacement at various depths (Wang et al. 2014b; Chelle-Michou and Chiaradia 2017; Zhu et al. 2018). Based on such empirical relation and estimated crystallization pressures of ~ 1.6 kbars, the H_2O contents in the parental magmas for the fertile porphyries in the Jinshajiang–Ailaoshan belt before degassing are estimated to be > 4 wt% (ESM Tables A4 andA10; Fig. 11B), similar to the values for fertile arc porphyry magmas worldwide (Richards 2015a).

Causes of oxidized-hydrous fertile porphyry magmas in postcollisional setting and implications for ore formation

Arc magmas worldwide are known to be H_2O-rich (mostly > 4 wt% H_2O; Wallace 2005; Plank et al. 2013) and relatively oxidized (ΔFMQ = 0.5 to 2; Kelly and Cottrell 2012; Richards 2015a). Fertile arc porphyry magmas, such as those in Chile (Ballard et al. 2002; Muñoz et al. 2012), British Columbia of Canada (Red Chris; Zhu et al. 2018), Mongolia (Oyu Tolgoi; Wainwright et al. 2011), Philippines (Black Mountain; Cao et al. 2018), Central Asian Orogenic belt (Shen et al. 2015), and Tibet (Xiongcun; Wang et al. 2017; Xie et al. 2018) of China are also relatively oxidized (Fig. 10) and H_2O-rich. It is widely accepted that these features are due to the involvement of slab-derived fluids and/or subducted sediment-derived melts, which are significantly more oxidized than the normal mantle, during magma generation in the mantle wedge beneath a subduction zone (Arculus 1994; Richards 2003; Kelley and Cottrell 2012; Evans and Tomkins 2011). Postcollisional porphyry magmas such as the fertile porphyry magmas in the Jinshajiang–Ailaoshan belt are also hydrous and relatively oxidized, but cannot be explained using the arc model above. Therefore, we have deciphered the causes of such oxidized-hydrous porphyry magmas in the Jinshajiang–Ailaoshan belt by investigating major controlling factors such as magma processes and source.

The effect of differentiation processes in the crust

Many petrological processes such as crustal assimilation, fractional crystallization, and degassing can alter the magma oxidation state and H_2O content (Chiaradia et al. 2009; Kelley and Cottrell 2012; Brounce et al. 2014; Grocke et al. 2016; Tang et al. 2018; Li et al. 2020). In the case of the ore-forming porphyries in the Jinshajiang–Ailaoshan belt, supracrustal contamination is negligible, as indicated by the negative correlations between whole-rock SiO_2 contents and $(^{87}Sr/^{86}Sr)_i$ ratios (Fig. 8D, H). Fractional crystallization of Fe–Mg silicate minerals (e.g., olivine and clinopyroxene) will decrease Fe^{2+} and increase Fe^{3+} in the fractionated magma, thereby making the magma more oxidized (Cottrell and Kelley 2011; Li et al. 2020). However, for the porphyry rocks in this study, they are mostly felsic in composition without clear trend for olivine and clinopyroxene fractionation (Fig. 9C). Likewise, fractionation of garnet would remove Fe^{2+} into lattice sites, leading to enrichment of the melt in Fe^{3+} (Tang et al. 2018), but there is no evidence for garnet separation during the formation of the studied porphyries (Fig. 9C). There is no clear positive correlation between whole-rock Rb/Sr ratios and ΔFMQ values, suggesting fractionation has not affected the fO_2 conditions of porphyry magmas (Li et al. 2020). Magma degassing of CO_2, H_2, Cl, and SO_2 may or may not make the magma more oxidized (Bell and Simon 2011; Kelley and Cortrell 2012; Brounce et al. 2017). We have not found any clear evidence to suggest that the relatively oxidized nature of the parental magmas for the fertile porphyries in the Jinshajiang–Ailaoshan belt resulted from magma differentiation.

Role of subduction-modified SCLM

As discussed above, the parental magmas for the fertile porphyries in the Jinshajiang–Ailaoshan belt were most likely formed by mixing between magmas derived from a subduction-modified SCLM source and from the overlying juvenile arc lower-crust. It is widely accepted that the magmas derived from such a mantle source could be as oxidized as arc magmas, because in both cases oxidized slab-derived fluids and subducted sediment-derived melts were involved, albeit at different times. The juvenile lower-crust-derived magma could be also oxidized and hydrous by inheritance (e.g., Richards 2009; Li et al. 2012; Hou et al. 2013, 2015a, 2017). However, sulfide inclusions are common in the lower crustal xenoliths entrained in the coeval barren alkaline syenite and granite plutons in the Ailaoshan–Red River belt (Hou et al. 2017; Zhou et al. 2017b), implying that the oxidation states of such a source would be less than FMQ + 1.5 (Jugo et al. 2005; Jugo 2009), which is within the range of the estimated oxidation states for the fertile porphyries but significantly lower than the higher end of the range. Many researchers have argued that it is difficult to generate a partial melt from this type of juvenile lower-crust to be as H_2O rich as the magmas of the fertile porphyries in the Jinshajiang–Ailaoshan belt (Lu et al. 2015a; Yang et al. 2014a, 2015; He et al. 2016; Zhou et al. 2019).

If the parental magmas for the fertile porphyries in the Jinshajiang–Ailaoshan belt formed by magma mixing between a juvenile lower-crust-derived melt and a mantle-derived melt, as we argue, then the mantle-derived end-member would be more oxidized and more H_2O rich than the crust-derived end-member. In our model, we propose that the mantle was previously metasomatized by slab-derived fluids and sediment-derived melts. Since these metasomatizing agents could be highly oxidized, such a source could become highly oxidized as well as hydrous, as was suggested for the Tibetan mantle (Li et al. 2020). As a result, the partial melts derived from such a source could also be highly oxidized and hydrous. Using the ilmenite-magnetite oxybarometer, the oxidation states of the Cenozoic, mantle-derived ultrapotassic–potassic mafic rocks that occur near the Yulong fertile porphyry belt are estimated to be at ΔFMQ > 1 (Turner et al. 1996). Based on the olivine oxybarometer, the oxidation states of the Cenozoic mantle-derived high Mg-number shoshonitic rocks that occur near the Ailaoshan–Red River fertile porphyry belt, are estimated to be at ΔFMQ between 0.5 and 5.0, with an average of 2.0 (Huang et al. 2010). Fractionation could influence magmatic oxidation state (Li et al. 2020), whereas it could be excluded because the least evolved igneous rocks were selected for fO_2 estimations (Turner et al. 1996; Huang et al. 2010). In both cases, the ultrapotassic–potassic mafic rocks and the fertile porphyries share a common mantle end-member that was metasomatized previously by slab-derived fluids and subducted sediment-derived melts.

Low-degree partial melting of a hydrated SCLM could produce an ultrapotassic–potassic mafic melt with H_2O content higher than usual because the solubility of H_2O in such a melt is much higher than in subalkaline magma at the same pressure (Behrens et al. 2009). The occurrence of abundant phlogopite in this type of Cenozoic rocks in southern Tibet including the Sanjiang region indicates the existence of such mantle-derived hydrous magma in the region (Turner et al. 1996). Such hydrous magma could release water during magma ascent at various depths, depending on the initial contents (Jiang et al. 2006; Lu et al. 2013b; Yang et al. 2014a, 2015; Hou et al. 2017; Zhou et al. 2017b). If this happened in the deep crust, the released water could be added to the lower crust, causing it to melt. Using the Ti-in-zircon thermometer, the parental magma of the fertile porphyries in this region are estimated to be < 750℃ with few exceptions (Table 3; ESM Tables A2 and A9), supporting the water-fluxed partial melting of the lower crust (Weinberg and Hasalová 2015; Collins et al. 2016). In addition, ponding of the mantle-derived magma in the lower crust could provide conductive heating to the overlying crust. This, together with the addition of the water released from the mantle-derived magma, could cause larger degrees of partial melting in the crust. Mixing between the mantle-derived and the crustal melts could occur in some places at this level.

Tectonic–magmatic models

The fertile porphyries of the Ailaoshan–Red River belt in the western rim of the Yangtze Craton and those of the Yulong belt in the East Qiangtang Block have similar ages (44–32 Ma) as well as similar chemical and isotopic compositions, consistent with magmas formed from mixing between enriched lithospheric mantle-derived and mafic arc crust-derived melts. The enrichments in the mantle sources are due to previous metasomatism by slab-derived fluids and/or subducted sediment-derived melts. In the case of the Ailaoshan–Red River belt, this process took place in the Neoproterozoic, related to the subduction of the oceanic plate beneath the western rim of the Yangtze Craton (see summary in Cawood et al. 2018; ESM Figs. A1A-B). In the case of the Yulong belt, this process took place in the Permian–Triassic, related to the subduction of the Paleo-Tethyan oceanic plate beneath the East Qiangtang Block (see summary in Deng et al. 2014a; ESM Fig. A1E). In both cases, a mafic lower crust was produced by accumulation of mafic minerals from the subduction-related basaltic magma. Partial melting of the metasomatized SCLM and the overlying mafic lower crust at both locations between 44 and 32 Ma produced a mafic end-member and a felsic end-member, respectively. At least two different models of partial melting have been proposed, including lithospheric thinning by convective removal of thickened lower lithosphere (Turner et al. 1993, 1996; Yakovlev et al. 2019) and continental subduction (Ding et al. 2003; Spurlin et al. 2005; Wang et al. 2005). However, combined geophysical observations and geochemistry of the Eocene potassic mafic lavas in the western Yangtze Craton suggest that the lithospheric thinning of the western Yangtze Craton during the Cenozoic continental collision was caused by delamination of thickened lower lithosphere due to compositional and thermal densification instead of hydration- or oxidation-induced rheological weakening (Wang et al. 2022). Thus, the lithospheric thinning model by lithospheric delamination is preferred and discussed below.

Protracted subduction of the Neo-Tethyan oceanic plate beneath Tibet from Late Tertiary to Early Cenozoic dramatically increased the lithosphere thickness in the southern Tibet and Sanjiang region including the East Qiangtang Block and the western rim of the Yangtze Craton (Turner et al. 1996; Chung et al. 2005; Lu et al. 2012, 2013b, 2015b). The thickened lithosphere was gravitationally unstable during the subsequent continental collision, inducing lithospheric delamination and coupled upwelling of the underlying asthenosphere, which then caused melting of the overlying lithosphere (Richards 2009; Lu et al. 2013b, 2015b; Wang et al. 2022). As described above, the lithosphere of the Yulong and Ailaoshan–Red River porphyry belts was metasomatized by slab-derived fluids and subducted sediment-derived melts in the Permian–Triassic and in the Neoproterozoic, respectively. With this in mind, we have proposed a two-stage model for formation of the fertile porphyries in these two belts (Fig. 12). In the case of the Yulong fertile porphyry belt in the East Qiangtang Block, arc magma formed by flux melting from Permian to Triassic was emplaced at depth to form a juvenile mafic lower crust; addition of slab-derived fluids and subducted sediment-derived melt to the mantle wedge resulted in metasomatism and enriched mantle (Fig. 12A). In the case of the Ailaoshan–Red River porphyry belt in the western rim of Yangtze Craton, these processes took place much earlier in the Neoproterozoic (Fig. 12C). The preservation of such metasomatized lithospheric mantle is important, which depends on whether it was modified by subsequent geologic events (e.g., oceanic subduction) and the degree of modification by these geologic events. It is true that, the Neoproterozoic metasomatized lithospheric mantle beneath the western Yangtze Craton and the Permian–Triassic metasomatized lithospheric mantle beneath the East Qiangtang Block were well preserved until the Cenozoic (Guo et al. 2006; Lu et al. 2015b). From the Eocene to Oligocene, delamination of the root of the lithosphere coupled with asthenosphere upwelling triggered partial melting in the lithospheric mantle, producing an oxidized and hydrous fertile mafic melt. Underplating of such magma in the overlying juvenile lower-crust induced partial melting of the lower crust. Mixing between the two melts at different proportions formed fertile porphyry magmas with variable compositions (Fig. 12B, D).

Although they are contemporaneous, the Cenozoic porphyry deposits in the Ailaoshan–Red River and Yulong belts in the Sanjiang region have different compositions. The former are more enriched in Au (e.g., Beiya and Yao'an) with only a few small Cu-Mo deposits (Bi et al. 2004, 2005, 2009; Xu et al. 2012, 2016a, 2019; Lu et al. 2013a; Deng et al. 2015; He et al. 2016; Hou et al. 2017; Zhou et al. 2017a) whereas the latter are generally more enriched in Cu and Mo (e.g., Yulong and Narigongma; Hou et al. 2003, 2007a, 2007b; Jiang et al. 2006; Liang et al. 2006; Li et al. 2012; Yang et al. 2014a; Chang et al. 2017). Globally, such variations have been attributed to differences in magma sources, crustal processes, depths of magma emplacement, redox conditions, and fluid evolution (e.g., Heinrich et al. 1999; Richards 2009; Murakami et al. 2010; Zajacz et al. 2012, 2017; Griffin et al. 2013; Lu et al. 2013b; Yang et al. 2014a; Tattitch and Blundy 2017; Chiaradia 2021). In the case of the Cenozoic porphyry deposits in the Jinshajiang–Ailaoshan belt, the metal variations are most likely related to source variations, because it has been suggested that the magmas derived from metasomatized SCLM tend to be more enriched in Au (e.g., McInnes et al. 1999; Griffin et al. 2013; Wilkinson 2013) and those derived from the lower crust tend to be more enriched in Mo (Mao et al. 1999; Richards 2011b; Sun et al. 2015; Hou and Wang 2018). More interestingly, helium and argon isotopes suggest that, the ore fluids of the Cenozoic porphyry deposits (e.g., Beiya and Yao'an) in the Ailaoshan–Red Rive belt have higher proportions of a mantle contribution than those of the Yulong belt (Hu et al. 1998, 2004; Xu et al. 2014). This may, to some extent, explain the compositional variations of the fertile porphyries in the Sanjiang region. Higher Au contents in the porphyry deposits of the Ailanshan–Red River belt in the western rim of the Yangtze Craton are probably due to a high proportion of mantle-derived melts in their parental magmas; higher Mo contents in the porphyry deposits of the Yulong belt in the East Qiangtang Block are possibly due to a dominantly juvenile lower crust-derived melt in the parental magmas for these deposits.

Conclusions

Zircon U−Pb ages, Hf−O isotopes, zircon and amphibole chemical compositions, and whole-rock chemical and Sr−Nd isotope compositions were analyzed for the fertile porphyries of the Machangqing, Tongchang, and Beiya deposits in the Ailaoshan–Red River porphyry Au-Cu-Mo belt (southern part of the Sanjiang region), SW China. Zircon U−Pb dating suggests the ore-forming porphyries emplaced at 35.4−34.8 Ma. The whole-rock chemical compositions indicate that the porphyry samples are all felsic (SiO_2 = 65.7–71.2 wt%) and metaluminus to weakly peraluminus [molar $Al_2O_3/(CaO + Na_2O + K_2O)$ = 0.9–1.2], and have high alkaline contents ($Na_2O + K_2O$ = 8.13–11.34 wt%). They are all characterized by enrichment in LILEs (LREE, Rb, Ba, Th, U, K, and Pb), and depletion in HFSEs (Ta, Nb, and Ti), and have high Sr/Y ratios of 75 ± 31. They have high initial $^{87}Sr/^{86}Sr$ ratios (0.7068–0.7071) and negative $\varepsilon_{Nd}(t)$ values (− 6.9 to − 5.0), with low zircon $\varepsilon_{Hf}(t)$ (− 5.3 to 4.5) and relatively high $\delta^{18}O$ values (5.9–9.0 ‰). Magmatic amphibole phenocryst compositions indicate that the parental magmas are all relatively oxidized, with estimated ΔFMQ values of 1.7 ± 0.6, and have relatively high H_2O contents (3.8 ± 0.3 wt%). These results are consistent with ΔFMQ values (1.8 ± 0.8) estimated from zircon compositions and high whole-rock Sr/Y ratios (75 ± 31), respectively.

These new data together with the previously published data for the fertile porphyries in the Eocence–Oligocene Jinshajiang–Ailaoshan porphyry Cu-Au-Mo belt in the Sanjiang region indicate that, despite a postcollisional tectonic setting, the Jinshajiang–Ailaoshan porphyry Cu-Au-Mo belt formed from relatively oxidized and hydrous magmas. We have demonstrated that such important features exhibited by the postcollisional porphyry deposits are mainly due to inheritance from a mantle source that was modified by previous subduction processes, and mixing with the juvenile arc lower-crust that formed from the ancient arc magmas. In the case of the Ailaoshan–Red River porphyry Au-Cu-Mo belt, such event took place in the Neoproterozoic. Whereas the subduction event took place from Permian to Triassic for the Yulong porphyry Cu-Mo belt in the East Qiangtang Block. In both cases, the mantle above the subduction zone was oxidized and hydrated by slab-derived fluids and subducted sediment-derived melts. Partial melting of the metasomatized SCLM at both locations after the amalgamation of the Asian and Indian continents due to lithospheric instability-induced delamination and lithospheric thinning produced an oxidized and hydrous fertile mafic melt. Underplating of such magma to the overlying juvenile lower-crust induced partial melting of the lower crust due to conductive heating. Mixing between these two end-members produced the parental magmas for the postcollisional porphyry deposits in the Sanjiang region. The porphyry deposits in the Ailaoshan–Red River belt are more enriched in Au possibly because the parental magmas had a high proportion of the mantle-derived end-member; those in the Yulong belt are more enriched in Mo probably because the parental magmas were dominated by the lower crust-derived end-member.

Supplementary Information The online version contains supplementary material available at https://doi.org/10.1007/s00126-022-01143-x.

Acknowledgements We thank Profs. Chusi Li from Indiana University and Pete Hollings from Lakehead University for revising the early version of this manuscript. Ph.D candidate Gong Liu is thanked for his assistance in compilation of geological maps and experimental work. We greatly appreciate the constructive comments and English edits from Editor-in-Chief Bernd Lehmann, Fabien Rabayrol and AE Celestine Mercer.

Funding This research was jointly funded by the Natural Science Foundation of China (91955209), the Team of "One Belt and One Road" of the Chinese Academy of Sciences, the Natural Science Foundation of China (42073047 and 41873052), the project under the Frontier Programme of the State Key Laboratory of Ore Deposit Geochemistry, and the 100 Innovative Talents of Guizhou province and Chinese Academy of Sciences.

Declarations

Conflict of interest The authors declare no competing interests.

References

Arculus RJ (1994) Aspects of magma genesis in arcs. Lithos 33:189–208

Baker M, Hirschmann M, Ghiorso M, Stolper E (1995) Compositions of near-solidus peridotite melts from experiments and thermodynamic calculations. Nature 375:308–311

Ballard JR, Palin JM, Campbell IH (2002) Relative oxidation states of magmas inferred from $Ce^{(IV)}/Ce^{(III)}$ in zircon: application to porphyry copper deposits of northern Chile. Contrib Mineral Petrol 144:347–364

Bao X-S, He W-Y, Gao X (2017) The Beiya gold deposit: constraint from water-rich magmas to mineralization. Acta Petrol Sin 33:2175–2188 (in Chinese with English abstract)

Behrens H, Misiti V, Freda C, Vetere F, Botcharnikov RE, Scarlato P (2009) Solubility of H_2O and CO_2 in ultrapotassic melts at 1200 and 1250 C and pressure from 50 to 500 MPa. Am Mineral 94:105–120

Bell AS, Simon A (2011) Experimental evidence for the alteration of the Fe3+/ΣFe of silicate melt caused by the degassing of chlorine-bearing aqueous volatiles. Geology 39:499–502

Bi X-W, Hu R-Z, Cornell D (2004) The alkaline porphyry associated Yao'an gold deposit, Yunnan, China: rare earth element and stable isotope evidence for magmatic-hydrothermal ore formation. Mineral Deposita 39:21–30

Bi X-W, Hu R-Z, Peng J-T, Wu K-X, Su W-C, Zhan X-Z (2005) Geochemical characteristics of the Yao'an and Machangqing alkaline-rich intrusions. Acta Petrol Sin 21:113–124 (in Chinese with English abstract)

Bi X-W, Hu R-Z, Hanley JJ, Mungall J, Peng J-T, Shang L-B, Wu K-X, Suang Y, Li H-L, Hu X-Y (2009) Crystallisation conditions (T, P, fO_2) from mineral chemistry of Cu- and Au-mineralised alkaline intrusions in the Red River-Jinshajiang alkaline igneous belt, western Yunnan Province, China. Mineral Petrol 96:43–58

Brounce MN, Kelley KA, Cottrell E (2014) Variations in Fe3+/∑Fe of mariana arc basalts and mantle wedge fO_2. J Petrol 55:2513–2536

Brounce M, Stolper E, Eiler J (2017) Redox variations in Mauna Kea lavas, the oxygen fugacity of the Hawaiian plume, and the role of volcanic gases in Earth's oxygenation. Proc Natl Acad Sci 114:8997–9002

Burnham CW (1979) Magmas and hydrothermal fluids, in Barnes, H.L., ed., Geochemistry of hydrothermal ore deposits, 2nd ed.: New York, John Wiley and Sons pp.71–136

Campbell IH, Stepanov AS, Liang H-Y, Allen CM, Norman MD, Zhang Y-Q, Xie Y-W (2014) The origin of shoshonites: new insights from the Tertiary high-potassium intrusions of eastern Tibet. Contrib Mineral Petrol 167:1–22

Cao M-J, Hollings P, Cooke DR, Evans NJ, McInnes BI, Qin K-Z, Li G-M, Sweet G, Baker M (2018) Physicochemical processes in the magma chamber under the black mountain porphyry Cu-Au deposit, Philippines: insights from mineral chemistry and implications for mineralization. Econ Geol 113:63–82

Cawood PA, Zhao G-C, Yao J-L, Wang W, Xu Y-J, Wang Y-J (2018) Reconstructing South China in Phanerozoic and Precambrian supercontinents. Earth-Sci Rev 186:173–194

Chang J, Li J-W, Selby D, Liu J-C, Deng X-D (2017) Geological and chronological constraints on the long-lived eocene yulong porphyry Cu-Mo deposit, Eastern Tibet: implications for the lifespan of giant porphyry Cu deposits. Econ Geol 112:1719–1746

Chelle-Michou C, Chiaradia M (2017) Amphibole and apatite insights into the evolution and mass balance of Cl and S in magmas associated with porphyry copper deposits. Contrib Mineral Petrol 172:105

Chiaradia M, Merino D, Spikings R (2009) Rapid transition to long-lived deep crustal magmatic maturation and the formation of giant porphyry-related mineralization (Yanacocha, Peru). Earth Planet Sci Lett 288:505–515

Chiaradia M, Ulianov A, Kouzmanov K, Beate B (2012) Why large porphyry Cu deposits like high Sr/Y magmas? Sci Reports 2:685

Chiaradia M (2021) Magmatic controls on metal endowments of porphyry Cu-Au deposits. SEG Spec Publ 24:1–16

Chou IM (1978) Calibration of oxygen buffers at elevated-P and elevated-T using hydrogen fugacity sensor. Am Mineral 63:690–703

Chung S-L, Lee T-Y, Lo C-H, Wang P-L, Chen C-Y, Yem N-T, Hoa T-T, Wu G-Y (1997) Intraplate extension prior to continental extrusion along the Ailao Shan Red River shear zone. Geology 25:311–314

Chung S-L, Liu D, Ji J, Chu M-F, Lee H-Y, Wen D-J, Lo C-H, Lee T-Y, Qian Q, Zhang Q (2003) Adakites from continental collision zones: melting of thickened lower crust beneath southern Tibet. Geology 31:1021–1024

Chung S-L, Chu M-F, Zhang Y, Xie Y, Lo C-H, Lee T-Y, Lan C-Y, Li X, Zhang Q, Wang Y (2005) Tibetan tectonic evolution inferred from spatial and temporal variations in post-collisional magmatism. Earth-Sci Rev 68:73–196

Collins WJ, Huang H-Q, Jiang X (2016) Water-fluxed crustal melting produces Cordilleran batholiths. Geology 44:143–146

Cooke DR, Hollings P, Walsh JL (2005) Giant porphyry deposits: characteristics, distribution, and tectonic controls. Econ Geol 100:801–818

Cottrell E, Kelley KA (2011) The oxidation state of Fe in MORB glasses and the oxygen fugacity of the upper mantle. Earth Planet Sci Lett 305:270–282

Davidson J, Turner S, Handley H, Macpherson C, Dosseto A (2007) Amphibole "sponge" in arc crust? Geology 35:787–790

Deng J, Wang Q-F, Li G-J, Li C-S, Wang C-M (2014) Tethys tectonic evolution and its bearing on the distribution of important mineral deposits in the Sanjiang region, SW China. Gondwana Res 26:419–437

Deng J, Wang Q-F, Li G-J, Santosh M (2014) Cenozoic tectono-magmatic and metallogenic processes in the Sanjiang region, southwestern China. Earth-Sci Rev 138:268–299

Deng J, Wang Q-F, Li G-J, Hou Z-Q, Jiang C-Z, Danyushevsky L (2015) Geology and genesis of the giant Beiya porphyry-skarn gold deposit, northwestern Yangtze Block, China. Ore Geol Rev 70:457–485

Deng W-M (1998) Cenozoic intraplate volcanic rocks in the Northern Qinghai–Xizang (Tibetan) plateau. Beijing, Geological Publishing House, 180 p. (in Chinese with English abstract)

Ding L, Kapp P, Zhong D-L, Deng W-M (2003) Cenozoic volcanism in Tibet: evidence for a transition from oceanic to continental subduction. J Petrol 44:1833–1865

Eiler JM (2001) Oxygen isotope variations of basaltic lavas and upper mantle rocks. Rev Mineral Geochem 43:319–364

Evans KA, Tomkins AG (2011) The relationship between subduction zone redox budget and arc magma fertility. Earth Planet Sci Lett 308:401–409

Ferry J, Watson E (2007) New thermodynamic models and revised calibrations for the Ti-in-zircon and Zr-in-rutile thermometers. Contrib Mineral Petrol 154:429–437

Gregory RT, Taylor HP (1981) An oxygen isotope profile in a section of Cretaceous oceanic crust, Samail Ophiolite, Oman: evidence for $\delta^{18}O$ buffering of the oceans by deep (>5 km) seawater-hydrothermal circulation at mid-ocean ridges. J Geophys Res 86:2737–2755

Griffin WL, Begg GC, O'Reilly SY (2013) Continental-root control on the genesis of magmatic ore deposits. Nat Geosci 6:905–910

Grocke SB, Cottrell E, de Silva S, Kelley KA (2016) The role of crustal and eruptive processes versus source variations in controlling the oxidation state of iron in Central Andean magmas. Earth Planet Sci Lett 440:92–104

Guo Z-F, Hertogen J, Liu J-Q, Pasteels P, Boven A, Punzalan L, He H-Y, Luo X-J, Zhang W-H (2005) Potassic magmatism in western Sichuan and Yunnan Provinces, SE Tibet, China: Petrological and geochemical constraints on petrogenesis. J Petrol 46:33–78

Guo Z-F, Wilson M, Liu J-Q, Mao Q (2006) Post-collisional, potassic and ultrapotassic magmatism of the northern tibetan plateau: constraints on characteristics of the mantle source, geodynamic setting and uplift mechanisms. J Petrol 47:1177–1220

Guynn JH, Kapp P, Pullen A, Heizler M, Gehrels G, Ding L (2006) Tibetan basement rocks near Amdo reveal “missing” Mesozoic tectonism along the Bangong suture, central Tibet. Geology 34:505–508

Hao J-H, Chen J-P, Dong Q-J, Tian Y-G, Li Y-C, Chen D (2012) Zircon LA-ICPMS U-Pb dating for Narigongma porphyry Mo–Cu deposit in southern Qinghai province and its geological implication. Geosci 26:45–53 (in Chinese with English abstract)

He W-Y, Mo X-X, Yu X-H, Li Y, Huang X-K, He Z-H (2011) Geochronological study of magmatic intrusions and mineralization of Machangqing porphyry Cu–Mo–Au deposit, western Yunnan Province. Earth Sci Front 1:207–215 (in Chinese with English abstract)

He W-Y, Mo X-X, He Z-H, White NC, Chen J-B, Yang K-H, Wang R, Yu X-H, Dong G-C, Huang X-F (2015) The geology and mineralogy of the Beiya skarn gold deposit in Yunanan, southwest China. Econ Geol 110:1625–1641

He W-Y, Mo X-X, Yang L-Q, Xing Y-L, Dong G-C, Yang Z, Gao X, Bao X-S (2016) Origin of the Eocene porphyries and mafic microgranular enclaves from the Beiya porphyry Au polymetallic deposit, western Yunnan, China: implications for magma mixing/mingling and mineralization. Gondwana Res 40:230–248

Heinrich C, Günther D, Audétat A, Ulrich T, Frischknecht R (1999) Metal fractionation between magmatic brine and vapor, determined by microanalysis of fluid inclusions. Geology 27:755–758

Hildreth W, Moorbath S (1988) Crustal contributions to arc magmatism in the Andes of central Chile. Contrib Mineral Petrol 98:455–489

Holwell DA, Fiorentini M, McDonald I, Lu Y-J, Giuliani A, Smith DJ, Keith M, Locmelis M (2019) A metasomatized lithospheric mantle control on the metallogenic signature of post-subduction magmatism. Nat Commun 10:3511

Hou Z-Q, Ma H-W, Zaw K, Zhang Y-Q, Wang M-J, Wang Z, Pan G-T, Tang R-L (2003) The Himalayan Yulong porphyry copper belt: product of large-scale strike slip faulting in eastern Tibet. Econ Geol 98:125–145

Hou Z-Q, Gao Y-F, Qu X-M, Rui Z-Y, Mo X-X (2004) Origin of adakitic intrusives generated during mid-Miocene east–west extension in southern Tibet. Earth Planet Sci Lett 220:139–155

Hou Z-Q, Zeng P-S, Gao Y-F, Du A-D, Fu D-M (2006) Himalayan Cu-Mo-Au mineralization in the eastern Indo-Asian collision zone: constraints from Re-Os dating of molybdenite. Mineral Deposita 41:33–45

Hou Z-Q, Zaw K, Pan G-T, Mo X-X, Xu Q, Hu Y-Z, Li X-Z (2007) Sanjiang Tethyan metallogenesis in SW China: tectonic setting, metallogenic epochs and deposit types. Ore Geol Rev 31:48–87

Hou Z-Q, Xie Y-L, Xu W-Y, Li Y-Q, Huang W, Luobu C-R (2007) Yulong deposit, East Tibet: a high-sulfidation Cu–Au porphyry Cu deposit in the eastern Indo-Asian collision zone. Int Geol Rev 49:235–259

Hou Z-Q, Zhang H-R, Pan X-F, Yang Z-M (2011) Porphyry Cu (-Mo-Au) deposits related to melting of thickened mafic lower crust: examples from the eastern Tethyan metallogenic domain. Ore Geol Rev 39:21–45

Hou Z-Q, Zheng Y-C, Yang Z-M, Rui Z-Y, Zhao Z-D, Jiang S-H, Qu X-M, Sun Q-Z (2013) Contribution of mantle components within juvenile lower-crust to collisional zone porphyry Cu systems in Tibet. Mineral Deposita 48:173–192

Hou Z-Q, Yang Z-M, Lu Y-J, Kemp A, Zheng Y-C, Li Q-Y, Tang J-X, Yang Z-S, Duan L-F (2015) A genetic linkage between subduction- and collision-related porphyry Cu deposits in continental collision zones. Geology 43:247–250

Hou Z, Duan L, Lu Y, Zheng Y, Zhu D, Yang Z, Yang Z, Wang B, Pei Y, Zhao Z, McCuaig TC (2015) Lithospheric architecture of the lhasa terrane and its control on ore deposits in the Himalayan-Tibetan Orogen. Econ Geol 110:1541–1575

Hou Z-Q, Zhou Y, Wang R, Zheng Y-C, He W-Y, Zhao M, Evans NJ, Weinberg RF (2017) Recycling of metal-fertilized lower continental crust: origin of non-arc Au-rich porphyry deposits at cratonic edges. Geology 45:563–566

Hou Z-Q, Wang T (2018) Isotopic mapping and deep material probing (II): imaging crustal architecture and its control on mineral systems. Earth Sci Front 25:20–41 (in Chinese with English abstract)

Hou Z, Wang R (2019) Fingerprinting metal transfer from mantle. Nat Commun 10:1

Hronsky JMA, Groves DI, Loucks RR, Begg GC (2012) A unified model for gold mineralisation in accretionary orogens and implications for regional-scale exploration targeting methods. Mineral Deposita 47:339–358

Hu R-Z, Burnard PG, Turner G, Bi X-W (1998) Helium and Argon isotope systematics in fluid inclusions of Machangqing copper deposit in west Yunnan province, China. Chem Geol 146:55–63

Hu R-Z, Burnard PG, Bi X-W, Zhou M-F, Pen J-T, Su W-C, Wu K-X (2004) Helium and argon isotope geochemistry of alkaline intrusion-associated gold and copper deposits along the Red River-Jinshajiang fault belt, SW China. Chem Geol 203:305–317

Huang M-L, Bi X-W, Gao J-F, Hu R-Z, Xu L-L, Zhu J-J (2019) Geochemistry, in-situ Sr-Nd-Hf-O isotopes, and mineralogical constraints on origin and magmatic-hydrothermal evolution of the Yulong porphyry Cu-Mo deposit, Eastern Tibet. Gondwana Res 76:98–114

Huang M-L, Bi X-W, Richards JP, Hu R-Z, Xu L-L, Gao J-F, Zhu JJ, Zhang X-C (2019) High water contents of magmas and extensive fluid exsolution during the formation of the Yulong porphyry Cu-Mo deposit, eastern Tibet. J Asian Earth Sci 176:168–183

Huang X-L, Niu Y-L, Xu Y-G, Chen L-L, Yang Q-J (2010) Mineralogical and geochemical constraints on the petrogenesis of post-collisional potassic and ultrapotassic rocks from Western Yunnan, SW China. J Petrol 51:1617–1654

Irvine T, Baragar W (1971) A guide to the chemical classification of the common volcanic rocks. Can J Earth Sci 8:523–548

Jahn B-M, Wu F-Y, Capdevila R, Fourcade S, Wang Y-X, Zhao Z-H (2001) Highly evolved juvenile granites with tetrad REE patterns: the Woduhe and Baerzhe granites from the Great Xing'an (Khingan) Mountains in NE China. Lithos 59:171–198

Jahn B-M, Wu F-Y, Lo C-H, Tsai C-H (1999) Crust-mantle interaction induced by deep subduction of the continental crust: Geochemical and Sr-Nd isotopic evidence from post-collisional mafic–ultramafic intrusions of the northern Dabie complex, central China. Chem Geol 157:119–146

Jian P, Liu D-Y, Kröner A, Zhang Q, Wang Y-Z, Sun XM, Zhang W (2009) Devonian to Permian plate tectonic cycle of the Paleo-Tethys Orogen in southwest China (II): insights from zircon ages of ophiolites, arc/back-arc assemblages and within-plate igneous rocks and generation of the Emeishan CFB province. Lithos 113:767–784

Jiang Y-H, Jiang S-Y, Ling H-F, Dai B-Z (2006) Low-degree melting of metasomatized lithospheric mantle for the origin of Cenozoic Yulong monzogranite-porphyry, east Tibet: geochemical and Sr–Nd–Pb–Hf isotopic constraints. Earth Planet Sci Lett 241:617–633

Jugo PJ, Luth RW, Richards JP (2005) Experimental data on the speciation of sulfur as a function of oxygen fugacity in basaltic melts. Geochim Cosmochim Acta 69:497–503

Jugo PJ (2009) Sulfur content at sulfide saturation in oxidized magmas. Geology 37:415–418

Kapp P, DeCelles PG, Gehrels GE, Heizler M, Ding L (2007) Geological records of the Lhasa-Qiangtang and Indo-Asian collisions in the Nima area of central Tibet. Geol Soc Am Bull 119:917–933

Kelley KA, Cottrell E (2012) The influence of magmatic differentiation on the oxidation state of Fe in a basaltic arc magma. Earth Planet Sci Lett 329:109–121

Kemp AIS, Hawkesworth CJ (2003) Granitic perspectives on the generation and secular evolution of the continental crust. Treatise Geochem 3:349–410
Kemp AIS, Hawkesworth CJ, Foster GL, Paterson BA, Woodhead JD, Hergt JM, Gray CM, Whitehouse MJ (2007) Magmatic and crustal differentiation history of granitic rocks from Hf-O isotopes in zircon. Science 315:980–983
Li J-X, Qin K-Z, Li G-M, Cao M-J, Xiao B, Chen L, Zhao J-X, Evans NJ, McInnes BIA (2012) Petrogenesis and thermal history of the Yulong porphyry copper deposit, Eastern Tibet: insights from U-Pb and U-Th/He dating, and zircon Hf isotope and trace element analysis. Mineral Petrol 105:201–221
Li W-C, Wang J-H, He Z-H, Dou S (2016) Formation of Au-polymetallic ore deposits in alkaline porphyries at Beiya, Yunnan, Southwest China. Ore Geol Rev 73:241–252
Li WK, Yang ZM, Cao K, Lu YJ, Sun MY (2019) Redox-controlled generation of the giant porphyry Cu–Au deposit at Pulang, southwest China. Contrib Mineral Petrol 174:12
Li WK, Yang ZM, Chiaradia M, Lai Y, Yu C, Zhang JY (2020) Redox state of southern Tibetan upper mantle and ultrapotassic magmas. Geology 48:733–736
Li Z-X (1998) Tectonic history of the major East Asian lithospheric Blocks since the mid-Proterozoic—a synthesis. Geodynamics Seri, Am Geophys Union 27:221–243
Liang H-Y, Campbell IH, Allen C, Sun W-D, Liu C-Q, Yu H-X, Xie Y-W, Zhang Y-Q (2006) Zircon Ce^{4+}/Ce^{3+} ratios and ages for Yulong ore-bearing porphyries in eastern Tibet. Mineral Deposita 41:152–159
Liang H-Y, Sun W, Su W-C, Zartman RE (2009) Porphyry copper-gold mineralization at Yulong, China, promoted by decreasing redox potential during magnetite alteration. Econ Geol 104:587–596
Lin B, Wang L-Q, Tang J-X, Song Y, Zhou X, Liu Z-B, Gao Y-M, Tang X-Q, Xu R-G, Chen Z-J (2017) Zircon U-Pb geochronology of ore-bearing porphyries in Baomai deposit, Yulong copper belt. Tibet Earth Sci 42:1454–1471 (in Chinese with English abstract)
Lin B, Wang L-Q, Tang J-X, Song Y, Cao H-W, Baker MJ, Zhang L-J, Zhou X (2018) Geology, geochronology, geochemical characteristics and origin of Baomai porphyry Cu (Mo) deposit, Yulong Belt. Tibet Ore Geol Rev 92:186–204
Locock AJ (2014) An Excel spreadsheet to classify chemical analyses of amphiboles following the IMA 2012 recommendations. Comput Geosci 62:1–11
Loucks RR, Fiorentini ML, Henríquez GJ (2020) New magmatic oxybarometer using trace elements in zircon. J Petrol 61.https://doi.org/10.1093/petrology/egaa034
Logan JM, Mihalynuk MG (2014) Tectonic Controls on Early Mesozoic Paired Alkaline Porphyry Deposit Belts (Cu-Au +/- Ag-Pt-Pd-Mo) Within the Canadian Cordillera. Econ Geol 109:827–858
Lu Y-J, Kerrich R, Cawood PA, McCuaig TC, Hart CJR, Li Z-X, Hou Z-Q, Bagas L (2012) Zircon SHRIMP U-Pb geochronology of potassic felsic intrusions in western Yunnan, SW China: Constraints on the relationship of magmatism to the Jinsha suture. Gondwana Res 22:737–747
Lu Y-J, Kerrich R, Kemp AIS, McCuaig TC, Hou Z-Q, Hart CJR, Li Z-X, Cawood PA, Bagas L, Yang Z-M, Cliff J, Belousova EA, Jourdan F, Evans NJ (2013) Intracontinental Eocene-Oligocene porphyry Cu mineral systems of Yunnan, Western Yangtze Craton, China: compositional characteristics, sources, and implications for continental collision metallogeny. Econ Geol 108:1541–1576
Lu Y-J, Kerrich R, McCuaig TC, Li Z-X, Hart CJR, Cawood PA, Hou Z-Q, Bagas L, Cliff J, Belousova EA, Tang S-H (2013) Geochemical, Sr-Nd-Pb, and zircon Hf-O isotopic compositions of Eocene-Oligocene Shoshonitic and Potassic Adakite-like Felsic Intrusions in Western Yunnan, SW China: Petrogenesis and Tectonic Implications. J Petrol 54:1309–1348
Lu Y-J, Loucks RR, Fiorentini ML, Yang Z-M, Hou Z-Q (2015) Fluid flux melting generated postcollisional high Sr/Y copper ore-forming water-rich magmas in Tibet. Geology 43:583–586
Lu Y-J, McCuaig TC, Li Z-X, Jourdan F, Hart CJR, Hou Z-Q, Tang S-H (2015) Paleogene post-collisional lamprophyres in western Yunnan, western Yangtze Craton: Mantle source and tectonic implications. Lithos 233:139–161
Lu Y-J, Loucks RR, Fiorentini M, McCuaig TC, Evans NJ, Yang Z-M, Hou Z-Q, Kirkland CL, Parra-Avila LA, Kobussen A (2016) Zircon compositions as a pathfinder for porphyry Cu±Mo±Au deposits. Soc Econ Geol Spec Publ 19:329–347
Macpherson CG (2008) Lithosphere erosion and crustal growth in subduction zones: insights from initiation of the nascent East Philippine Arc. Geology 36:311–314
Mao J-W, Zhang Z-C, Zhang Z-H, Du A-D (1999) Re-Os isotopic dating of molybdenites in the Xiaoliugou W (Mo) deposit in the northern Qilian mountains and its geological significance. Geochim Cosmochim Acta 63:1815–1818
Mao J-W, Zhou Y-M, Liu H, Zhang C-Q, Fu D-G, Liu B (2017) Metallogenic setting and ore genetic model for the Beiya porphyry-skarn polymetallic Au orefield, western Yunnan, China. Ore Geol Rev 86:21–34
McInnes BI, McBride JS, Evans NJ, Lambert DD, Andrew AS (1999) Osmium isotope constraints on ore metal recycling in subduction zones. Science 286:512–516
Meng X-Y, Mao J-W, Zhang C-Q, Zhang D-Y, Liu H (2018) Melt recharge, fO_2-T conditions, and metal fertility of felsic magmas: zircon trace element chemistry of Cu-Au porphyries in the Sanjiang orogenic belt, southwest China. Mineral Deposita 53:649–663
Metcalfe I (2002) Permian tectonic framework and palaeogeography of SE Asia. J Asian Earth Sci 20:551–566
Metcalfe I (2006) Palaeozoic and Mesozoic tectonic evolution and palaeogeography of East Asian crustal fragments: the Korean Peninsula in context. Gondwana Res 9:24–46
Metcalfe I (2013) Gondwana dispersion and Asian accretion: tectonic and palaeogeographic evolution of eastern Tethys. J Asian Earth Sci 66:1–33
Middlemost EA (1994) Naming materials in the magma/igneous rock system. Earth-Sci Rev 37:215–224
Mo X-X, Deng J-F, Lu F-X (1994) Volcanism and the evolution of Tethys in Sanjiang area, southwestern China. J Southeast Asian Earth Sci 9:325–333
Mungall JE (2002) Roasting the mantle: Slab melting and the genesis of major Au and Au-rich Cu deposits. Geology 30:915–918
Muñoz M, Charrier R, Fanning CM, Maksaev V, Deckart K (2012) Zircon trace element and O-Hf isotope analyses of mineralized intrusions from El Teniente ore deposit, Chilean Andes: constraints on the source and magmatic evolution of porphyry Cu–Mo related magmas. J Petrol 53:1091–1122
Murakami H, Seo JH, Heinrich CA (2010) The relation between Cu/Au ratio and formation depth of porphyry-style Cu-Au +/- Mo deposits. Mineral Deposita 45:11–21
Mutch E, Blundy J, Tattitch B, Cooper F, Brooker R (2016) An experimental study of amphibole stability in low-pressure granitic magmas and a revised Al-in-hornblende geobarometer. Contrib Mineral Petrol 171:85
O'Neill HS, Pownceby MI (1993) Thermodynamic data from redox reactions at high-temperatures. 1. An experimental and theoretical assessment of the electrochemical method using stabilized zirconia electrolytes, with revised values for the Fe-FeO, CO-COO, Ni-NiO and Cu-Cu_2O oxygen buffers, and new data for the W-WO_2 buffer. Contrib Mineral Petrol 114:296–314
O'Neill HS (1987) Quartz-Fayalite-Iron and Quartz-Fayalite-Magnetite equilibria and the free-energy of formation of fayalite (Fe_2SiO4) and magnetite (Fe_3O_4). Am Mineral 72:67–75

Pan G-T, Ding J, Yao D-S, Wang L-Q (2004) Guidebook of 1:1,500,000 geologic map of the Qinghai-Xizang (Tibet) plateau and adjacent areas 1–148. Cartographic Publishing House, Chengdu, China
Park J-W, Campbell IH, Chiaradia M, Hao H, Lee C-T (2021) Crustal magmatic controls on the formation of porphyry copper deposits. Nat Rev Earth Environ 2:542–557
Plank T, Kelley KA, Zimmer MM, Hauri EH, Wallace PJ (2013) Why do mafic arc magmas contain ~4 wt% water on average? Earth Planet Sci Lett 364:168–179
Pullen A, Kapp P, Gehrels GE, Vervoort JD, Ding L (2008) Triassic continental subduction in central Tibet and Mediterranean-style closure of the Paleo-Tethys Ocean. Geology 36:351–354
Qiu X-F, Ling W-L, Liu X-M, Lu S-S, Jiang T, Wei Y-X, Peng L-H, Tan J-J (2018) Evolution of the Archean continental crust in the nucleus of the Yangtze block: evidence from geochemistry of 3.0 Ga TTG gneisses in the Kongling high-grade metamorphic terrane. South China J Asian Earth Sci 154:149–161
Richards JP (2003) Tectono-magmatic precursors for porphyry Cu-(Mo-Au) deposit formation. Econ Geol Bull Soc Econ Geol 98:1515–1533
Richards JR, Kerrich R (2007) Special paper: Adakite-like rocks: their diverse origins and questionable role in metallogenesis. Econ Geol 102:537–576
Richards JP (2009) Postsubduction porphyry Cu-Au and epithermal Au deposits: Products of remelting of subduction-modified lithosphere. Geology 37:247–250
Richards JP (2011) High Sr/Y magmas and porphyry Cu±Mo±Au deposits: just add water. Econ Geol 106:1075–1081
Richards JP (2011) Magmatic to hydrothermal metal fluxes in convergent and collided margins. Ore Geol Rev 40:1–26
Richards JP, Spell T, Rameh E, Razique A, Fletcher T (2012) High Sr/Y magmas reflect arc maturity, high magmatic water content, and porphyry Cu ± Mo ± Au potential: examples from the Tethyan Arcs of Central and Eastern Iran and Western Pakistan. Econ Geol 107:295–332
Richards JP (2015) The oxidation state, and sulfur and Cu contents of arc magmas: implications for metallogeny. Lithos 233:27–45
Richards JP (2015) Tectonic, magmatic, and metallogenic evolution of the Tethyan orogen: from subduction to collision. Ore Geol Rev 70:323–345
Richards JP, Celâl Şengör AM (2017) Did Paleo-Tethyan anoxia kill arc magma fertility for porphyry copper formation? Geology 45:591–594
Ridolfi F, Renzulli A, Puerini M (2010) Stability and chemical equilibrium of amphibole in calc-alkaline magmas: an overview, new thermobarometric formulations and application to subduction-related volcanoes. Contrib Mineral Petrol 160:45–66
Ringwood AE (1977) Petrogenesis in island arc systems, in Talwani, M., and Pitman, W.C., eds., Island arcs, deep sea trenches, and back arc basins: American Geophysical Union [Maurice Ewing Series II:311–324
Rutherford MJ, Devine JD (1988) The May 18, 1980, eruption of Mount St.Helens. 3. Stability and chemistry of amphibole in the magma chamber. J Geophys Res 93:11949–11959
Shafiei B, Haschke M, Shahabpour J (2009) Recycling of orogenic arc crust triggers porphyry Cu mineralization in Kerman Cenozoic arc rocks, southeastern Iran. Mineral Deposita 44:265–283
Shen P, Hattori K, Pan H, Jackson S, Seitmuratova E (2015) Oxidation condition and metal fertility of granitic magmas: zircon trace-element data from porphyry Cu deposits in the Central Asian Orogenic Belt. Econ Geol 110:1861–1878
Shen Y, Zheng Y-C, Ma R, Zhang A-P, Xu P-Y, Wu C-D, Wang Z-X (2018) Mineralogical characteristics of hornblendes and biotites in ore-forming porphyry from Machangqing Cu-Mo deposit in Yunnan Province and their significance. Miner Deposits 37:797–815 (in Chinese with English abstract)
Shen Y, Zheng Y-C, Hou Z-Q, Zhang A-P, Huizenga JM, Wang Z-X, Wang L (2021) Petrology of the Machangqing Complex in southeastern Tibet: implications for the genesis of potassium-rich adakite-like intrusions in collisional zones. J Petrol 62. https://doi.org/10.1093/petrology/egab066
Sillitoe RH (2010) Porphyry Copper Systems. Econ Geol 105:3–41
Spurlin MS, Yin A, Horton BK, Zhou J, Wang J (2005) Structural evolution of the Yushu-Nangqian region and its relationship to syncollisional igneous activity, east-central Tibet. Geol Soc Ame Bull 117:1293–1317
Sun S-S, McDonough WF (1989) Chemical and isotopic systematics of oceanic basalts: implications for mantle composition and processes. Geol Soc London Spe Publ 42:313–345
Sun W-D, Li C-Y, Ling M-X, Ding X, Yang X-Y, Liang H-Y, Zhang H, Fan W-M (2015) The Geochemical Behavior of Molybdenum and Mineralization. Acta Petrol Sin 31:1807–1817
Tang M, Erdman M, Eldridge G, Lee C-TA (2018) The redox "filter" beneath magmatic orogens and the formation of continental crust. Sci Adv 4:1–7
Tang R-L, Luo H-S (1995) The geology of Yulong porphyry copper (molybdenum) ore belt, Xizang (Tibet). Beijing, Geological Publishing House, 320 p. (in Chinese with English abstract)
Tao Y, Bi X-W, Li C-S, Hu R-Z, Li Y-B, Liao M-Y (2014) Geochronology, petrogenesis and tectonic significance of the Jitang granitic pluton in eastern Tibet, SW China. Lithos 184–187:314–323
Tattitch BC, Blundy JD (2017) Cu-Mo partitioning between felsic melts and saline-aqueous fluids as a function of XNaCleq, fO_2, and fS2. Am Mineral 102:1987–2006
Trail D, Watson EB, Tailby ND (2011) The oxidation state of Hadean magmas and implications for early Earth's atmosphere. Nature 480:79–82
Trail D, Watson EB, Tailby ND (2012) Ce and Eu anomalies in zircon as proxies for the oxidation state of magmas. Geochim Cosmochim Acta 97:70–87
Turner S, Hawkesworth C, Liu J-Q, Rogers N, Kelley S, van Calsteren P (1993) Timing of Tibetan uplift constrained by analysis of volcanic rocks. Nature 364:50–54
Turner S, Arnaud N, Liu J-Q, Rogers N, Hawkesworth C, Harris N, Kelley S, van Calsteren P, Deng W-M (1996) Postcollision, shoshonitic volcanism on the Tibetan Plateau: implications for convective thinning of the lithosphere and the source of ocean island basalts. J Petrol 37:45–71
Valley JW, Kinny PD, Schulze DJ, Spicuzza MJ (1998) Zircon megacrysts from kimberlite: oxygen isotope variability among mantle melts. Contrib Mineral Petrol 133:1–11
Wainwright AJ, Tosdal RM, Wooden JL, Mazdab FK, Friedman RM (2011) U-Pb (zircon) and geochemical constraints on the age, origin, and evolution of Paleozoic arc magmas in the Oyu Tolgoi porphyry Cu–Au district, southern Mongolia. Gondwana Res 19:764–787
Wallace PJ (2005) Volatiles in subduction zone magmas: concentrations and fluxes based on melt inclusion and volcanic gas data. J Volcanol Geotherm Res 140:217–240
Wang J, Wang Q, Xu C-B, Dan W, Xiao Z, Shu C, Wei G (2022) Cenozoic delamination of the southwestern Yangtze craton owing to densification during subduction and collision. Geology 50:912–917
Wang Q, McDermott F, Xu J-F, Bellon H, Zhu Y-T (2005) Cenozoic K-rich adakitic volcanic rocks in the Hohxil area, northern Tibet: lower-crustal melting in an intracontinental setting. Geology 33:465
Wang Q, Wyman DA, Xu J-F, Dong Y-H, Vasconcelos PM, Pearson N, Wan Y-S, Dong H, Li CF, Yu Y-S, Zhu T-X, Feng X-T, Zhang Q-Y, Zi F, Chu Z-Y (2008) Eocene melting of subducting continental crust and early uplifting of central Tibet: evidence from central-western Qiangtang high-K calc-alkaline andesites, dacites and rhyolites. Earth Planet Sci Lett 272:158–171

Wang Q, Hawkesworth CJ, Wyman D, Chung S-L, Wu F-Y, Li X-H, Li Z-X, Gou G-N, Zhang X-Z, Tang G-J, Dan W, Ma L, Dong Y-H (2016) Pliocene-Quaternary crustal melting in central and northern Tibet and insights into crustal flow. Nat Commun 7:1–7

Wang R, Richards JP, Hou Z-Q, Yang Z-M, Gu Z-B, DuFrane SA (2014) Increasing magmatic oxidation state from Paleocene to Miocene in the Eastern Gangdese Belt, Tibet: Implication for Collision-Related Porphyry Cu-Mo +/- Au Mineralization. Econ Geol 109:1943–1965

Wang R, Richards JP, Hou Z-Q, Yang Z-M, DuFrane SA (2014) Increased magmatic water content-the key to oligo-miocene porphyry Cu-Mo +/- Au formation in the Eastern Gangdese Belt. Tibet Econ Geol 109:1315–1339

Wang R, Tafti R, Hou Z-Q, Shen Z-C, Guo N, Evans NJ, Jeon H, Li Q-Y, Li W-K (2017) Across-arc geochemical variation in the Jurassic magmatic zone, Southern Tibet: implication for continental arc-related porphyry Cu Au mineralization. Chem Geol 451:116–134

Wang R, Weinberg RF, Collins WJ, Richards JP, Zhu D-C (2018) Origin of postcollisional magmas and formation of porphyry Cu deposits in southern Tibet. Earth-Sci Rev 181:122–143

Wang X-F, Metcalfe I, Jian P, He L-Q, Wang C-S (2000) The Jinshajiang-Ailaoshan suture zone, China: tectonostratigraphy, age and evolution. J Asian Earth Sci 18:675–690

Wang Y-J, Qian X, Cawood PA, Liu H-C, Feng Q-L, Zhao G-C, Zhang Y-H, He H-Y, Zhang PZ (2018) Closure of the East Paleotethyan Ocean and amalgamation of the Eastern Cimmerian and Southeast Asia continental fragments. Earth-Sci Rev 186:195–230

Wang D (2013) The characteristics of volatile compositions and their constraints on the metallogenesis of Cenozoic alkali-rich magmas in the Jinshajiang−Red River belt. Ph.D. thesis, Institute of Geochemistry, Chinese Academy of Sciences, Guiyang (in Chinese with English abstract)

Weinberg RF, Hasalová P (2015) Water-fluxed melting of the continental crust: a review. Lithos 212–215:158–188

Wilkinson JJ (2013) Triggers for the formation of porphyry ore deposits in magmatic arcs. Nat Geosci 6:917–925

Winchester JA, Floyd PA (1977) Geochemical discrimination of different magma series and their differentiation products using immobile elements. Chemi Geol 20:325–343

Wu T, Xiao L, Ma C-Q, Huang W (2013) The geochronological, geochemical and Sr-Nd isotopic characteristics of Tongpu intrusive complex and its implications. Acta Petrol Sin 29:3567–3580 (in Chinese with English abstract)

Xia B, Lu Y, Yuan Y-J, Chen W-Y, Zhang X, Xu C, Yu S-R, Wan Z-F (2018) Mixing of enriched lithospheric mantle-derived and crustal magmas: evidence from the Habo cenozoic porphyry in western Yunnan. Acta Geol Sin-English Edition 92:1753–1768

Xie F-W, Tang J-X, Chen Y-C, Lang X-H (2018) Apatite and zircon geochemistry of Jurassic porphyries in the Xiongcun district, southern Gangdese porphyry copper belt: Implications for petrogenesis and mineralization. Ore Geol Rev 96:98–114

Xin D, Yang T-N, Liang M-J, Xue C-D, Han X, Liao C, Tang J (2018) Syn-subduction crustal shortening produced a magmatic flare-up in middle Sanjiang orogenic belt, southeastern Tibet Plateau: evidence from geochronology, geochemistry, and structural geology. Gondwana Res 62:93–111

Xu B, Hou Z-Q, Griffin WL, Lu Y, Belousova E, Xu J-F, O'Reilly SY (2021) Recycled volatiles determine fertility of porphyry deposits in collisional settings. Am Mineral 106:656–661

Xu X-W, Cai X-P, Xiao Q-B, Peters S-G (2007) Porphyry Cu-Au and associated polymetallic Fe-Cu-Au deposits in the Beiya Area, western Yunnan Province, south China. Ore Geol Rev 31:224–246

Xu L-L, Bi X-W, Hu R-Z, Zhang X-C, Su W-C, Qu W-J, Hu Z-C, Tang Y-Y (2012) Relationships between porphyry Cu–Mo mineralization in the Jinshajiang-Red River metallogenic belt and tectonic activity: constraints from zircon U-Pb and molybdenite Re–Os geochronology. Ore Geol Rev 48:460–473

Xu L-L, Bi X-W, Hu R-Z, Tang Y-Y, Jiang G-H, Qi Y-Q (2014) Origin of the ore-forming fluids of the Tongchang porphyry Cu–Mo deposit in the Jinshajiang-Red River alkaline igneous belt, SW China: constraints from He, Ar and S isotopes. J Asian Earth Sci 79:884–894

Xu L-L, Bi X-W, Hu R-Z, Tang Y-Y, Wang X-S, Xu Y (2015) LA-ICP-MS mineral chemistry of titanite and the geological implications for exploration of porphyry Cu deposits in the Jinshajiang-Red River alkaline igneous belt, SW China. Miner Petrol 109:181–200

Xu L-L, Bi X-W, Hu R-Z, Qi Y-Q, Tang Y-Y, Wang X-S, Zhu J-J (2016a) Redox states and genesis of magmas associated with intra-continental porphyry Cu-Au mineralization within the Jinshajiang-Red River alkaline igneous belt, SW China. Ore Geol Rev 73:330–345

Xu L-L, Bi X-W, Hu R-Z, Tang Y-Y, Wang X-S, Huang M-L, Wang Y-J, Ma R, Liu G (2019) Contrasting whole-rock and mineral compositions of ore-bearing (Tongchang) and ore-barren (Shilicun) granitic plutons in SW China: Implications for petrogenesis and ore genesis. Lithos 336–337:54–66

Xu Y, Bi X-W, Hu R-Z, Chen Y-W, Liu H-Q, Xu L-L (2016b) Geochronology and geochemistry of Eocene potassic felsic intrusions in the Nangqian basin, eastern Tibet: Tectonic and metallogenic implications. Lithos 246–247:212–227

Xu Y-G, Menzies MA, Thirlwall MF, Xie G-H (2001) Exotic lithosphere mantle beneath the western Yangtze Craton: petrogenetic links to Tibet using highly magnesian ultrapotassic rocks. Geology 29:863–866

Xu Y-G, Luo Z-Y, Huang X-L, He B, Xiao L, Xie L-W, Shi Y-R (2008) Zircon U-Pb and Hf isotope constraints on crustal melting associated with the Emeishan mantle plume. Geochim Cosmochim Acta 72:3084–3104

Yakovlev PV, Saal A, Clark MK, Hong C, Niemi NA, Mallick S (2019) The geochemistry of Tibetan lavas: spatial and temporal relationships, tectonic links and geodynamic implications. Earth Planet Sci Lett 520:115–126

Yan G-C, Wang B-D, Liu H, Li X-B, Zhou F (2018) Delineation of Middle Caboniferous arc volcanic rocks in Jomda area, eastern Tibet and its tectonic implications. Earth Sci 43:2715–2726

Yang M, Zhao F, Liu X, Qing H, Chi G, Li X, Duan W, Lai C (2020) Contribution of magma mixing to the formation of porphyry-skarn mineralization in a post-collisional setting: the Machangqing Cu-Mo-(Au) deposit, Sanjiang tectonic belt, SW China. Ore Geol Rev 122:103518

Yang T-N, Zhang H-R, Liu Y-X, Wang Z-L, Song Y-C, Yang Z-S, Tian S-H, Xie H-Q, Hou K-J (2011) Permo-Triassic arc magmatism in central Tibet: evidence from zircon U-Pb geochronology, Hf isotopes, rare earth elements, and bulk geochemistry. Chem Geol 284:270–282

Yang Z-M, Hou Z-Q, Xu J-F, Bian X-F, Wang G-R, Yang Z-S, Tian S-H, Liu Y-C, Wang Z-L (2014a) Geology and origin of the post-collisional Narigongma porphyry Cu–Mo deposit, southern Qinghai, Tibet. Gondwana Res 26:536–556

Yang T-N, Ding Y, Zhang H-R, Fan J-W, Liang M-J, Wang X-H (2014b) Two-phase subduction and subsequent collision defines the Paleotethyan tectonics of the southeastern Tibetan Plateau: evidence from zircon U-Pb dating, geochemistry, and structural geology of the Sanjiang orogenic belt, southwest China. Geol Soc Am Bull 126:1654–1682

Yang Z-M, Lu Y-J, Hou Z-Q, Chang Z-S (2015) High-Mg diorite from Qulong in Southern Tibet: Implications for the Genesis of Adakite-like Intrusions and Associated Porphyry Cu Deposits in Collisional Orogens. J Petrol 56:227–254

Yang Z-M, Goldfarb R, Chang Z-S (2016) Generation of postcollisional porphyry copper deposits in southern Tibet triggered by subduction of the Indian continental plate, in Richards, J.P., ed., Tectonics and Metallogeny of the Tethyan Orogenic Belt. SEG Spec Publ 19:279–300

Yang Z, Yang L-Q, He W-Y, Gao X, Liu X-D, Bao X-S, Lu Y-G (2017) Control of magmatic oxidation state in intracontinental porphyry mineralization: a case from Cu (Mo–Au) deposits in the Jinshajiang-Red River metallogenic belt, SW China. Ore Geol Rev 90:827–846

Yang Z-M, Cooke D (2019) Porphyry Cu deposits in China. Soc Econ Geol Spec Publ 22:133–187

Yao J-H, Zhu W-G, Li C-S, Zhong H, Bai Z-J, Ripley EM, Li C (2018) Petrogenesis and ore genesis of the lengshuiqing magmatic sulfide deposit in Southwest China: constraints from chalcophile elements (PGE, Se) and Sr-Nd-Os-S isotopes. Econ Geol 113:675–698

Yin A, Harrison TM (2000) Geologic evolution of the Himalayan-Tibetan orogen. Ann Rev Earth Planet Sci 28:211–280

Yulong Copper (Tibet Yulong Copper Co. Ltd.) (2009) Exploration report for theYulong porphyry copper deposit in Jiangda county, Tibet. Internal report pp1–397

Zajacz Z, Candela A, Piccoli M, Wälle M, Sanchez-Valle C (2012) Gold and copper in volatile saturated mafic to intermediate magmas: solubilities, partitioning, and implications for ore deposit formation. Geochim Cosmochim Acta 91:140–159

Zajacz Z, Candela PA, Piccoli PM (2017) The partitioning of Cu, Au and Mo between liquid and vapor at magmatic temperatures and its implications for the genesis of magmatic-hydrothermal ore deposits. Geochim Cosmochim Acta 207:81–101

Zhang K-J, Zhang Y-X, Tang X-C, Xia B (2012) Late Mesozoic tectonic evolution and growth of the Tibetan plateau prior to the Indo-Asian collision. Earth-Sci Rev 114:236–249

Zhang Y-Q, Xie YW (1997) Nd, Sr isotopic characteristics and chronology of Ailaoshan–Jinshajiang alkali-rich intrusions. Sci China (Ser. D) 27:289–293 (in Chinese)

Zheng J-P (1999) Mesozoic-Cenozoic Mantle Replacement and Lithospheric Thinning beneath Eastern China. China University of Geosciences Press, Wuhan, 126 p. (in Chinese with English abstract)

Zhao G-C, Wang Y-J, Huang B-C, Dong Y-P, Li S-Z, Zhang G-W, Yu S (2018) Geological reconstructions of the East Asian blocks: from the breakup of Rodinia to the assembly of Pangea. Earth-Sci Rev 186:262–286

Zhao J-H, Zhou M-F, Yan D-P, Yang Y-H, Sun M (2008) Zircon Lu–Hf isotopic constraints on Neoproterozoic subduction-related crustal growth along the western margin of the Yangtze Block, South China. Precambrian Res 163:189–209

Zhao J-H, Zhou M-F (2013) Neoproterozoic high-Mg basalts formed by melting of ambient mantle in South China. Precambrian Res 233:193–205

Zhao J-H, Asimow PD (2014) Neoproterozoic boninite-series rocks in South China: a depleted mantle source modified by sediment derived melt. Chem Geol 388:98–111

Zhao J-H, Li Q-W, Liu H, Wang W (2018) Neoproterozoic magmatism in the western and northern margins of the Yangtze Block (South China) controlled by slab subduction and subduction-transform-edge-propagator. Earth-Sci Rev 187:1–18

Zhao T, Li J, Liu G, Cawood PA, Zi J-W, Wang K, Feng Q, Hu S, Zeng W, Zhang H (2020) Petrogenesis of Archean TTGs and potassic granites in the southern Yangtze Block: Constraints on the early formation of the Yangtze Block. Precambrian Res 347:105848

Zhong H, Campbell IH, Zhu W-G, Allen CM, Hu R-Z, Xie L-W, He D-F (2011) Timing and source constraints on the relationship between mafic and felsic intrusions in the Emeishan large igneous province. Geochim Cosmochim Acta 75:1374–1395

Zhou H-Y, Sun X-M, Cook NJ, Lin H, Fu Y, Zhong R-C, Brugger J (2017) Nano- to micron-scale particulate gold hosted by magnetite: a product of gold scavenging by bismuth metls. Econ Geol 112:993–1010

Zhou M-F, Yan D-P, Kennedy AK, Li Y-Q, Ding J (2002) SHRIMP U-Pb zircon geochronological and geochemical evidence for Neoproterozoic arc-magmatism along the western margin of the Yangtze Block, South China. Earth Planet Sci Lett 196:51–67

Zhou Y, Hou Z-Q, Zheng Y-C, Xu B, Wang R (2017) Granulite xenoliths in Liuhe area: evidence for composition and genetic mechanism of the lower crust from the Neoproterozoic to Cenozoic. Acta Petrol Sin 33:2143–2160

Zhou Y (2018) Metal fertilization (Cu, Au) of Juvenile Lower–crust and petrogenesis of adakite–like rock in Beiya–Liuhe area. Ph.D. thesis, China University of Geosciences, Beijing (in Chinese with English abstract)

Zhou Y, Xu B, Hou Z-Q, Wang R, Zheng Y-C, He W-Y (2019) Petrogenesis of Cenozoic high–Sr/Y shoshonites and associated mafic microgranular enclaves in an intracontinental setting: Implications for porphyry Cu-Au mineralization in western Yunnan, China. Lithos 324–325:39–54

Zhu D-C, Zhao Z-D, Niu Y, Mo X-X, Chung S-L, Hou Z-Q, Wang L-Q, Wu F-Y (2011) The Lhasa Terrane: record of a microcontinent and its histories of drift and growth. Earth Planet Sci Lett 301:241–255

Zhu D-C, Zhao Z-D, Niu Y, Dilek Y, Hou Z-Q, Mo X-X (2013) The origin and pre-Cenozoic evolution of the Tibetan Plateau. Gondwana Res 23:1429–1454

Zhu D-C, Wang Q, Zhao Z-D, Chung S-L, Cawood PA, Niu Y, Liu S-A, Wu F-Y, Mo X-X (2015) Magmatic record of India-Asia collision. Sci Reports 5:14289

Zhu D-C, Wang Q, Cawood A, Zhao Z-D, Mo X-X (2017) Raising the Gangdese Mountains in southern Tibet. J Geophys Res-Solid Earth 122:214–223

Zhu J-J, Hu R-Z, Richards JP, Bi X-W, Zhong H (2015) Genesis and magmatic-hydrothermal evolution of the Yangla Skarn Cu deposit, Southwest China. Econ Geol 110:631–652

Zhu J-J, Richards JP, Rees C, Creaser R, DuFrane SA, Locock A, Petrus JA, Lang J (2018) Elevated magmatic sulfur and chlorine contents in ore-forming magmas at the red chris porphyry Cu-Au deposit, Northern British Columbia, Canada. Econ Geol 113:1047–1075

Zhu J-J, Hu R, Bi X-W, Hollings P, Zhong H, Gao J-F, Pan L-C, Huang M-L, Wang D-Z (2022) Porphyry Cu fertility of eastern Paleo-Tethyan arc magmas: evidence from zircon and apatite compositions. Lithos 424–425:106775

Zhu X-P, Mo X-X, White NC, Zhang B, Sun M-X, Wang S-X, Zhao S-L, Yang Y (2013) Petrogenesis and metallogenic setting of the Habo porphyry Cu-(Mo-Au) deposit, Yunnan, China. J Asian Earth Sci 66:188–203

Zi J-W, Cawood A, Fan W-M, Wang Y-J, Tohver E (2012) Contrasting rift and subduction-related plagiogranites in the Jinshajiang ophiolitic melange, southwest China, and implications for the Paleo-Tethys. Tectonics 31. https://doi.org/10.1029/2011TC002937

Zou X-Y, Qin K-Z, Han X-L, Li G-M, Evans NJ, Li Z-Z, Yang W (2019) Insight into zircon REE oxy-barometers: a lattice strain model perspective. Earth Planet Sci Lett 506:87–96